designed. Whenever the Power MOS is switched-on by a driver, the current to be detected flows through the power trace on the PCB. When the setup aims to test a resistive current sensing under the effect of EMI, the Hall sensor output is floating and the voltage across the sense resistor R_{sense} in series with the Power MOS is properly amplified and processed by a detection block (as sketched in Figure 1a). On the contrary, to evaluate the EMI robustness of the Hall sensor, the resistor R_{sense} is shorted and the output voltage of the Hall sensor is elaborated by a properly-modified detection block (as sketched in Figure 1b).

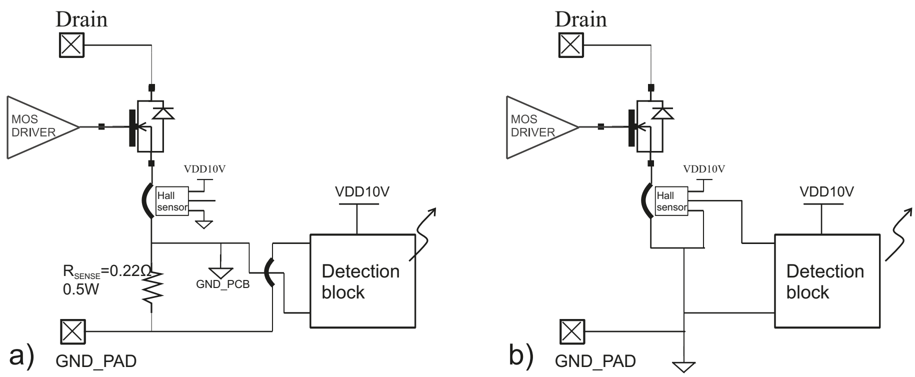

Figure 1. Schematic view of the current sensing setup for: (**a**) resistive approach; and (**b**) the Hall sensor.

A schematic layout representation of the the test PCB that can address both the current sensing methods is reported in Figure 2. A power MOS transistor, which is remotely driven by an optical fiber link, is employed to switch on and off the power circuit. The power supplies to the MOS and to the analog front-end are obtained from a line of the wiring harness and reach the PCB trough an automotive connector.

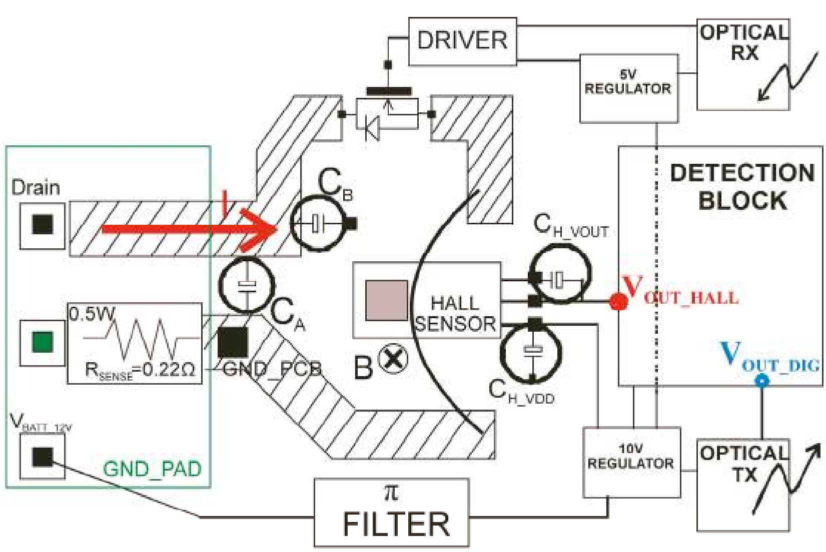

Figure 2. Layout representation of the testing board.

The power supply voltage for the signal acquisition front-end is filtered by a π-type LC and further processed by a 10 V regulator. To reject conducted disturbance in the range of the DPI tests (1–400 MHz), the π filter is composed of a 3 µH inductor and two 100 nF capacitors at its terminals. The regulator provides the power supply to the Hall sensor, to the optical transmitter and to the detection block. A further voltage regulator provides a 5 V supply to the optical receiver and power driver.

The bottom side of the PCB is a ground reference plane named GND_PCB. In Figure 2, the rectangular box on the left indicates a track on the bottom side of the PCB that separates two different ground plane references: GND_PAD and GND_PCB (respectively, inside and outside the rectangular box). This two reference areas are electrically connected by the resistance R_{sense} during resistive current sensing, while, for the Hall-effect based current sensing, the two areas are shorted. Electromagnetic simulations by means of ANSYS Maxwell [14] were performed on the PCB cross section to ensure that the Hall-effect device did not suffer from the magnetic field due to the current in the bottom ground plate. Thus, only the wire placed on the Hall sensor (as in Figure 2) generated the magnetic field due to the current flowing in itself and to be detected by the sensor.

Hall-Effect versus Resistive Setup

Depending on which of the two considered current sensing is investigated (Hall-effect based or resistive one), proper paths are enabled and the respective components are mounted on the PCB to define the signal processing chain. Thus, the Hall sensor output voltage or the voltage drop across R_{sense}, respectively, is properly processed by a detection block, as represented in Figure 2, which contains a non-inverting gain stage and a hysteresis threshold comparator, as reported in Figure 3. Such a hysteresis comparator provides a digital output voltage related to its threshold input voltages (output voltage of the amplifier), respectively, equal to V_{TL} and V_{TH}. Such a comparator drives an optical transmitter so that the comparator output can be remotely monitored.

For resistive current sensing, these hysteresis thresholds correspond to a sensed current, respectively, equal to $I_{\min} = 0.85$ A and $I_{\max} = 0.65$ A, as reported in Figure 4a.

For Hall-effect current sensing, depending on the magnitude of the current flowing through the power circuit, a magnetic induction field is generated. The Hall-effect sensor is sensitive to this magnetic induction field and generates a proportional output voltage showing. The sensitivity is $1\,\frac{\mathrm{mV}}{\mathrm{mT}}$, which roughly corresponds to an output voltage of 10 mV for a current of 1 A flowing in the PCB power circuit. On this basis, the two voltage levels V_{TL} and V_{TH} are due to two correspondent current values equal, respectively, to $I_{\min}$ = 0.9 A and $I_{\max}$ = 2.7 A, as reported in Figure 4b. Notice that these two current values vary depending on the distance between the Hall magnetic sensitive plate and the wire in which flows the current that generates the sensed magnetic field.

The hysteresis windows in Figure 4a,b are defined to find a failure event in the current sensing induced by the EMI-presence. Such event corresponds to the High-to-Low transition of the hysteresis comparator that, in turn, produces a light signal generated by the optical RX that can be remotely acquired.

Despite of the fact that the hysteresis window amplitude for resistive current sensing is 10× narrower than the one employed with the Hall sensor (as can be highlighted comparing Figure 4a,b), the resistive current method shows a strong robustness to EMI. No failure in its current detection were experienced during any of the EMI tests discussed in this paper. Thus, for the sake of simplicity, the robustness of the resistive current method is not mentioned again so that only the investigations referring to the Hall-effect current sensor are discussed in the following.

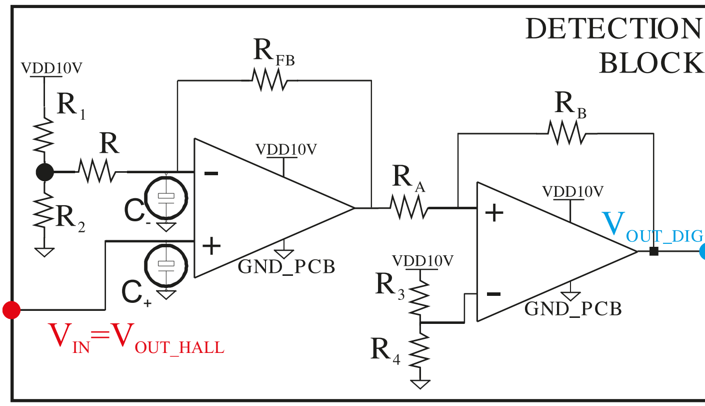

Figure 3. Processing chain of the Hall sensor output voltage.

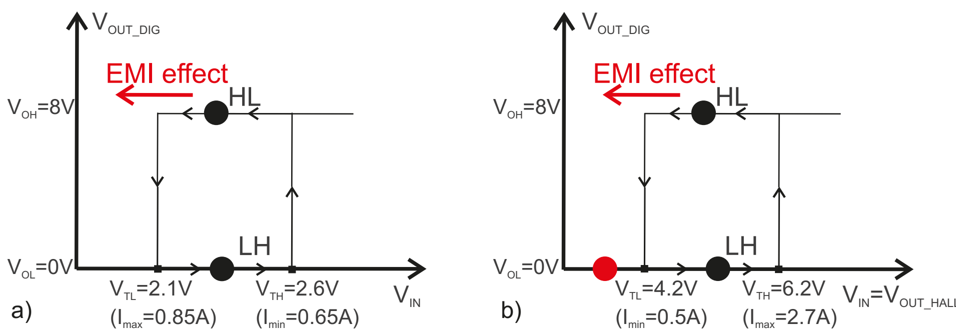

Figure 4. Hysteresis window of the output comparator for: (**a**) resistive current sensing; and (**b**) the Hall-effect sensor.

3. Bulk Current Injection (BCI) Test

To assess the susceptibility of the testing board introduced in Section 2, BCI tests were performed on the overall current detection system in Figure 5 by the setup in Figure 6 [11].

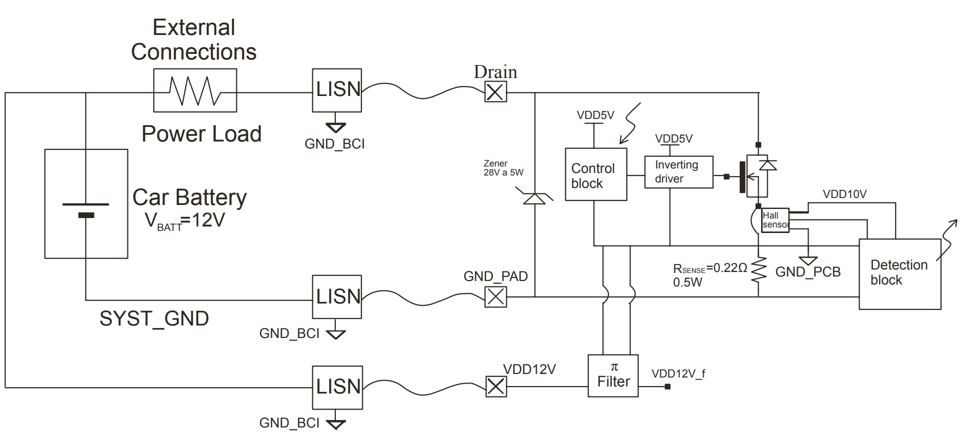

Figure 5. Overall schematic view of the current detection setup.

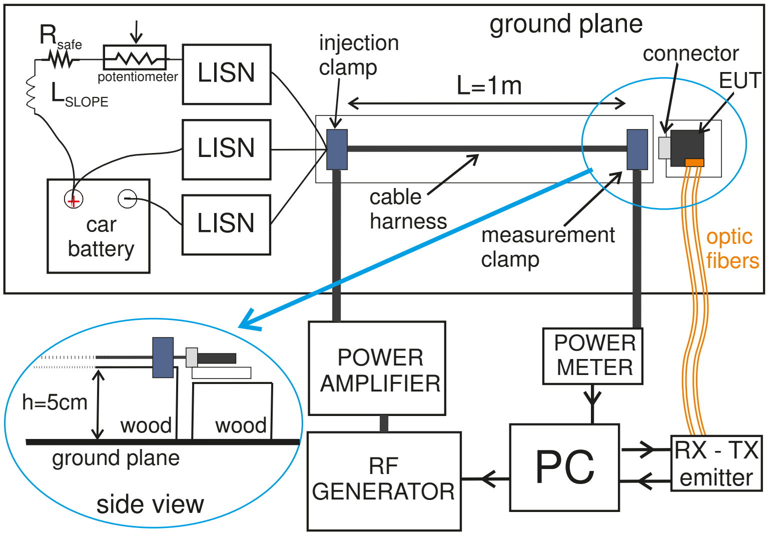

Figure 6. Pictorial representation of BCI test setup [11].

In such a setup, the equipment under test (EUT) is connected to the a variable resistive power load (potentiometer in the figure), to a car battery and to a remote ground reference through a 1 m-long three-wire harness running 5 cm above the system ground plane on a wooden structure (inset in Figure 6). The three wires of the harness are connected to the loads and to the battery through three Line Impedance Stabilization Networks (LISNs in Figures 5 and 6), which provide a 50 Ω RF termination to each line. Every LISN is designed to show an impedance equal to 50 Ω at its RF terminals independently of the load connected at its low-frequency input terminals in the test bandwidth (0–400 MHz).

During the tests, an injection clamp (F-130A-1 [15]) and a measurement clamp (F-51 [16]) by Fischer Custom Communication (FCC) are located along the harness, as shown in Figure 6, to perform BCI tests in compliance with [11]. The distance between the injection and measurement clamps is 75 cm, while the distance between the measurement clamp and the EUT is 4.5 cm. The injection clamp is connected to the output of an 10 W RF power amplifier, whose input terminal is connected to a CW RF signal source, while the measurement clamp is connected to an RF power meter to measure the bulk current injected into the EUT. The power amplifier, the RF source, the RF power meter and the control unit are located out of the test area. The EUT is connected to a two-way optical fiber link in order to drive the power transistor in the EUT and to monitor the current sensor output without perturbing the surrounding electromagnetic environment. A potential malfunction of the current detecting of the EUT during BCI tests is due to common-mode RF current (bulk current) injected into the EUT through its wiring harness.

3.1. BCI Susceptibility Tests

BCI measurements in the bandwidth (10–400 MHz) were performed by a PC-based acquisition system, as represented in Figure 6. For each test frequency, the RFI amplitude is increased until a failure in the DUT operation is experienced or the maximum incident RF power deliverable by the amplifier is reached. In the first case, the failure injected bulk current obtained from the power meter measurement is acquired. Otherwise, no failure value is reported (missing points and respective connecting lines in Figures 7–10).

Referring to the above-mentioned EUT, the commutation of the hysteresis comparator voltage has been considered as a failure criterion and the potentiometer has been configured so that a DC current $I = \frac{I_{\text{min}}+I_{\text{max}}}{2}$ flows in the power circuit. More precisely, at each failure event, the EUT has been configured so that the hysteresis comparator operates at the point HL in Figure 4 with no EMI excitation.

To highlight the susceptibility of the Hall-effect sensors, BCI immunity tests were performed the on different configurations of the EUT introduced in Section 2.

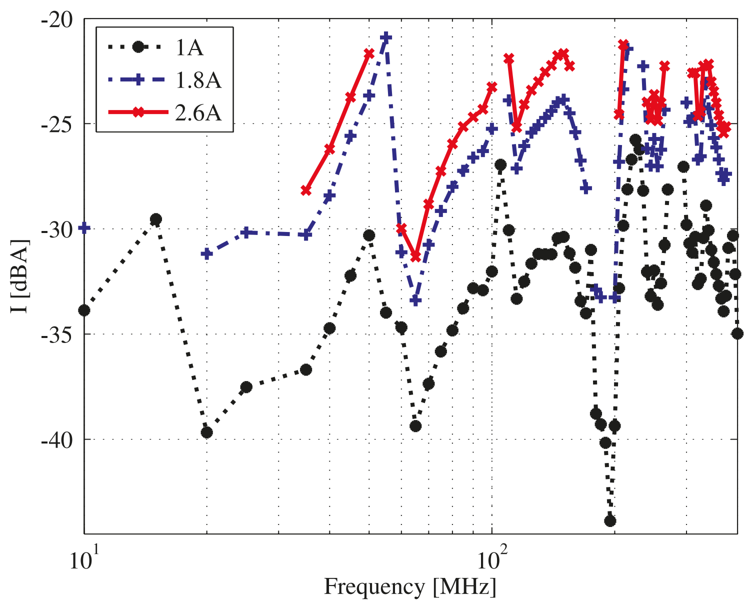

Figure 7. BCI immunity measurement for different current values.

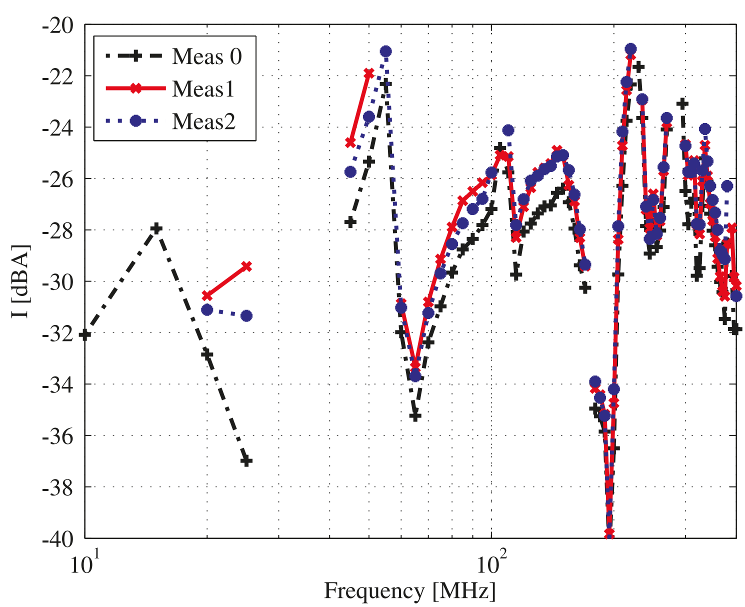

Figure 8. BCI immunity measurement for different caps presence in layout in Figure 2: Meas0 = no caps; Meas1 = C_+, C_-; and Meas2 = C_+, C_-, C_{H_VOUT}, C_{H_VDD}.

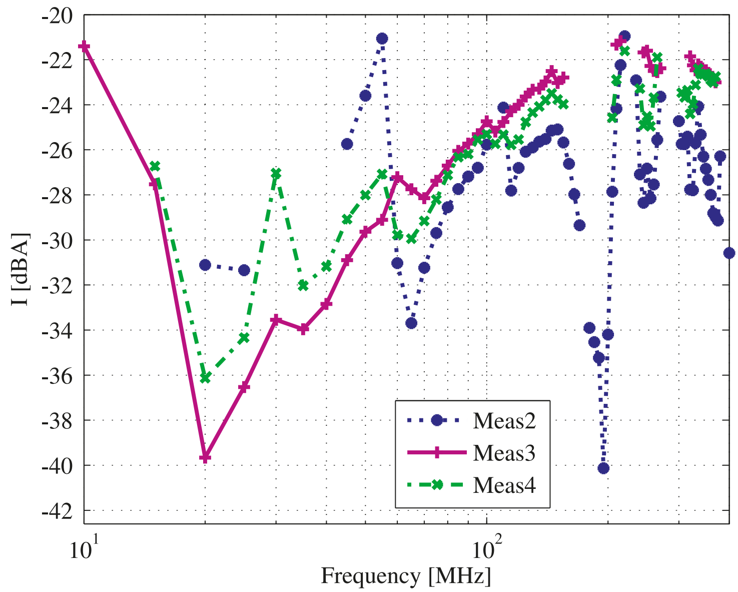

Figure 9. BCI immunity measurement for different caps presence in layout in Figure 2: Meas2 = C_+, C_-, C_{H_VOUT}, C_{H_VDD}; Meas3 = C_+, C_-, C_{H_VOUT}, C_{H_VDD}, C_A; and Meas4 = C_+, C_-, C_{H_VOUT}, C_{H_VDD}, C_B

3.2. BCI Test Results

The susceptibility to EMI of the EUT in Figure 6 was first tested for different values of the DC current flowing through the power line. The results of such tests are reported in Figure 7. It can be observed that the susceptibility level of the EUT scales with the DC current level, depending on the proximity of the threshold value.

Moreover, several BCI measurements were performed adding 100 nF filter capacitors in order to reject the conducted disturbances. They were placed at the terminals of the main blocks (i.e., inputs of the detection block or Hall sensor leads) and to define the influence of the parasitic of the long trace on the PCB.

The encircle capacitances in Figures 2 and 3 point out the most significant filter capacitances added on the PCB in the successive tests described in this section. The susceptibility of the EUT with no filter capacitors on the Hall sensor acquisition front-end is firstly considered and named Meas0 in Figure 8. Then, two capacitors C_+ and C_- were placed at the inputs of the operational amplifier of the detection block, as in Figure 3. The susceptibility tests were repeated and data collected as Meas1 in Figure 8. Another configuration, listed as Meas2 in Figure 8, includes the capacitors C_+ and C_- as in Meas1 but two further capacitors C_{H_VOUT}, C_{H_VDD} at Hall sensor leads, as represented in Figure 2. Comparing the above-mentioned three configurations, the capacitors do not strongly affect the immunity level of the EUT.

Other measurements were performed including other capacitors. The immunity level of the EUT was explored with a capacitor C_A between the drain and source of the power transistor, as reported in Figure 2. At the capacitors already placed in Meas2, such capacitor C_A was added and the respective measurements are named as Meas3 in Figure 9. Then, instead of the capacitor C_A, a capacitor C_B between the drain and the ground plane on the bottom side of the DUT was placed. The respective measurements are reported as Meas4 in Figure 9. Comparing Meas2, Meas3 and Means4 shows that the respective additional capacitors result in a slightly higher immunity for frequencies higher than 600 MHz. Thus, no significant immunity improvement is experienced in any of the above-mentioned configurations.

Other EMI investigations were performed for different Hall sensor inclination with respect to the PCB surface, as represented in Figure 10a. In all cases, the distance beetween the wire and the Hall sensor has not been changed. The experimental results obtained with such configurations are reported in Figure 10b and show a significant dependence of the susceptibility level on the inclination of the sensor.

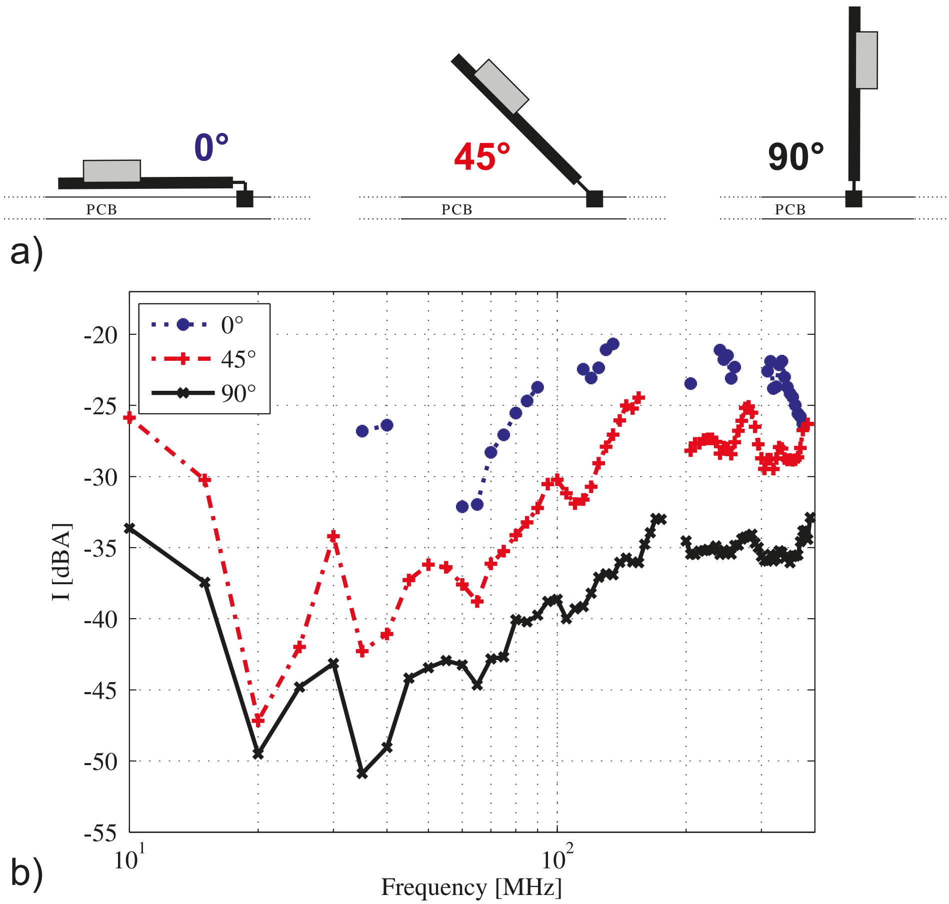

Figure 10. (**a**) Hall sensor inclination considered in BCI tests; and (**b**) respective BCI immunity measurements.

3.3. Discussion

Figure 7 shows how the failure level of the EUT scales with the current to be measured. As a consequence, EMI-induced failures seems to be related to an EMI-induced upset in the Hall-effect sensor output signal path. On the other hand, Figures 8 and 9 show that the susceptibility level of the EUT is scarcely affected by the introduction of filter capacitors at the conditioning amplifier inputs and at the terminals of the Hall-effect current sensors. Therefore, the EUT susceptibility is not related to the detection block or the trace parasitics. On the contrary, the measurements performed for different Hall sensor inclinations (Figure 10b) show that the immunity level is strongly affected by the inclination of the sensor. On this basis, the susceptibility to EMI of the EUT seems to be related to direct electromagnetic field coupling in the Hall-effect sensor body. For this reason, further TEM cell immunity tests were performed.

4. Transverse-Electromagnetic (TEM) Cell Tests

To investigate in further detail the EMI-induced failures in the Hall sensor highlighted by BCI measurements, the susceptibility to radiated EMI of such a sensor was tested in a TEM cell, by placing the sensor in the cell, as sketched in Figure 11. The Hall sensor ground lead was shorted to the TEM cell internal side while the supply voltage (VDD) and the output (V_{OUT}) terminals were AC-shorted to the internal side of the TEM cell. VDD and V_{OUT} leads come out from the TEM cell upper side. Through these terminals, the DC power supply of the sensor was provided and its DC output voltage was measured. To verify the device susceptibility to electric and magnetic fields, the Hall sensor was placed inside the cell TEM in different orientations (A–D in Figure 11).

Figure 12 points out the magnetic and electric field directions in the different setup considered in the following. In Setups A and B, the RF electric field E_x (along x-axis) is parallel to the device orientation. Instead, Setups A and B differ to the device orientation with respect to the RF magnetic field H_y (along y-axis). In Setup A, H_y is parallel to the Hall sensor surface, while, in Setup B, H_y is orthogonal to the device. Similarly, in Setups C and D, the RF electric field E_x is orthogonal while these two setup differ to the RF magnetic field orientation with respect to Hall sensor surface.

4.1. (TEM) Cell Measurement Result

The radiated EMI susceptibility tests highlight that electromagnetic field distribution inside the TEM cell induces a negative offset in the Hall sensor output voltage. In Figure 13, the magnitude of the induced offset voltage in the range from 500 kHz to 1 GHz for an RF incident power applied to the TEM cell equal to 34 dBm. This implies a vertical electric field magnitude of 250 V/m and a transversal magnetic field magnitude of 0.66 A/m where the Hall sensor under test is placed [17–19].

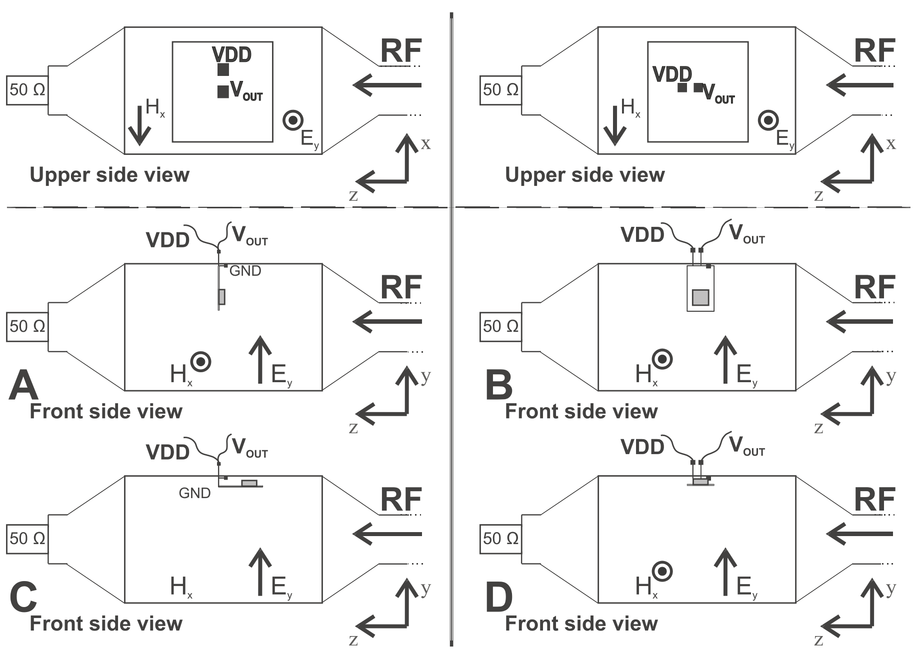

Figure 11. TEM cell testing setup.

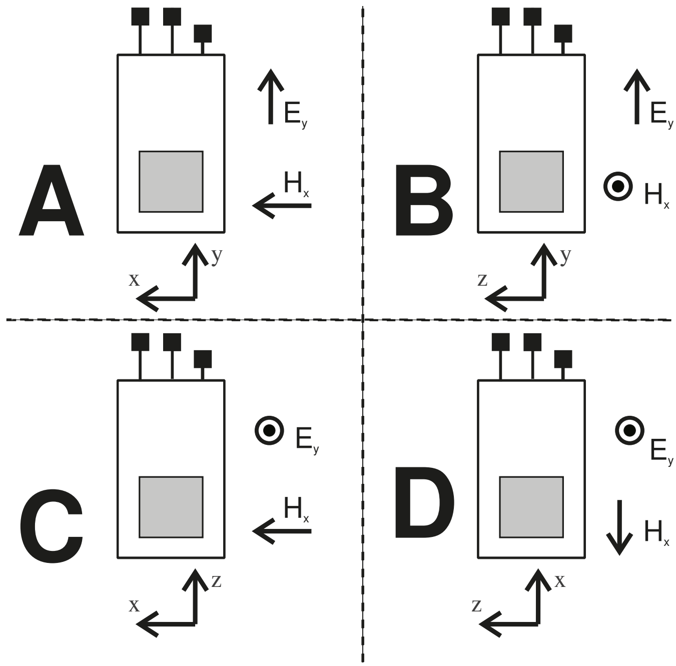

Figure 12. Magnetic and electric field orientation for different Hall sensor setup.

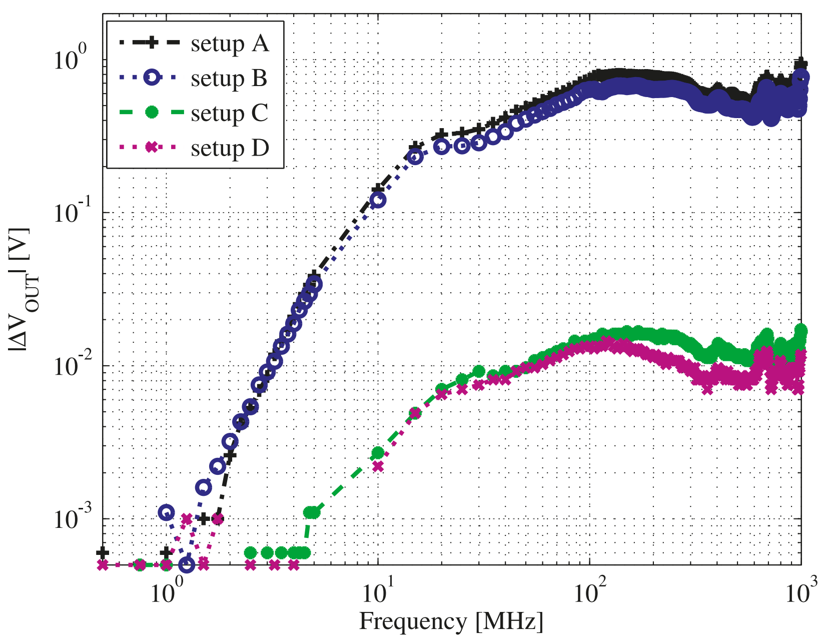

Figure 13. TEM cell immunity measurements at 34 dBm RF power amplitude for different setup.

4.2. Discussion

Figure 13 highlights the similarity between the EMI induced offset voltage measured in Setups A and B. In addition, Setups C and D show similarity in terms of EMI-induced offset. Moreover, Setups A and B are differently coupled to the TEM cell magnetic field and similarly coupled to the electric field, whereas Setups A and C (Setups B and D) are differently coupled in terms of electric field. On this basis, the susceptibility to EMI of the Hall-effect sensor can be related to the electric field parallel to the Hall sensor plate. This could be due to the susceptibility of the sensor either to the electric field directly coupled to the sensing element or to the disturbances connected by leads and metal interconnections on the sensor body.

5. Direct Power Injection (DPI)

As a further EMI investigation, direct power injection tests [13] on the employed Hall sensor were performed. RF power was injected on the supply voltage of the Hall sensor by means of an RF generator, an RF amplifier and a bias tee, as represented in Figure 14. The employed bias tee has a lower bandwidth limit equal to 30 MHz. Therefore, in the following figure, the measurement results are not reliable for a frequency lower that 30 MHz. At the end of the power amplifier a −3 dB attenuator was placed for the safety of the RF amplifier. In fact, if the RF amplifier were accidentally not totally connected (open circuit condition) during the measurement operation, a reflection coefficient $|\Gamma| = 1$ could damage the RF amplifier.

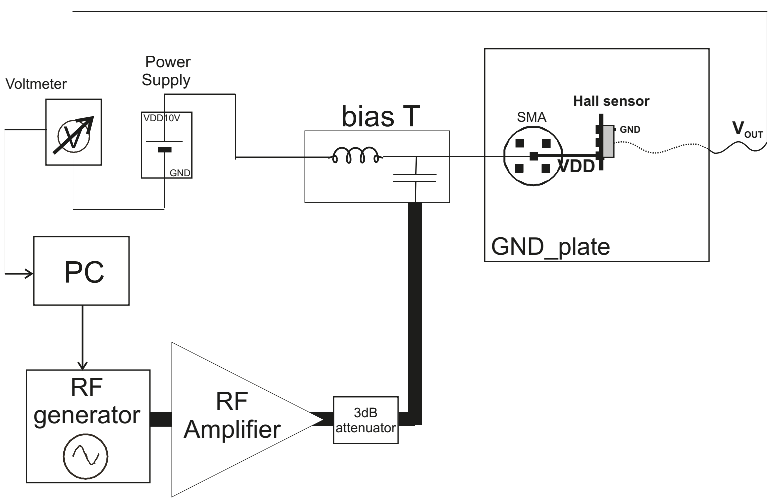

Figure 14. DPI on Hall sensor VDD Test setup [13].

The incident powers provided are given as results of the sum of the incident power of the RF generator (respectively, −50, −40, −30, −20, and −10 dBm), 34 dBm of the RF amplifier and the attenuation due to a −3 dB attenuator. On this basis, the induced offset voltages ΔV_{OUT} due to RF power amplitudes equal −19, −9, 1, 11, and 21 dBm injected on VDD in the range 500 kHz–1 GHz are reported in Figure 15. Similarly, the induced offset voltages ΔV_{OUT} due to frequencies of 100 MHz, 500 MHz and 1 GHz for amplitude in the range −19 dBm to +21 dBm are reported in Figure 16. An upper limit to provided RF power amplitude equal to 21 dBm was chosen to avoid Hall sensor destruction due an excessive power at its terminals. Such an amplitude corresponds to a theoretical maximum voltage on supply voltage VDD lead equal to 17 V.

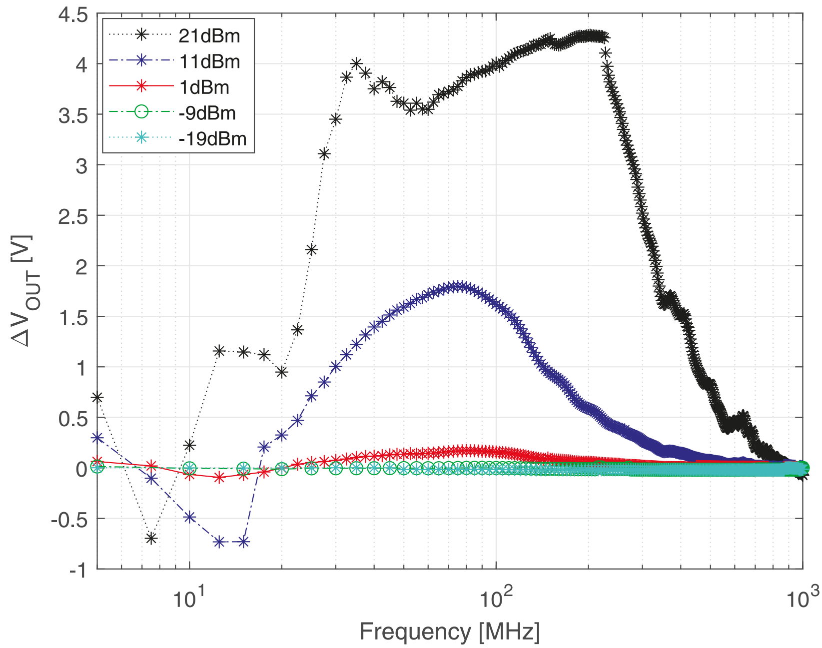

Figure 15. DPI on VDD immunity measurements ($|\Delta V_{OUT}|$ vs. frequency) for different RF power amplitudes.

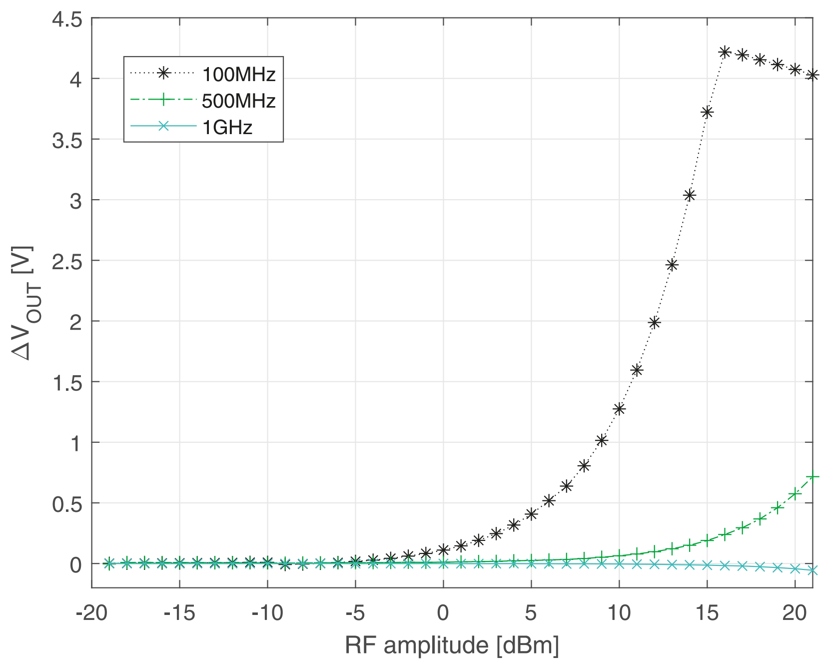

Figure 16. DPI on VDD immunity measurements ($|\Delta V_{OUT}|$ vs. RF power amplitude) for different frequencies.

Different signs of the induced offset are highlighted in Figures 15 and 16. These phenomena seem to be due to different nonlinear mechanisms of active elements in the device. Similar measurement results are shown even in the EMI superimposed on the output terminal of the Hall sensor. Although even the DPI tests show the susceptibility to EMI of the investigated Hall sensor, no precise reasons for such failure can be inferred.

6. Conclusions

The susceptibility to EMI of a Hall-effect sensor employed in current monitoring was investigated firstly referring to BCI test. Hall-effect current sensors (contactless) are dramatically affected by the EMI presence, contrary to the resistive (wired) current sensing method. BCI tests were performed in difference configurations, in addition to TEM cell and DPI tests. The measurements results show that a Hall-effect sensor can be strongly affected by the presence of EMI. In particular, the TEM cell tests highlighted how the operations of the specific Hall-effect sensor considered in this study are affected by an RF electric field excitation parallel to the surface of the sensing element. As the physical mechanism of the Hall-effect is not affected by a CW RFI [7], the failures of the Hall sensor are likely related to the ICs that interface the Hall sensor and process its signal. Although many investigations are present in the literature regarding amplifier and monitoring ICs [20–22], a precise understanding of the Hall sensor failure causes always relies on a complete knowledge of the ICs that interface with the Hall plates. This implies that the EMI-induced effects have to be taken into account from the first phases of the Hall-effect sensor design.

Funding: This research received no external funding.

Conflicts of Interest: The author declares no conflict of interest.

References

1. Tong, Q.; Chen, C.; Zhang, Q.; Zou, X. A Sensorless Predictive Current Controlled Boost Converter by Using an EKF with Load Variation Effect Elimination Function. *Sensors* **2015**, *15*, 9986–10003. [CrossRef] [PubMed]
2. Min, R.; Chen, C.; Zhang, X.; Zou, X.; Tong, Q.; Zhang, Q. An Optimal Current Observer for Predictive Current Controlled Buck DC-DC Converters. *Sensors* **2014**, *14*, 8851–8868. [CrossRef] [PubMed]
3. Aiello, O.; Fiori, F. A new mirroring circuit for power MOS current sensing highly immune to EMI. *Sensor* **2013**, *13*, 1856–1871. [CrossRef] [PubMed]
4. Aiello, O.; Fiori, F. Current sensing circuit for DC-DC converters based on the miller effect. In Proceedings of the 2013 International Conference on Applied Electronics (AE), Pilsen, Czech Republic, 10–11 September 2013; pp. 1–4.
5. Huang, K.; Liu, Z.; Zhu, F.; Zheng, Z.; Cheng, Y. Evaluation Scheme for EMI of Train Body Voltage Fluctuation on the BCU Speed Sensor Measurement. *IEEE Trans. Instrum. Meas.* **2017**, *66*, 1046–1057. [CrossRef]
6. Popovic, R.S. *Hall Effect Devices*, 2nd ed.; Institute of Physics Publishing: Bristol, UK; Philadelphia, PA, USA, 2004.
7. Aiello, O.; Fiori, F. A New MagFET-Based Integrated Current Sensor Highly Immune to EMI. *Elsevier Microelectron. Reliab.* **2013**, *53*, 573–581 . [CrossRef]
8. Aiello, O.; Crovetti, P.; Fiori, F. Investigation on the susceptibility of hall-effect current sensors to EMI. In Proceedings of the 10th International Symposium on Electromagnetic Compatibility, York, UK, 26–30 September 2011; pp. 1–4.
9. Satav, S.M.; Agarwal, V. Design and Development of a Low-Cost Digital Magnetic Field Meter With Wide Dynamic Range for EMC Precompliance Measurements and Other Applications. *IEEE Trans. Instrum. Meas.* **2009**, *58*, 2837–2846. [CrossRef]
10. Dalessandro, L.; Karrer, N.; Kolar, J.W. High-Performance Planar Isolated Current Sensor for Power Electronics Applications. *IEEE Trans. Power Electron.* **2007**, *22*, 1682–1692. [CrossRef]
11. International Standard ISO 11452-4:2005. Road Vehicles–Component Test Method for Electrical Disturbances from Narrowband Radiated Electromagnetic Energy—Part 4: Bulk Current Injection (BCI). Available online: https://www.iso.org/standard/37414.html (accessed on 6 November 2019).

12. International Standard IS0 11452-3:2016. Road Vehicles—Electrical Disturbances by Narrowband Radiated Electromagnetic Energy, Component Test Method Part 3: Transverse Electromagnetic Mode (TEM) Cell. Available online: https://www.iso.org/standard/66829.html (accessed on 6 November 2019).
13. IEC 623132-4:2006. Integrated Circuits, Measurement of Electromagnetic Immunity—Part 4: Direct RF Power Injection Method. Available online: https://webstore.iec.ch/publication/6510 (accessed on 6 November 2019).
14. Available online: https://www.ansys.com/products/electronics/ansys-maxwell (accessed on 6 November 2019).
15. Fischer Custom Communication (FCC). *F-130A-1 Injection Current Probe Characterization: Fischer Custom Communication (FCC)*; FCC: Torrance, CA, USA, 2004.
16. Fischer Custom Communication (FCC). *F-51 Monitor Current Probe Characterization: Fischer Custom Communication (FCC)*; FCC: Torrance, CA, USA, 2004.
17. Fiori, F.; Musolino, F. Investigation on the effectiveness of the IC susceptibility TEM cell method. *IEEE Trans. EMC* **2004**, *46*, 110–114. [CrossRef]
18. Fiori, F.; Musolino, F. Measurement of integrated circuit conducted emissions by using a transverse electromagnetic mode (TEM) cell. *IEEE Trans. EMC* **2001**, *43*, 622–628. [CrossRef]
19. Spiegel, R.J.; Joines, W.T.; Blackman, C.F.; Wood, A.W. A method for calculating electric and magnetic fields in TEM cell at ELF. *IEEE Trans. Electromagn. Compat.* **1987**, *EMC-29*, 265–272. [CrossRef]
20. Redoute, J.M.; Steyaert, M. *EMC of Analog ICS*; Springer: Berlin, Germany, 2010.
21. Richelli, A.; Matiga, G.; Redoute, J.M. Design of a Folded Cascode Opamp with Increased Immunity to Conducted Electromagnetic Interference in 0.18 um. *Elsevier Microelectron. Reliab.* **2015**, *55*, 654–661. [CrossRef]
22. Aiello, O.; Fiori, F. On the Susceptibility of Embedded Thermal Shutdown Circuit to Radio Frequency Interference. *IEEE Trans. EMC* **2012**, *54*, 405–412. [CrossRef]

electronics

Article

A Novel Meander Split Power/Ground Plane Reducing Crosstalk of Traces Crossing Over

Jung-Han Lee [1,2]

[1] Department of Electronic Engineering, Sogang University, Seoul 04107, Korea; leejunghan@kiost.ac.kr
[2] Marine Security and Safety Research Center, Korea Institute of Ocean Science & Technology, Busan 49111, Korea

Received: 29 August 2019; Accepted: 16 September 2019; Published: 17 September 2019

Abstract: In this paper, a novel meander split power/ground plane is proposed for reducing crosstalk between parallel lines crossing over it. The working mechanism of the meander split scheme is investigated by simulations and measurements. The LC equivalent circuit and transmission line model are developed for modeling interactions between the meander split and the signal lines. The proposed meander structure enhances electromagnetic coupling between split planes. The capacitive coupling across the split ensures signal integrity and magnetic coupling between adjacent finger shaped structures suppresses lateral wave propagation along the split gap, which in turn helps suppress the crosstalk. The effectiveness of the meander split remains valid over very wide frequency ranges (up to 9 GHz). Experimental results show that the proposed structure improves the signal quality and reduces the near/far end crosstalk over 30 dB and 50% in the frequency domain and time domain, respectively.

Keywords: meander split; power/ground plane; crosstalk; signal integrity; equivalent circuit; capacitive and magnetic coupling

1. Introduction

In high-speed electronic systems, the power and ground planes play important roles as a reservoir in supplying power to components and as a voltage reference on printed circuit boards. To accommodate the rapidly switching components and their demand for current, an ideal power supply should have very low impedances, which necessitates the use of power and ground planes. However, the plane pair effectively forms a parallel plate waveguide, which can hold persistent ringing noises generated by routed traces and vias to and from components on the circuit board. To reduce the noise coupling due to power planes and provide different power supply voltages, slotted or split plane types are frequently used for the integrated circuits or modules [1–3] occupying the same printed circuit boards (PCBs) [4,5]. However, power/ground partitioning generates undesired electromagnetic effects such as signal integrity degradation, electromagnetic interference (EMI) and crosstalk when signal lines cross over the split gaps [6–10]. When two parallel line traces cross over slots or splits in the planes, the crosstalk level between the traces becomes high even for large clearances [11].

Commonly used methods to reduce crosstalk are placing via fences [12], guard traces [13], serpentine guard traces [14], stubs [15], or resonators [16] between the two signal lines. Recently, a method of coating signal lines with graphene-paraffin has also been studied [17]. In most of the approaches, efforts are made to decrease the crosstalk levels by inserting additional structures between the conventional transmission lines. Defective microstrip line structures [18] and stub-alternated microstrip lines [19] have been used for the reduction of crosstalk. With these methods, the complexity of the PCBs is increased due to the additional structures.

Attaching stitching capacitors [11,20] or inter-digital capacitors [21] between the split gap under the signal lines reduces the crosstalk and provides return current paths at high frequency while maintaining distinct dc levels of each region. However, this requires additional processes or costs and sometimes it is hard to make room for the stitching capacitor right below the signal trace. Furthermore, the effectiveness of these approaches is limited in that the equivalent series inductance of the capacitors dominates the impedance of a decoupling capacitor at higher frequencies [22]. Another commonly used approach is the addition a low-Q inductor or a thin inductive trace or stubs [23,24] on split power planes. However, this remedy cannot isolate wideband switching noises generated by each functional block on the same PCB, and cannot accommodate different power supply voltages.

Recently, various shapes of defective ground structures (DGS) such as the "U", "V", "H", rectangular, square, circular, ring and dumbbell shape [25–28] have been investigated to design the wideband filter without adding any complexity to the original structure. Some complex shapes have also been studied, which include meander lines [29]. All of these studies focus on the design of the filter using DGS, and it is necessary to study DGS for their crosstalk reduction effect. Recently, several studies [30,31] have investigated the reduction of crosstalk using rectangular or dumbbell DGS shapes on the ground plane, finding that the reduction effectiveness is 20 dB over a frequency range of 5 GHz.

In this paper, a novel meandered DGS embedded on a split plane is proposed and investigated from the view point of signal transmission and crosstalk reduction. The equivalent circuit model based on slot-coupled cavity equivalent circuit and transmission line theory is presented to describe the behavior of the meandered DGS split gap. The meandered structure enhances capacitive coupling across the split planes, which helps signal transmission of the line traces over a split gap. The structure suppresses lateral wave propagation along the slot-line formed by the split gap by the destructive coupling of the magnetic fields of meandering currents on the adjacent slot line sections. In other words, lateral waves excited along the split gap become evanescent, which helps the return current on the power/ground plane be localized. The crosstalk reduction effectiveness of the split plane with meandered DGS holds 30 dB over a wide frequency range up to 9 GHz, and the crosstalk levels are reduced to over 50% of a simple straight split plane such as a rectangular or dumbbell one [30,31], which is verified by measurements.

2. The Meander DGS on Split Power/Ground Plane

2.1. Advantage and Application of the Meander DGS

In general, the shape, size, and periodicity of the DGS affects the frequency characteristics. A periodic DGS can design well-defined stopbands and passbands and achieve the performance such as high-order filters. DGS can be used in many applications in microwave printed circuits such as filters, amplifiers, oscillators, directional couplers, antennas, and multiplayer stack-up PCBs.

The DGS disturbs the current distribution of the ground plane and changes the characteristics of a transmission line crossing over the DGS [32]. The main disadvantage of the DGS is that they break the return current path and cause spurious radiations in the circuits. The DGS will change the impedance of the ground plane, and lead to spurious radiations. However, our proposed meander DGS has the advantage of providing the return current path by enhancing the coupling between adjacent meander lines. Thus, it can be applied as an excellent method to solve EMI problems such as signal integrity, radiation, and crosstalk.

2.2. Design Methodolgy of the Meander DGS

The meander DGS-like asymmetric inter-digital finger in Figure 1c was used in the split ground plane and optimized for the desired frequency of operation. Due to the structure of the meander split on the ground plane, the vertical length l_{tot} and width w_1, w_2 of the meander split dimension were selected according to the design rule. Within the given criteria ($l_{tot} = 2 \times w_1 + 2 \times l_2 + l_3$), the vertical length l_3 and width w_2 of meander split gap contribute to the mutual inductance and capacitive coupling between the meander gaps, respectively, in Figure 1c. The design parameters related to this electromagnetic coupling are independent of the position of the signal line w_L. That is, the w_L does not necessarily have to be located right above the center of l_1 or w_2.

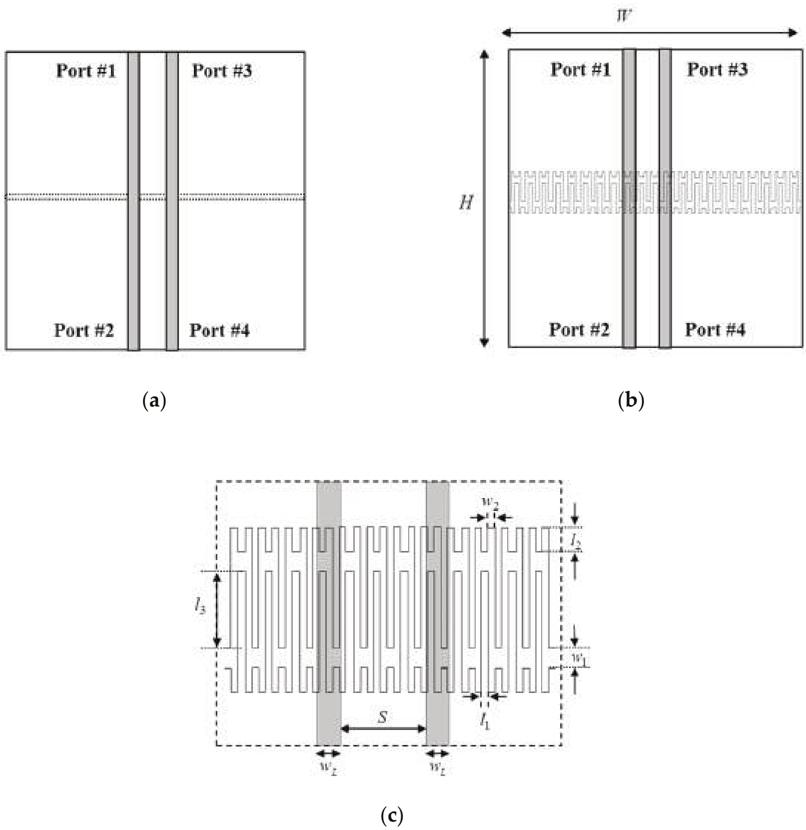

Figure 1. Printed circuit boards with two kinds of split gap adopted. The dotted line is on the bottom side. (**a**) Two signal lines cross over a straight split gap on the ground plane. (**b**) A meander DGS split gap. (**c**) Detailed structure.

The main design method was to select the vertical length l_3 of the meander gap associated with the magnetic coupling and width w_2 of the meander gap associated with the capacitive coupling effect for defining the stopband and passband frequency characteristics. The equivalent circuit of the meander DGS and associated parameters were extracted by the LC equivalent circuit model and transmission line model. The periodic placement (N) of the meander DGS enhances the frequency characteristics of the equivalent circuit and improves the crosstalk reduction effect on broadband frequencies.

Figure 1a,b shows two PCBs containing parallel line traces (W = 100 mm, H = 100 mm, S = 10 mm, w_L = 1.69 mm) on one side. On the bottom sides of the boards, a simple straight split ground plane, like a rectangular DGS [30,31], and a proposed meandered DGS (w_2 = 0.2 mm, l_1 = 0.25 mm, w_1 = 2 mm, l_3 = 20 mm, l_2 = 2 mm) embedded split ground plane are formed, respectively. The dielectric material used for the PCBs is FR4 whose relative permittivity is 4.2, and the thickness of the boards is 1.0 mm. The width of the split gaps of the two boards is 2 mm. There are a total of 110 (N) meandering cells in the split in Figure 1c, which are not drawn to real scale. The characteristic impedances of the signal traces above the solid ground plane are set to be 50 Ω to eliminate reflections from the coaxial cables, which connect the board to a network analyzer.

We measured the scattering parameters of the two samples with a complete homogeneous ground plane in Figure 2. As shown in the figure, the reflections occur due to the split gaps, and the scattering parameters show resonant behavior. Compared with the complete homogeneous ground plane, the two split ground planes degrade the signal integrity and increase crosstalk. However, the meander split improves the signal integrity and decreases 30 dB of crosstalk up to 9 GHz more than the straight split ground plane, like a rectangular DGS [30,31]. This difference comes from the enhanced coupling due to the meander structure on the split plane.

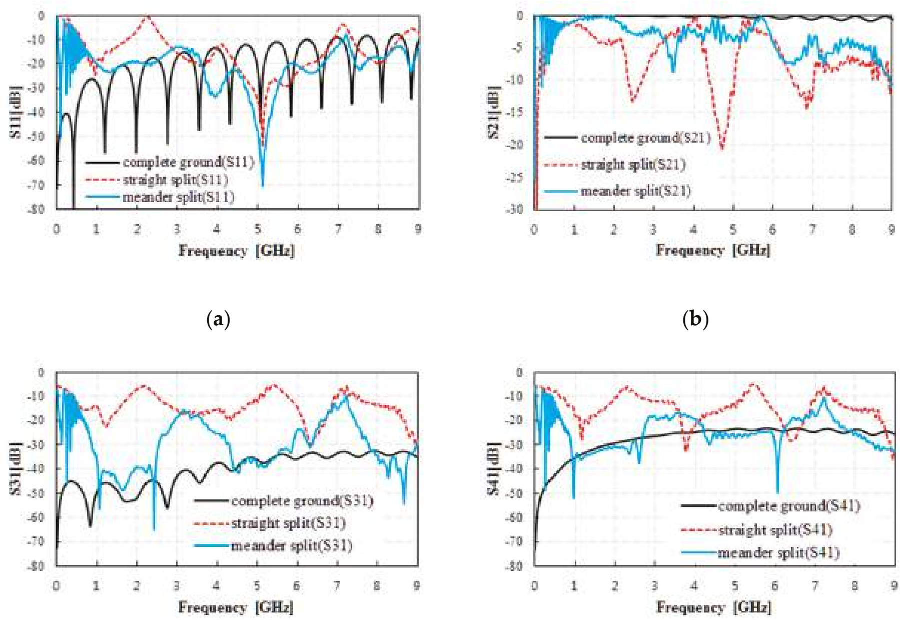

(**a**) (**b**) (**c**) (**d**)

Figure 2. Measured reflection, transmission and crosstalk of the signal line with a complete homogeneous ground, straight and meander split power or ground plane. (**a**) S_{11}. (**b**) S_{21}. (**c**) S_{31} (near-end crosstalk). (**d**) S_{41} (far-end crosstalk).

2.3. Equivalent Circuit of the Meander DGS Split Model

The DGS slot can be modeled in parallel with a capacitor and inductor [32]. Based on the equivalent slot circuit, the LC equivalent circuit of the bottom layer where the ground is a meander gap can be derived in Figure 3. In terms of return current path on the bottom layer, the capacitive and mutual inductance effects exit between the different meanders. The return current paths by the capacitive and mutual inductance effects are represented by the Type 1 (p), Type 2, 3 (m) and Type 4 (n), respectively. The p is the fraction of the return current not involved in the coupling (Type 1), m is the fraction involved in coupling one way only (Type 2 and 3) and n is the fraction involved in coupling one way only (Type 4). The design parameters such as coupling fractions, and the L and C values of the meander structure in Figure 3 were extracted based on the slot-coupled cavity equivalent circuit [33] to define the passband and stopband frequency characteristics.

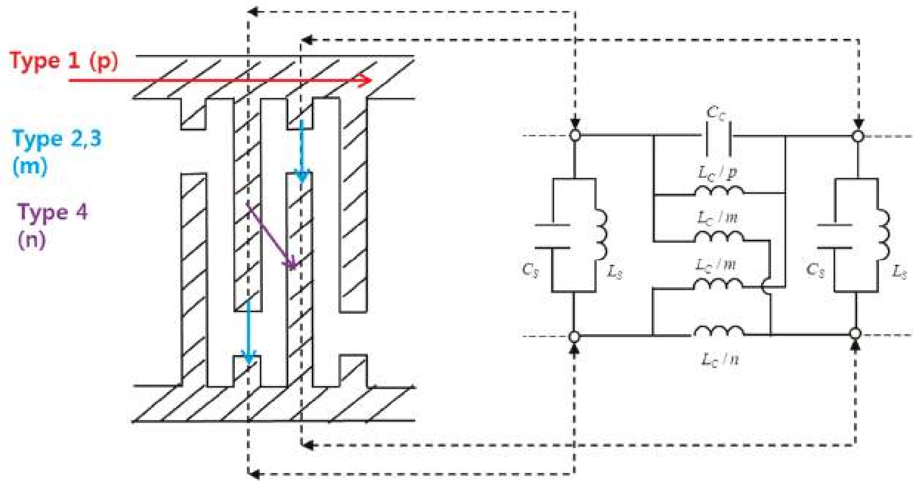

Figure 3. Equivalent circuit of the meander gap.

Alternatively, this enhanced coupling phenomenon can be explained using slot line modes excited in the split. Based on the previous analysis and the scheme of the meander structure, the transmission line equivalent circuit model of the meander split gap can be derived in Figure 4. The meander gap away from the signal line is modeled simply by a series of periodic transmission lines with alternately varying characteristic impedances Z_1, Z_2, Z_3, effective dielectric constants εe_1, εe_2, εe_3 and mutual inductances L_m. To observe the vertical length l_3 and width w_1 of the split gap affecting the crosstalk reduction, we performed a parameter sweep using CST Microwave studio. Due to the structure of the meander split on the ground plane, the vertical length l_{tot} of the meander split cannot be infinitely long. Within the given criteria ($l_{tot} = 2 \times w_1 + 2 \times l_2 + l_3$), the vertical length l_3 of the meander split gap contributes to the mutual inductance. The width w_1 of the meander split gap contributes to the capacitive coupling. We calculated the characteristic impedances and the effective dielectric constants of the slot line as l_3 and w_1 changes (Table 1) by using the conformal mapping technique [34]. By varying the split gap widths (w_1) and length (l_3), the frequency characteristics are designed for passband and stopband of the crosstalk at least (Figure 5).

Table 1. Characteristic impedances and relative dielectric constants of the meander slot line.

l_{tot}(mm)	l_1(mm)	l_2(mm)	l_3(mm)	w_1(mm)	w_2(mm)	w_3(mm)	Z_1(Ω)	Z_2(Ω)	Z_3(Ω)	ε_{e1}	ε_{e2}	ε_{e3}
35	0.25	0.4	5	14.6	0.2	0.2	168	75	75	1.1	1.3	1.3
35	0.25	0.4	15	9.6	0.2	0.2	149	75	75	1.1	1.4	1.4
35	0.25	0.4	30	2.1	0.2	0.2	106	75	75	1.1	1.4	1.4

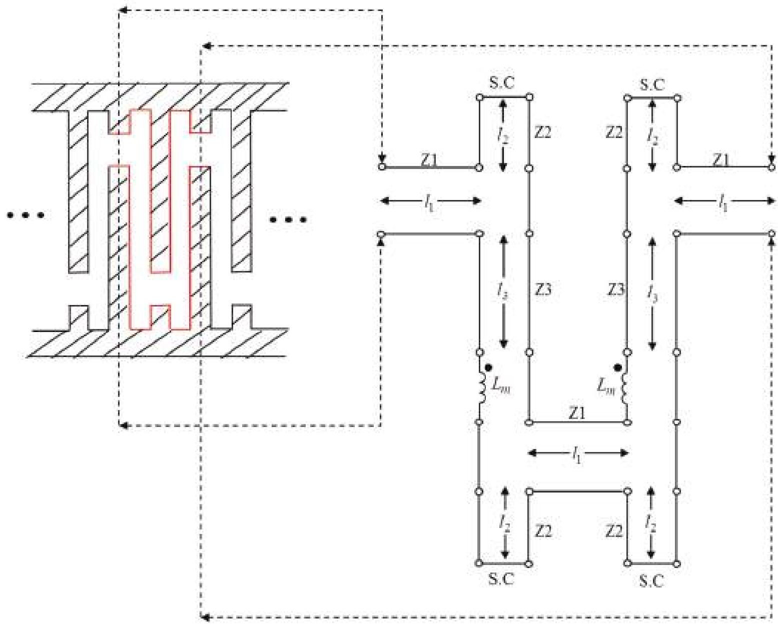

Figure 4. Transmission line equivalent circuit of the meander gap.

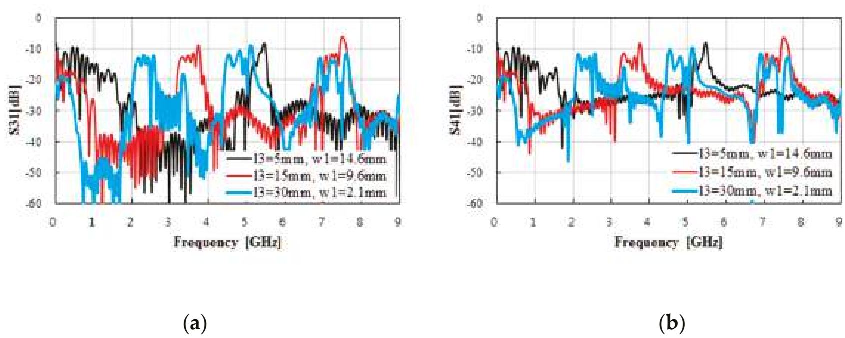

Figure 5. S_{31} (near-end crosstalk) and S_{41} (far-end crosstalk) of the meander split plane with length l_3 and w_1 changed. (**a**) S_{31}; (**b**) S_{41}.

Based on the equivalent circuit of the meander gap, the crosstalk equivalent circuit of Figure 6 can be derived for the meander split on the ground plane. The split gap can be modeled by a slot line with a transformer, which is excited by the signal line above [11]. If the spatial period of the meander structure is small enough, the signal line crosses over the split gap in a number of points, which can be modeled by transformers. It shows that if a signal line crosses over the meander split gap on the ground plane, it excites a transverse electromagnetic (TEM) mode in the mender split gap, which has a structure similar to the slot lines. The excited modes propagate in either direction and are scattered at the corners of the meander line, which impede the propagating modes. The split gap right under the signal line can be regarded as a coupled line structure, of which coupling strength can be changed by varying the longitudinal length dimension of the split.

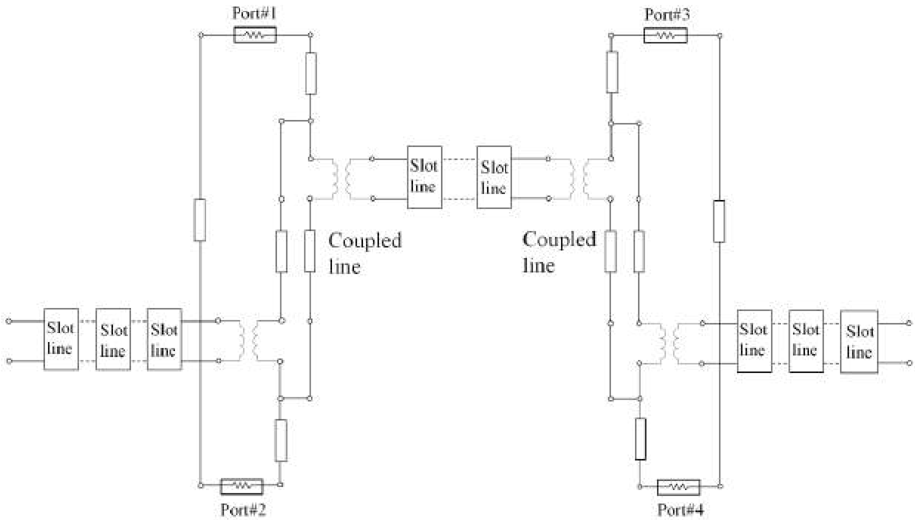

Figure 6. Crosstalk equivalent circuit of the meander split on the ground plane.

3. Results

3.1. Simulation Results of the Equivalent Circuit

Figure 7 shows the effectiveness of the equivalent circuit of Figures 4 and 5. The crosstalk behaviors of the circuit model simulated using Agilent ADS and measurement show good overall agreement about the peak and zero. At low frequencies below about 3 GHz, the LC equivalent circuit model of Figure 4 was closer to the measured result than the transmission line equivalent model of Figure 5. At high frequencies, the transmission line model was close to the measured result. The mutual inductance effect is proportional to the vertical length of the meander split and their relationship is calculated by the linear interpolation from the simulation and measured result. The crosstalk simulation result of the circuit model is slightly overestimated compared to the measured result because of the interpolation residual error of the mutual inductance value.

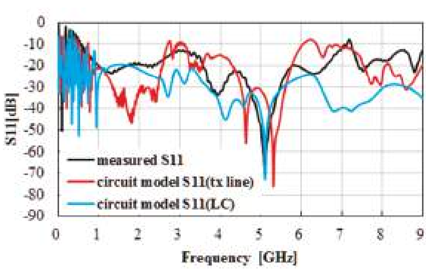

(**a**)

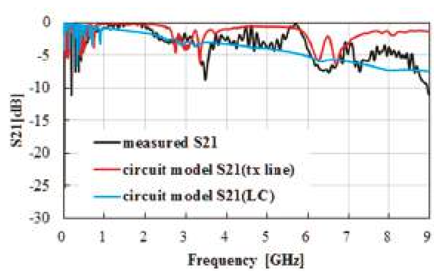

(**b**)

Figure 7. *Cont.*

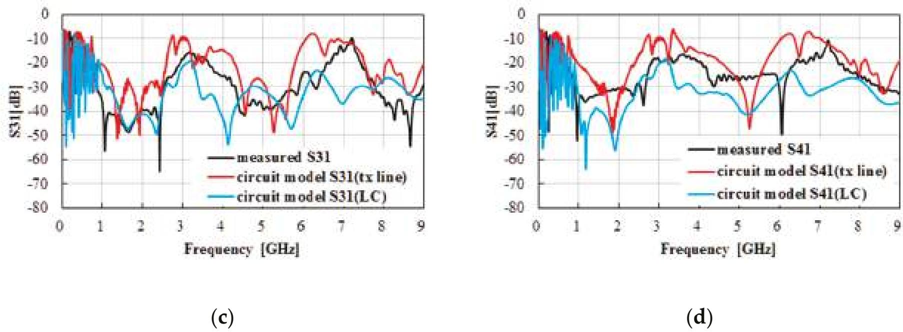

Figure 7. Scattering parameters of the simulation (circuit model) and measured result. (**a**) S_{11}; (**b**) S_{21}; (**c**) S_{31}; (**d**) S_{41}.

3.2. Reduction of Crosstalk According to the Vertical Length and Width of the Meander Split Gap

The effect of reducing the crosstalk is proportional to the vertical length l_3 and l_2 and inversely proportional to the split gap width w_2. We showed the effectiveness of those design parameters using CST Microwave studio. We set the discrete ports at the start and end point of the transmission line equivalent circuit of the meander slot line in Figure 4. Figure 8 shows the more narrowly split gap width w_2 that increases capacitive coupling and the longer length of l_3 and l_2 that causes destructive magnetic coupling with a shortened circuit line and less lateral wave propagation. The shortened circuit transmission lines (l_2) have reactance that impedes lateral wave propagation (Figure 8c). By increasing the number of cells (N) of the meander slot line, as well as varying the meander line length and split gap widths, the excited slot line mode is suppressed or attenuated (Figure 8d).

Therefore, the reduction of crosstalk at the lower and upper frequency has improved, which is desirable for digital signal transmission. The meander split gaps away from the signal line attenuate the scattered waves entering the slot line. Thanks to the evanescent mode, the periodic resonant behavior disappears, which effectively helps the signal transmission and reduces the crosstalk.

These differences come from the enhanced electromagnetic coupling between neighboring slot line sections of split planes. The meander split structure increases capacitive coupling due to the narrow split gap width, and increased length of the interaction causes destructive magnetic coupling due to the oppositely directed currents on nearby slot line sections. The capacitive coupling decreases impedance across the split gap, and the magnetic coupling increases impedances along the split. With the increased impedance, the return current cannot spread perpendicularly to the signal line. The effect causes the return current to be formed near the signal line, which helps the return current flow across the split gap without detouring. The localized return current improves signal integrity of the line traces formed over the split more effectively than the straight split.

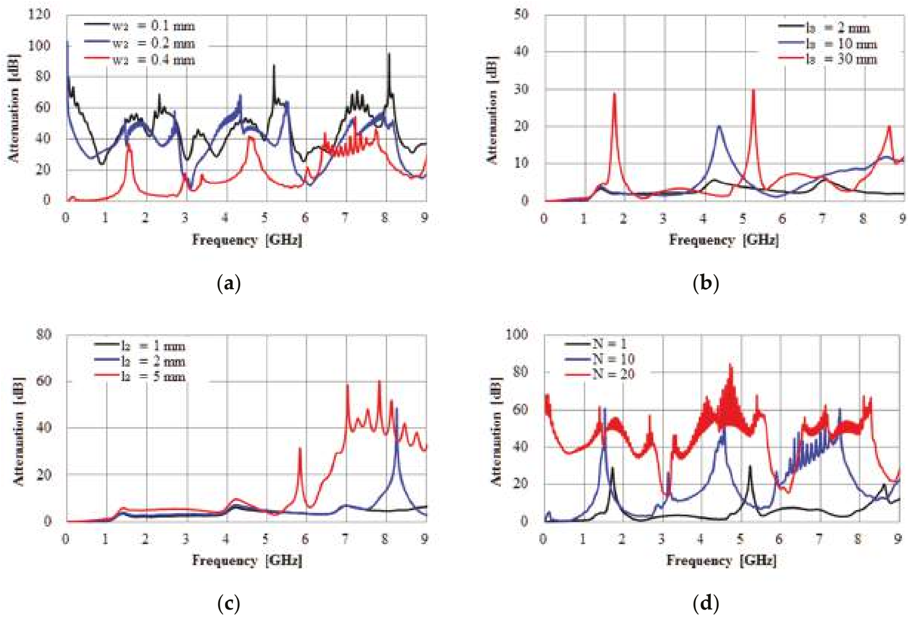

Figure 8. Lateral wave attenuation of the unit cell of the meander slot line obtained by Figure 4. (**a**) Split gap width w_2 changed (when l_1 = 0.25 mm, l_2 = 0.4 mm, l_3 = 30 mm, w_1 = 2.1 mm, $w_2 = w_3$); (**b**) length l_3 changed (when l_1 = 0.25 mm, l_2 = 0.4 mm, w_1 = 2.1 mm, $w_2 = w_3$ = 0.2 mm); (**c**) length l_2 changed (when l_1 = 0.25 mm, l_3 = 2 mm, w_1 = 2.1 mm, $w_2 = w_3$ = 0.2 mm); (**d**) number of cells changed (when l_1 = 0.25 mm, l_2 = 0.4 mm, l_3 = 30 mm, w_1 =2.1 mm, $w_2 = w_3$ = 0.2 mm.

3.3. Time Domain Crosstalk Simulation Results

The crosstalk can be explained by the current distribution on the printed circuit board. We used CST Microwave studio to obtain the current distributions of the two types of circuit boards. Figure 9 shows the surface current distribution at 2 GHz. In the case of the straight split gap, currents flow along the edge of the split and reflect at the open ends of the PCB, which enhances coupling between the two parallel signal lines and causes crosstalk. For the meander split gap, most currents cross over the meander split gap near the signal line, which shows the effectiveness of the proposed structure. Following the meander DGS split gap, the increased impedance caused by currents with alternating directions causes the crosstalk signal to be reduced effectively.

The crosstalk behavior of the transmission line equivalent circuit model for the meander DGS split is simulated in the time domain by using Agilent ADS in Figure 10. We excited a source pulse voltage $1V_{p\text{-}p}$ with 50 ohm and checked the voltage of V_3 (port #3) and V_4 (port #4). Figure 11 shows when the fast pulse signal is excited, the proposed meander DGS split decreases the crosstalk voltage at port #3 and #4 over 50% more than the straight split.

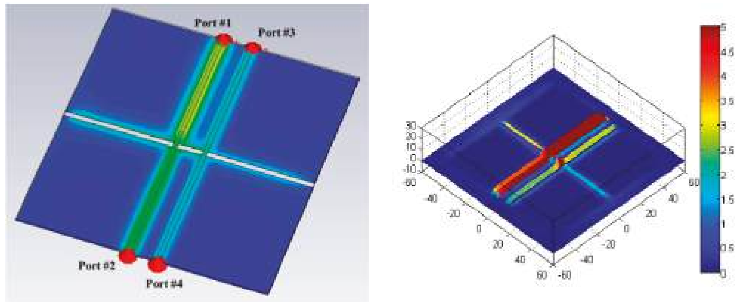

(**a**)

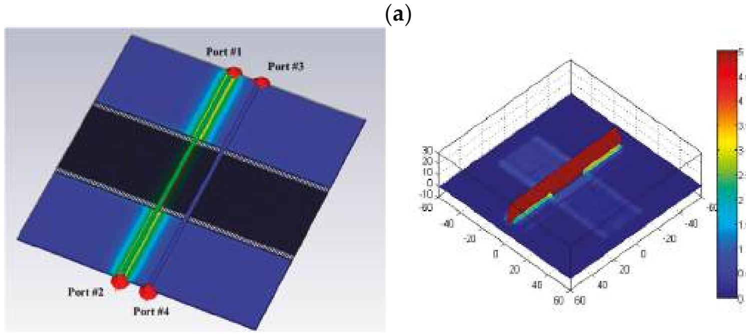

(**b**)

Figure 9. Current distributions on the straight and meander split power or ground plane at 2 GHz. (**a**) Straight split plane; (**b**) meander split plane.

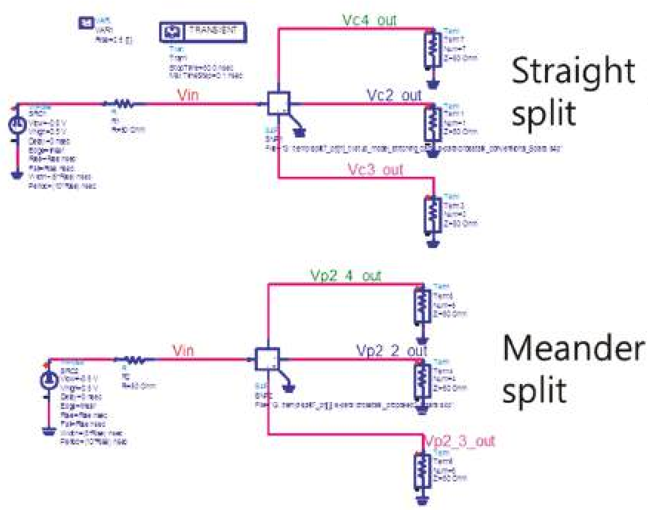

Figure 10. Time simulation of the crosstalk signal of the straight and meander split ground plane.

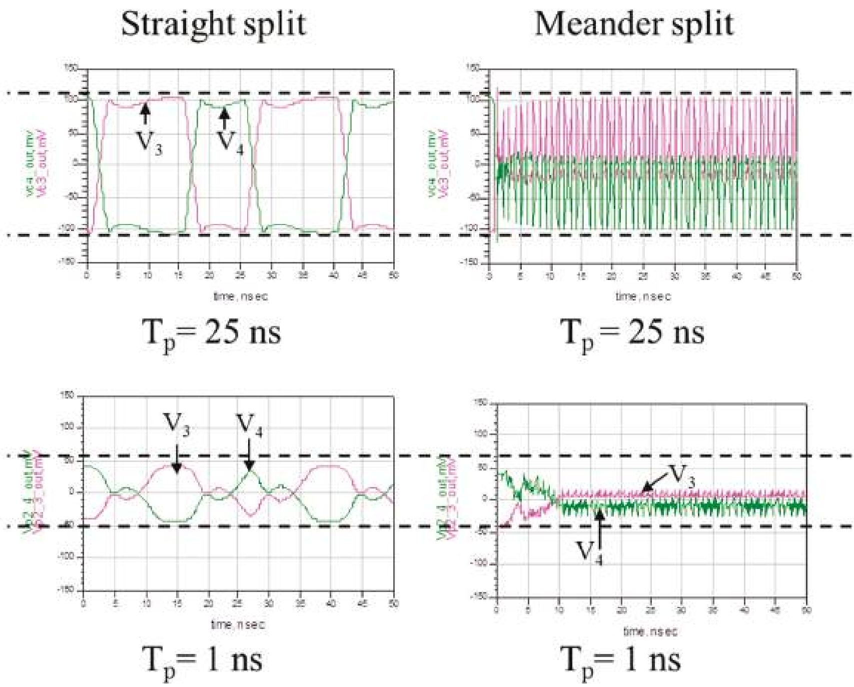

Figure 11. Time domain simulation result of Figure 10.

3.4. Time Domain Crosstalk Measurement Results

In order to demonstrate the effectiveness of the proposed split method, the crosstalk behavior of the straight and proposed split was observed experimentally in the time domain. The measurements were made by a digital oscilloscope (Tektronix TDS 6604B) and a RF signal generator (Rohde&Schwarz SML 03). The characteristic of the input RF signal is as follows. The frequency is 2 GHz, amplitude is 0.8 V. The input port #1 is fed into the RF signal generator in Figure 1. All the other ends of the lines such as port #2 (transmission), port #3 (near-end crosstalk) and port #4 (far-end crosstalk) are fed into the digital oscilloscope. Figure 12 shows the peak-to-peak voltage of the transmission signal of the meander split is larger than the straight split and it reduces near/far end crosstalk by over 50%. This behavior demonstrates that the proposed meander split power/ground plane can effectively eliminate the reflection and crosstalk due to a split gap and increase transmission bandwidth in the time domain.

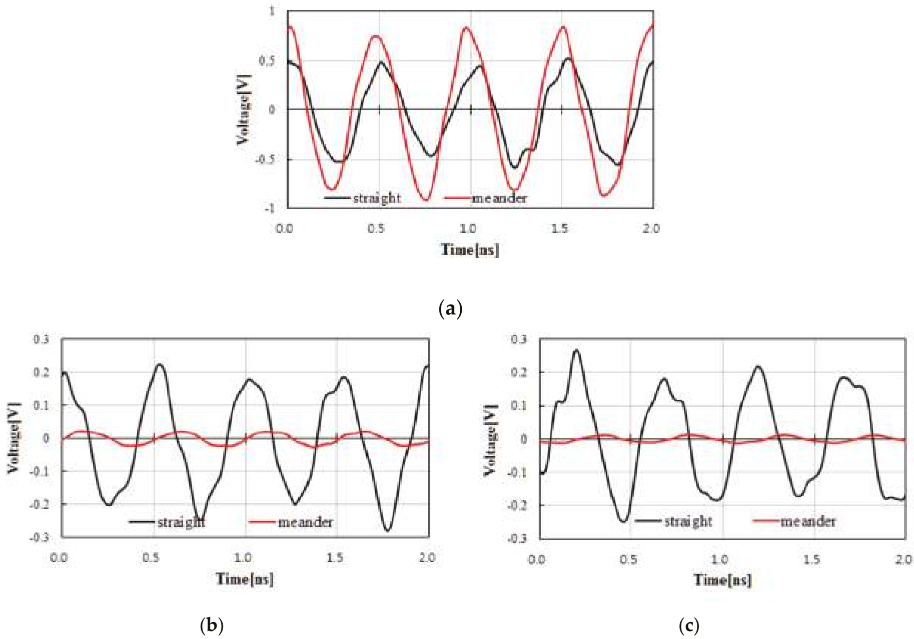

Figure 12. Comparison of the transmission and crosstalk signal with the straight and meander split power or ground plane. (**a**) Transmission signal measured at port #2; (**b**) near-end crosstalk signal measured at port #3; (**c**) far-end crosstalk signal measured at port #4.

4. Conclusions

A novel meander DGS is proposed to improve the transmission bandwidth and reduce the crosstalk of the two parallel microstrip lines over split power/ground planes. It employs a meander split to enhance electromagnetic coupling and suppress propagation of lateral waves to make signal return current flow across the split formed in the power/ground plane along the signal line in proximity, which helps reduce the crosstalk effectively. We have presented a design method for the main parameters l_3 and w_2 of the meander DGS that enhanced electromagnetic coupling and reduced the crosstalk. We developed the LC equivalent circuit and transmission line equivalent circuit model for analyzing the crosstalk. The validity of the equivalent circuit model was verified by comparison with measurement and simulation results and it shows overall good agreement with slight overestimation due to the mutual inductance interpolation error. Experimental results show that the proposed meander DGS improves signal quality and reduces near/far end crosstalk over 30 dB up to 9 GHz and 50% in the frequency domain and time domain, respectively.

Author Contributions: Conceptualization, methodology, investigation, writing-original draft preparation, writing-review and editing, J.-H.L.

Funding: This research was funded by Korea Institute of Ocean Science & Technology, grant number PE99741.

Acknowledgments: This research was part of the project titled "Development of maritime defense and security technology [PE99741]" funded by Korea Institute of Ocean Science & Technology in 2019.

Conflicts of Interest: The author declares no conflict of interest.

References

1. Fan, J.; Ren, Y.; Chen, J.; Hockanson, D.M.; Shi, H.; Drewniak, J.L.; Hubing, T.H.; Van Doren, T.P.; DuBroff, R.E. RF isolation using power islands in DC power bus design. In Proceedings of the 1999 IEEE International Symposium on Electromagnetic Compatability. Symposium Record (Cat. No. 99CH36261), Seattle, WA, USA, 2–6 August 1999; pp. 838–843.
2. Miller, J.R. The impact of split power planes on package performance. In Proceedings of the 2001 Proceedings. 51st Electronic Components and Technology Conference (Cat. No. 01CH37220), Orlando, FL, USA, 29 May–1 June 2001; pp. 1117–1121.
3. Liaw, H.-J.; Merkelo, H. Signal integrity issues at split ground and power planes. In Proceedings of the 1996 Proceedings 46th Electronic Components and Technology Conference, Orlando, FL, USA, 28–31 May 1996; pp. 752–755.
4. Shim, H.-Y.; Kim, J.; Yook, J.-G. Modeling of ESD and EMI problems in split multi-layer power distribution network. In Proceedings of the 2003 IEEE Symposium on Electromagnetic Compatibility. Symposium Record (Cat. No. 03CH37446), Boston, MA, USA, 18–22 August 2003; pp. 48–51.
5. Cui, W.; Fan, J.; Ren, Y.; Shi, H.; Drewniak, J.; Dubroff, R. DC power-bus noise isolation with power-plane segmentation. *IEEE Trans. Electromagn. Compat.* **2003**, *45*, 436–443. [CrossRef]
6. Johnson, H.W.; Graham, M. *High-Speed Digital Design: A Handbook of Black Magic*; Prentice Hall: Upper Saddle River, NJ, USA, 1993.
7. Shuppert, B. Microstrip/slotline transitions: Modeling and experimental investigation. *IEEE Trans. Microwave Theory Tech.* **1988**, *36*, 1272–1282. [CrossRef]
8. Duan, D.-W.; Rubin, B.J.; Magerlein, J. Distributed effects of a gap in power/ground planes. In Proceedings of the IEEE 8th Topical Meeting on Electrical Performance of Electronic Packaging (Cat. No. 99TH8412), San Diego, CA, USA, 25–27 October 1999; pp. 207–210.
9. Schuster, C.; Fichtner, W. Parasitic modes on printed circuit boards and their effects on EMC and signal integrity. *IEEE Trans. Electromagn. Compat.* **2001**, *43*, 416–425. [CrossRef]
10. Moran, T.; Virga, K.; Aguirre, G.; Prince, J. Methods to reduce radiation from split ground planes in RF and mixed signal packaging structures. *IEEE Trans. Adv. Packag.* **2002**, *25*, 409–416. [CrossRef]
11. Xiao, F.; Nakada, Y.; Murano, K.; Kami, Y. Crosstalk analysis model for traces crossing split ground plane and its reduction by stitching capacitor. *Electron. Commun. Jpn. (Part II: Electron.)* **2007**, *90*, 26–34. [CrossRef]
12. Suntives, A.; Khajooeizadeh, A.; Abhari, R. Using via fences for crosstalk reduction in PCB circuits. In Proceedings of the 2006 IEEE International Symposium on Electromagnetic Compatibility, Portland, OR, USA, 14–18 August 2006; pp. 34–37.
13. Mbairi, F.D.; Siebert, W.P.; Hesselbom, H. On The Problem of Using Guard Traces for High Frequency Differential Lines Crosstalk Reduction. *IEEE Trans. Compo. Packag. Technol.* **2007**, *30*, 67–74. [CrossRef]
14. Huang, W.-T.; Lu, C.-H.; Lin, D.-B. SUPPRESSION OF CROSSTALK USING SERPENTINE GUARD TRACE VIAS. *Prog. Electromagn. Res.* **2010**, *109*, 37–61. [CrossRef]
15. Koo, S.-K.; Lee, H.; Park, Y.B. Crosstalk Reduction Effect of Asymmetric Stub Loaded Lines. *J. Electromagn. Waves Appl.* **2011**, *25*, 1156–1167. [CrossRef]
16. Chu, S.T.; Little, B.; Pan, W.; Kaneko, T.; Kokubun, Y. Cascaded microring resonators for crosstalk reduction and spectrum cleanup in add-drop filters. *IEEE Photonics Technol. Lett.* **1999**, *11*, 1423–1425.
17. Cai, Q.-M.; Yu, X.-B.; Zhang, L.; Zhu, L.; Zhang, C.; Ren, Y.; Fan, J. Far-End Crosstalk Mitigation in DDR5 Using Graphene-Paraffin Material Coated Signal Lines with Tabs. In Proceedings of the 2019 Cross Strait Quad-Regional Radio Science and Wireless Technology Conference (CSQRWC 2019), Taiyuan, China, 18–21 July 2019; pp. 1–3.
18. Zhang, L.; Cai, Q.-M.; Yu, X.-B.; Zhu, L.; Zhang, C.; Ren, Y.; Fan, J. Far-End Crosstalk Mitigation for Microstrip Lines in High-Speed PCBs. In Proceedings of the 2019 Cross Strait Quad-Regional Radio Science and Wireless Technology Conference (CSQRWC 2019), Taiyuan, China, 18–21 July 2019; pp. 1–3.
19. Lee, S.-K.; Lee, K.; Park, H.-J.; Sim, J.-Y. FEXT-eliminated stub-alternated microstrip line for multi-gigabit/second parallel links. *Electron. Lett.* **2008**, *44*, 272–273. [CrossRef]
20. Roden, J.A.; Archambeault, B.; Lyle, R.D. Effect of stitching capacitor distance for critical traces crossing split reference planes. In Proceedings of the 2003 IEEE Symposium on Electromagnetic Compatibility. Symposium Record (Cat. No. 03CH37446), Boston, MA, USA, 18–22 August 2003; pp. 703–707.

21. Lin, D.-B.; Shen, R.-H. The improvement of signal quality and far-end crosstalk for coupled microstrip line over a completely split ground plane. In Proceedings of the 2012 IEEE Electrical Design of Advanced Packaging and Systems Symposium (EDAPS 2012), Taipei, Taiwan, 9–11 December 2012; pp. 139–141.
22. Kim, J.; Lee, H.; Kim, J. Effects on signal integrity and radiated emission by split reference plane on high-speed multilayer printed circuit boards. *IEEE Trans. Adv. Packag.* **2005**, *28*, 724–735.
23. Chuang, H.-H.; Wu, T.-L. Suppression of Common-Mode Radiation and Mode Conversion for Slot-Crossing GHz Differential Signals Using Novel Grounded Resonators. *IEEE Trans. Electromagn. Compat.* **2011**, *53*, 429–436. [CrossRef]
24. Chuang, H.-H.; Chou, C.-C.; Chang, Y.-J.; Wu, T.-L. A Branched Reflector Technique to Reduce Crosstalk between Slot-Crossing Signal Lines. *IEEE Microwave Wireless Compon. Lett.* **2012**, *22*, 342–344. [CrossRef]
25. Mandal, M.K.; Sanyal, S. A novel defected ground structure for planar circuits. *IEEE Microwave Wireless Compo. Lett.* **2006**, *16*, 93–95. [CrossRef]
26. Chen, H.-J.; Huang, T.-H.; Chang, C.-S.; Chen, L.-S.; Wang, N.-F.; Wang, Y.-H.; Houng, M.-P. A novel cross-shape DGS applied to design ultra-wide stopband low-pass filters. *IEEE Microwave Wireless Components Lett.* **2006**, *16*, 252–254. [CrossRef]
27. Woo, D.-J.; Lee, T.-K.; Lee, J.-W.; Pyo, C.-S.; Choi, W.-K. Novel U-slot and V-slot DGSs for bandstop filter with improved Q factor. *IEEE Trans. Microwave Theory Tech.* **2006**, *54*, 2840–2847.
28. Kim, C.-S.; Park, J.-S.; Ahn, D.; Jae-Bong, L. A novel 1-D periodic defected ground structure for planar circuits. *IEEE Microwave Guided Wave Lett.* **2000**, *10*, 131–133.
29. Balalem, A.; Ali, A.R.; Machac, J.; Omar, A. Quasi-Elliptic Microstrip Low-Pass Filters Using an Interdigital DGS Slot. *IEEE Microwave Wireless Compon. Lett.* **2007**, *17*, 586–588. [CrossRef]
30. Liu, W.-T.; Tsai, C.-H.; Han, T.-W.; Wu, T.-L. An Embedded Common-Mode Suppression Filter for GHz Differential Signals Using Periodic Defected Ground Plane. *IEEE Microwave Wireless Compon. Lett.* **2008**, *18*, 248–250.
31. Henridass, A.; Sindhadevi, M.; Karthik, N.; Alsath, M.G.N.; Kumar, R.R.; Malathi, K. Defective ground plane structure for broadband crosstalk reduction in PCBs. In Proceedings of the 2012 International Conference on Computing, Communication and Applications, Dindigul, India, 22–24 February 2012; pp. 1–5.
32. Khandelwal, M.K.; Kanaujia, B.K.; Kumar, S. Defected Ground Structure: Fundamentals, Analysis, and Applications in Modern Wireless Trends. *Int. J. Antennas Propag.* **2017**, *2017*, 1–22. [CrossRef]
33. Curnow, H. A General Equivalent Circuit for Coupled-Cavity Slow-Wave Structures. *IEEE Trans. Microwave Theory Tech.* **1965**, *13*, 671–675. [CrossRef]
34. Abbosh, A.M.; Bialkowski, M.E. Deriving characteristics of the slotline using the conformal mapping technique. In Proceedings of the MIKON 2008-17th International Conference on Microwaves, Radar and Wireless Communications, Wroclaw, Poland, 19–21 May 2008; pp. 1–4.

electronics

MDPI

Article

A Dual-Perforation Electromagnetic Bandgap Structure for Parallel-Plate Noise Suppression in Thin and Low-Cost Printed Circuit Boards

Myunghoi Kim

Department of Electrical, Electronic, and Control Engineering, and the Institute for Information Technology Convergence, Hankyong National University, Anseong 17579, Korea; mhkim80@hknu.ac.kr; Tel.: +82-31-670-5295

Received: 27 May 2019; Accepted: 21 June 2019; Published: 25 June 2019

Abstract: In this study, we propose and analyze a dual-perforation (DP) technique to improve an electromagnetic bandgap (EBG) structure in thin and low-cost printed circuit boards (PCBs). The proposed DP–EBG structure includes a power plane with a square aperture and a patch with an L-shape slot that overcomes efficiently the problems resulting from the low-inductance and the characteristic impedance of the EBG structure developed for parallel-plate noise suppression in thin PCBs. The effects of the proposed dual-perforation technique on the stopband characteristics and unit cell size are analyzed using an analytical dispersion method and full-wave simulations. The closed-form expressions for the main design parameters of the proposed DP–EBG structure are extracted as a design guide. It is verified based on full-wave simulations and measurements that the DP technique is a cost-effective method that can be used to achieve a size reduction and a stopband extension of the EBG structure in thin PCBs. For the same unit cell size and low cut-off frequency, the DP–EBG structure increases the stopband bandwidth by up to 473% compared to an inductance-enhanced EBG structure. In addition, the unit cell size is substantially reduced by up to 94.2% compared to the metallo–dielectric EBG structure. The proposed DP–EBG technique achieves the wideband suppression of parallel plate noise and miniaturization of the EBG structure in thin and low-cost PCBs.

Keywords: electromagnetic bandgap (EBG); dual perforation (DP); parallel-plate noise; power delivery network (PDN); printed circuit board (PCB)

1. Introduction

Design complexity of high-speed digital and microwave printed circuit boards (PCBs) continues to increase as high-speed PCBs are fully populated with heterogeneous circuits and associated interconnects. High-speed PCB design is a complicated and heavily constrained problem due to the requirement to ensure reliable power delivery in the presence of multiple voltage levels and optimized signal traces within restricted routing regions. Moreover, small-form factors and cost reduction are preferred. To solve this complex problem, multilayer PCB technology, including thin and low-cost dielectrics, such as epoxy–resin fiberglass (e.g., FR–4) dielectric materials, is extensively employed in high-speed digital and microwave applications. Use of a thin dielectric provides advantages of inductance reductions when signals or planes are vertically connected, and when narrow transmission lines are used for highly dense interconnections. Additionally, a thin dielectric increases the static capacitance of PCB planes, thus achieving low-plane impedance for power delivery networks [1]. This reduces the effort of designing and optimizing decoupling capacitors for noise suppressions.

However, recent circuit operations of high-speed switching and high-bandwidth data transfers generate wideband and high-frequency noise in PCB power delivery networks that cannot be reduced or suppressed by the low-impedance characteristics of thin PCBs. In particular, parallel-plate noise is a serious problem because it significantly affects system performance. Moreover, it is induced by a parallel-plate waveguide that is frequently adopted for power delivery networks in high-speed PCBs [2–6].

One of the methods used to suppress wideband and high-frequency parallel-plate noise in high-speed PCBs is a power delivery network based on an electromagnetic bandgap (EBG) structure. To-this-date, various EBG structures have been introduced [7–22]. Their characteristics of parallel-plate noise suppression are superior. The EBG structures exhibit increased levels of noise suppression over a wideband frequency range. They are easily implemented by metal patterning of conductive layers, and can thus be simply integrated into PCBs. One promising approach introduced in previously conducted researches is the EBG structure [12–22]. This technique is based on a shunt LC resonator, whereby the capacitance and inductance are respectively induced by an embedded metal patch and a via. These EBG structures have been studied extensively and a variety of cost-effective techniques have been presented for the improvement of the stopband and the miniaturization of an EBG unit cell [12–22].

To reduce a unit cell size of an EBG structure with cost-effective PCB technology, various methods using edge-located vias and inductance-enhanced patch have been proposed. The EBG structure that uses an edge-located via [12,13] increases the inductance value of the shunt LC resonator by simply moving the via to the patch edge. In inductance-enhanced EBG structures [14–18], a resonant patch is perforated with the use of various patterns, such as spiral-shaped, stub-like, I-type patterns, so that the effective inductances in the equivalent circuit of a unit cell substantially increase.

These methods efficiently increase the inductance value of a shunt LC resonator using low-cost PCB technology. Hence, decreases of the low-cutoff frequency can result in the miniaturization of EBG structures. However, the drawback of these techniques is the significant reduction of the stopband bandwidth. The stopband bandwidth is at most 1 GHz to suppress the parallel-plate noise in the low-frequency range of 1–2 GHz.

To enhance the stopband bandwidth, an EBG structure using multiple vias is presented in [19,20]. In the multivia EBG structure, the equivalent inductance of a shunt LC resonator is reduced by the parallel connection between the vias. The multivia approach substantially increases the stopband bandwidth without changing the EBG size and without increasing manufacturing cost. However, its drawback is a low-cutoff frequency which is shifted to a high frequency, and which results in the increase of the unit cell size to suppress parallel-plate noise in the low-frequency range. Furthermore, the multivia approach is less effective in thin PCBs because the inductance effect on the stopband is not dominant for thin dielectrics.

Other methods used for stopband improvements employed defected ground structures (DGSs) [21–24]. The plane that is connected to a resonant patch through a via is etched by particular patterns so that the characteristic impedance (Z_o) increases in an equivalent EBG unit cell circuit. A stopband bandwidth significantly increases, while a low-cutoff frequency of the DGS–EBG structure is not shifted to a high frequency. While its stopband expansion is prominent, the DGS–EBG structure does not have the advantage of miniaturizing an EBG structure in thin PCBs. Consequently, it is necessary to develop a new technique to simultaneously achieve increases of the stopband bandwidth and size reductions of the EBG structure in thin PCBs.

In this study, a dual-perforation technique is proposed for a miniaturized and wideband EBG structure to mitigate parallel-plate noise in thin and low-cost PCBs. The study is organized as follows: (1) in Section 2, the proposed EBG structure is presented, and its improved features are completely explained using dispersion analysis based on the close-form expressions for low and high cut-off frequencies and full-wave simulation approaches based on finite element method. (2) In Section 3, the proposed EBG structure is validated using the scattering parameters which are obtained using the full-wave simulations and experimental results. (3) The conclusions of the study are outlined in Section 4.

2. Dual-Perforation EBG Structure

2.1. Design Description

The proposed dual-perforation EBG (DP–EBG) structure is developed to suppress parallel-plate noise in multilayer PCBs, including thin dielectrics. The DP–EBG structure is a periodic structure in which a unit cell comprises a perforated power plane, a perforated patch, and a ground plane embedded in a thin dielectric, as shown in Figure 1. The power plane is perforated by four square apertures, while the resonant patch is perforated by an L-shape slot. These perforations are simple to implement with conventional PCB manufacturing techniques without requiring additional, costly processes. The perforated power plane and patch are connected through a short-length via owing to the thin dielectric. The apertures in the power plane electrically enhance the characteristic impedance of the EBG unit cell, while the L-shape slot in the resonant patch effectively increases the inductance of the EBG unit cell. The unit cell size and square aperture of the DP–EBG structure are represented as d_c–by–d_c and d_a–by–d_a structures, respectively. Therefore, the width of the remaining conductor is the same and equal to d_c-2d_a. Regarding the L-shape slot, the conductor width etched on the patch is denoted by $\mathrm{w_s}$ and the width of the remaining conductor is denoted by $\mathrm{w_b}$. The sum of $\mathrm{d_p}/2$ and $\mathrm{d_s}$ is the total length of the L-shape slot. The design parameter $\mathrm{d_s}$ is adjustable to obtain a desired patch inductance. The dielectric thickness between the dual perforated planes is $\mathrm{h_1}$. The distance between the perforated patch and the ground plane is $\mathrm{h_2}$.

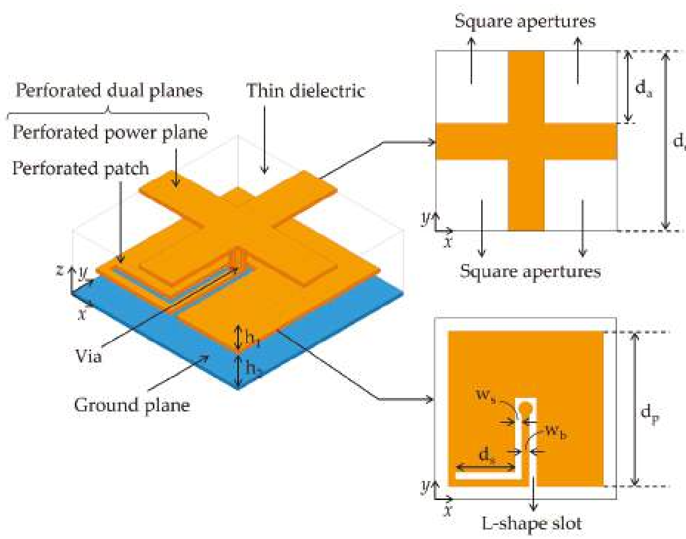

Figure 1. A unit cell of a dual-perforation electromagnetic bandgap dual-perforation–electromagnetic bandgap (DP–EBG) structure consisting of perforated dual planes and its design parameters.

2.2. Derivation of the Equations for f_L and f_H

Dispersion analysis is performed to examine the dual-perforation effects on the stopband of the DP–EBG structure. To derive an analytical dispersion equation, a two-port equivalent circuit model based on transmission line theory is considered, as shown in Figure 2. In this study, one-dimensional (1–D) propagation is captured by the equivalent circuit. The dispersion analysis conducted with the use of the 1–D circuit model can be extended to a 2–D EBG array because it shows good correlation with the prediction of noise suppression in the 2–D EBG array. The DP–EBG circuit model consists of two transmission lines and a resonator circuit in which an inductor and a capacitor are connected in series. At the resonant frequency, the LC resonator has zero impedance which results in the decoupling of parallel-plate noise. The transmission line is the circuital representation of electromagnetic waves propagating through the parallel plate waveguide, which is formed by the perforated power and the ground planes. In the DP–EBG circuit model, Z_{eq} and β_c respectively denote the characteristic impedance and propagation constant of this parallel plate waveguide or transmission line. Its length is $d_c/2$. In the transmission line model, Z_{eq} is significantly enhanced by the square perforation aperture because the width of the remaining conductor perpendicular to the direction of wave propagation is narrowed. In the resonator circuit, the capacitance C_p is attributed to the capacitor between the resonant patch and the corresponding ground plane, while the inductance is attributed to the patch and the via inductances. For the DP–EBG structure in the thin PCBs, the inductance of the via can be ignored compared to the patch inductance which substantially increases due to the L-shape slot. Thus, the value of L_{eq} in the DP–EBG circuit model is mainly determined by the L-shape slot on the perforated resonant patch. Hence, the equivalent circuit of the proposed DP–EBG structure is expressed with a Z_o-enhanced transmission line and an L-enhanced resonator.

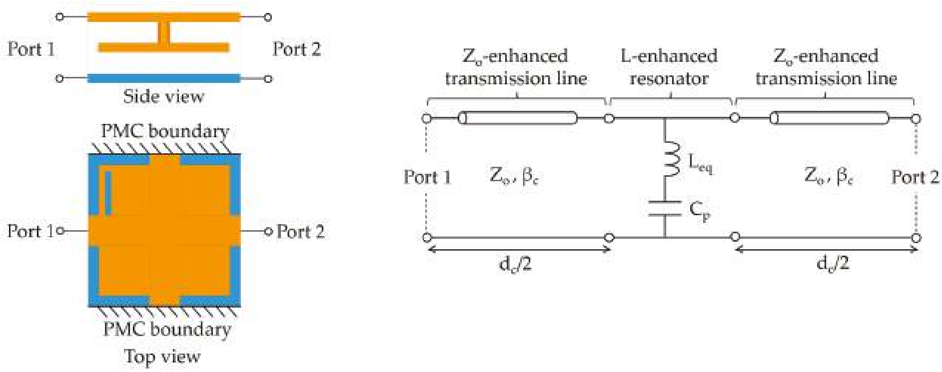

Figure 2. Equivalent circuit model of the DP–EBG unit cell based on transmission line theory for the extraction of the dispersion equation.

Using the ABCD parameters of the microwave theory, the voltage/current relationships between ports 1 and 2 of the DP–EBG unit cell are described by [22]

$$\begin{pmatrix} \cos(\beta_{uc}d_c) & jZ_{uc}\sin(\beta_{uc}d_c) \\ jZ_{uc}^{-1}\sin(\beta_{uc}d_c) & \cos(\beta_{uc}d_c) \end{pmatrix} = \begin{pmatrix} \cos\left(\frac{\beta_c d_c}{2}\right) & jZ_{eq}\sin\left(\frac{\beta_c d_c}{2}\right) \\ jZ_{eq}^{-1}\sin\left(\frac{\beta_c d_c}{2}\right) & \cos\left(\frac{\beta_c d_c}{2}\right) \end{pmatrix} \begin{pmatrix} 1 & 0 \\ Y_R & 1 \end{pmatrix} \begin{pmatrix} \cos\left(\frac{\beta_c d_c}{2}\right) & jZ_{eq}\sin\left(\frac{\beta_c d_c}{2}\right) \\ jZ_{eq}^{-1}\sin\left(\frac{\beta_c d_c}{2}\right) & \cos\left(\frac{\beta_c d_c}{2}\right) \end{pmatrix} \tag{1}$$

where,

$$Y_R = \frac{j(2\pi f)C_p}{1-(2\pi f)^2 L_{eq}C_p} \tag{2}$$

From the equations listed above, an effective phase constant β_{uc} of the DP–EBG unit cell is derived by

$$\beta_{uc} = \frac{1}{d_c}\cos^{-1}\left[\cos(\beta_c d_c) - \frac{(2\pi f)C_p Z_{eq}}{2\left(1-(2\pi f)^2 C_p L_{eq}\right)}\sin(\beta_c d_c)\right]. \tag{3}$$

Closed-form expressions for low and high-cutoff frequencies (f_L and f_H) are further extracted from (3). To derive a closed-form expression for f_L, it is considered that the real part of β_{uc} is equal to π/d_c (i.e., $Re\{\beta_{uc}\} = \pi/d_c$). It is assumed that the electrical length of $\beta_c d_c$ for f_L is small enough to set cos($\beta_c d_c$) and sin($\beta_c d_c$) to 1 and $\beta_c d_c$, respectively. Accordingly, the following equation is obtained from (3),

$$1 = \left(\frac{\pi f_L C_p Z_{eq}}{2\left(1 - (2\pi f_L)^2 C_p L_{eq}\right)} \right) \left(\frac{2\pi f_L d_c}{v_p} \right). \tag{4}$$

where v_p is the phase velocity of $c/\sqrt{\varepsilon_r}$, and c is the speed of light in vacuum. Based on Equation (4), an analytical equation can be derived explicitly for $f_{L,}$ as follows,

$$f_L = \frac{1}{2\pi} \left(\frac{1}{4 Z_{eq} C_p d_c v_p^{-1} + L_{eq} C_p} \right)^{1/2} \tag{5}$$

As it can be observed in Equation (5), f_L is expected to be reduced when Z_{eq} and L_{eq} increase, when the DP technique is used, which are associated with the perforations of a power plane and a resonant patch. L_{eq} mainly contributes to the reduction in $f_{L,}$ while the Z_{eq} effect is limited because it is divided by the phase velocity v_p.

To obtain an explicit expression for f_H, it is considered that $\beta_{uc} d_c = 0$ or cos($\beta_{uc} d_c$) = 1. Thus, Equation (3) may be simplified to

$$tan\left(\frac{\beta_c d_c}{2} \right) = -\frac{(2\pi f_H) C_p Z_{eq}}{2\left(1 - (2\pi f_H)^2 C_p L_{eq}\right)} \tag{6}$$

Accordingly, Equation (6) can be approximated using two assumptions. First, d_c is so small compared to the wavelength of f_H which results in tan($\beta_c d_c$/2) ≈ $\beta_c d_c$/2.

Second, f_H is higher than the resonant frequency determined by the $C_p L_{eq}$ product. Thus, (1-$(2\pi f_H)^2 C_p L_{eq}$) is approximated to be equal to -$(2\pi f_H)^2 C_p L_{eq}$. Consequently, (6) becomes

$$f_H = \frac{1}{2\pi} \left(\frac{Z_{eq}}{L_{eq}} \frac{v_p}{d_c} \right)^{1/2} \tag{7}$$

It is observed in Equation (7) that f_H can be shifted to lower the frequency values by increasing L_{eq} with the resonant patch perforated by the L-shape slot. Considering the factor L_{eq} in Equations (6) and (7), the f_H reduction rate is higher than that of f_L because f_H is inversely proportional to $(L_{eq})^{1/2}$. However, increasing Z_{eq}, induced from the power plane perforated using rectangular apertures, compensates this bandwidth reduction in the proposed DP–EBG structure.

2.3. Dispersion Analysis

To validate the f_L and f_H equations and examine the DP technique effects on the stopband characteristics of the DP–EBG structure, a full-wave simulation based on a finite element method (FEM) is adopted, and the results are compared with those from Equations (5) and (7). FEM simulations were performed using the commercial software HFSS (ver. 17.1, Ansys. Corp., Pittsburgh, PA, USA). The FEM simulation model used for the dispersion analysis of the DP–EBG structure is identical to the unit cell shown in Figure 1. In the simulation model, the nominal values of the design parameters of d_c, d_p, d_a, w_s, w_b, d_s, h_1, and $h_{2,}$ are set to 5 mm, 4.9 mm, 2.45 mm, 0.1 mm, 0.1 mm, 2.2 mm, 0.1 mm, and 0.1 mm, respectively. These values were determined based on the consideration of a conventional and low-cost PCB process. The dimensions of the geometrical parameters are summarized in Table 1. The dielectric thicknesses of h_1 and h_2 are chosen as the minimum value provided by the cost-effective PCB process. The dielectric constant and loss tangent of the FR–4 are 4.4 and 0.02, respectively. The aperture size d_a and the L-shape slot length d_s are respectively related with Z_{eq} and L_{eq}. The parameters d_a and d_s were varied to comprehensively examine the stopband characteristics of the DP–EBG structure and to verify the closed-form expressions for f_L and f_H of Equations (5) and (7). The d_a values of 2.15, 2.25, 2.35, and 2.45 mm, are employed which correspond to the Z_{eq} values of 33, 41, 56, and 90 Ω. The d_s values changed from 0.15 mm to 2.3 mm and coincided with the L_{eq} values from 1.55 nH to 2.38 nH. The Z_{eq} and L_{eq} values associated with the geometrical dimensions were simply obtained using quasistatic simulations.

Table 1. Dimensions of geometrical parameters of the DP–EBG structure.

Parameters	d_c	d_p	d_a	w_s	w_b	d_s	h_1	h_2
Dimensions (mm)	5	4.9	2.45	0.1	0.1	2.2	0.1	0.1

Figure 3 depicts the f_L and f_H values of the stopband characteristics with the aforementioned Z_{eq} and L_{eq} values, as acquired from the FEM simulations (blue lines) and the proposed equations (red lines). The results for Z_{eq} of 33, 41, 56, and 90 Ω, are shown in Figure 3a–d, respectively. The closed-form expressions for f_L and f_H exhibit good correlations with the FEM-based full-wave simulations, as shown in all the figures. The discrepancies associated with f_H may result from the first-order approximation of the Taylor series expansion of the tangent function. However, the differences between the FEM simulation and the closed-form expressions are approximately uniform for all the L_{eq} values. Thus, the tendencies among these results are in close agreement. Even though the closed-form expressions for f_L and f_H derived herein are verified using a limited number of test cases, these equations can be extended and applied to other DP–EBG structures, including the different dimensions of geometrical parameters.

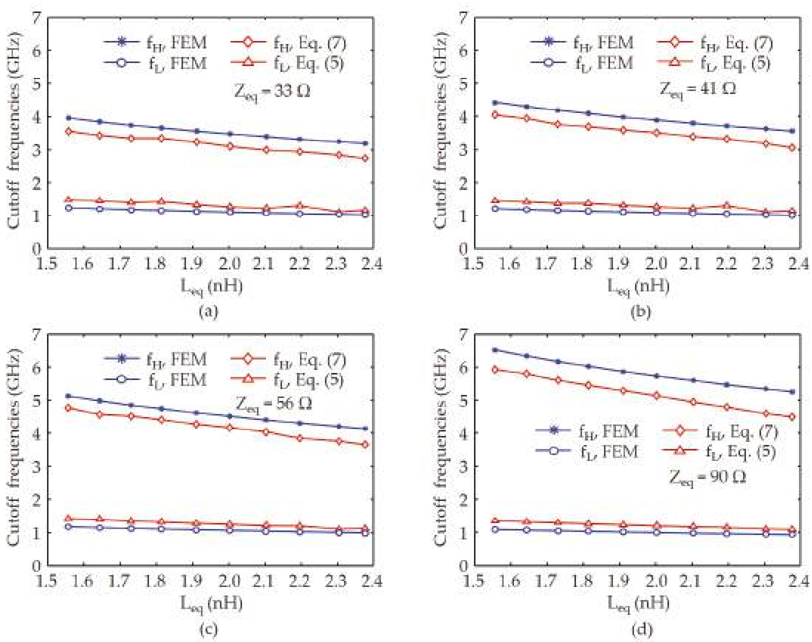

Figure 3. Various cutoff frequencies with respect to the changes of Z_{eq} ((**a**) 33 Ω, (**b**) 41 Ω, (**c**) 56 Ω and (**d**) 90 Ω) and L_{eq} used to examine the stopband characteristics and verify the closed-form expressions for f_L and f_H.

The effects of the DP technique on a stopband are further examined. The f_L and f_H variations with respect to Z_{eq} and L_{eq} are explored using Equations (5) and (7), as shown in Figure 4. The value of Z_{eq} varies from 5 Ω to 95 Ω and that of L_{eq} changes from 1.0 nH to 3.0 nH. These values are commonly used for the proposed DP–EBG structure in low-cost and thin PCBs. The overall tendencies of the variations of f_L and f_H associated with the DP technique are also observed and evaluated. In Figure 4a, the minimum f_L value is 0.85 GHz when Z_{eq} and L_{eq} are 95 Ω and 3.0 nH, respectively. The maximum value of f_L is 1.63 GHz and results from Z_{eq} = 5 Ω and L_{eq} = 1.0 nH. As shown in Figure 4b, the minimum value of f_H is 1.10 GHz and is observed when Z_{eq} = 5 Ω and L_{eq} = 3.0 nH, while the DP–EBG structure has a maximum value of f_H is 8.34 GHz when Z_{eq} = 95 Ω and L_{eq} = 1.0 nH. The conditions for the minimum and maximum f_L and f_H values are different.

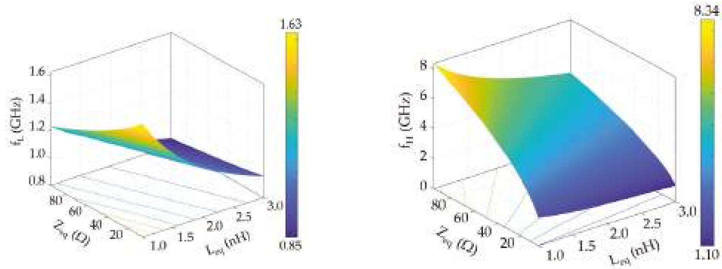

(**a**) (**b**)

Figure 4. Variations of (**a**) f_L and (**b**) f_H for various Z_{eq} and L_{eq} values obtained using the closed-form expressions.

To gain insight into the efficient design of the DP–EBG structure, the variations of f_L and f_H are presented graphically. Figure 5 depicts the contour lines of both f_L (black dashed lines) and f_H (blue solid lines) when Z_{eq} changes from 5 Ω to 95 Ω and when L_{eq} changes from 1.0 nH to 3.0 nH. Point A in Figure 5 shows that f_L and f_H are equal to 1.23 GHz and 4.42 GHz when Z_{eq} and L_{eq} are 40 Ω and 1.5 nH, respectively. However, the suppression region of the parallel-plate noise given at point A needs to be extended in the low-frequency range. To achieve this, L_{eq} can increase. For instance, f_L changes from 1.23 GHz to 1.0 GHz as L_{eq} increases from 1.5 nH (point A) to 2.42 nH (point B) by maintaining Z_{eq} to 40 Ω. In this approach, both f_L and f_H are lowered, thus reducing the stopband bandwidth. To compensate for this drawback, other approaches can be considered, namely, by moving point A to C. Z_{eq} increases from 40 Ω to 60 Ω and L_{eq} increases from 1.5 nH to 2.42 nH, thus resulting in an f_L value of 1.0 GHz and an f_H value of 4.42 GHz. The f_L reduction is successfully achieved by maintaining f_H to 4.42 GHz. Consequently, the suppression region of the parallel plate noise is broadened as is f_L is reduced. As it has been observed in the proposed analysis, the contour plots, which were extracted with the use of the closed-form expressions for f_L and f_H, provided a simple and systematic approach to design the DP–EBG structure in thin and cost-effective PCBs.

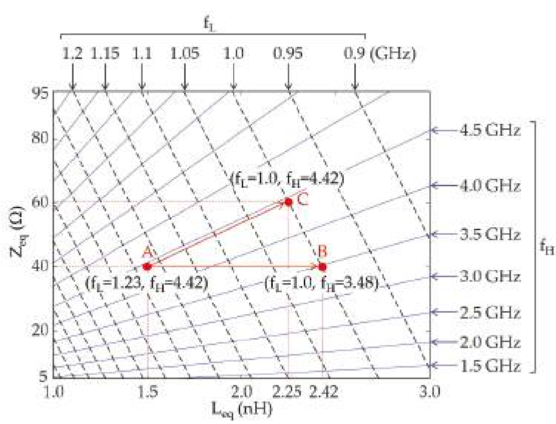

Figure 5. Contour plots of f_L and f_H used for the design and analyses of DP–EBG structures.

2.4. Performance Comparisons

The performances of the proposed DP–EBG structure are demonstrated by comparing their dispersion characteristics with those of previous EBG structures, namely a mushroom-type EBG (MT–EBG), defected-ground EBG (DGS–EBG), and inductance-enhanced EBG (IEP–EBG) structures. The unit cells and the dimensions of these EBG structures are shown in Figure 6 and Table 1, respectively. It is noted that the unit cells of these EBG structures have the same size. The dispersion characteristics are obtained by applying the Floquet theory to full-wave simulation results [25]. The results are illustrated in Figure 7. The f_L values of the previously proposed MT–EBG, DGS–EBG, IEP–EBG, and the proposed DP–EBG structures are 4.95, 2.28, 1.22, and 1.00 GHz, respectively. For the same unit cell size, the proposed DP–EBG structure shows the lowest f_L in the EBG structures. Moreover, the proposed DP–EBG structure substantially reduces f_L compared to the MT– and DGS–EBG structures. Even though the stopband bandwidth of the MT– and DGS–EBG structures are larger than the DP–EBG structure, the stopbands of the MT– and DGS–EBG structures are in higher frequency ranges. These ranges cannot be lowered unless their unit cell sizes are significantly enlarged. The IEP–EBG structure has a low f_L value comparable to the DP–EBG structure. However, the stopband bandwidth of the IEP–EBG structure is 0.48 GHz, which is equal to at most 0.17 times the stopband bandwidth of the DP–EBG structure. The DP–EBG structure successfully overcomes the limitation of the IEP–EBG structure, thus widening the bandwidth of the stopband.

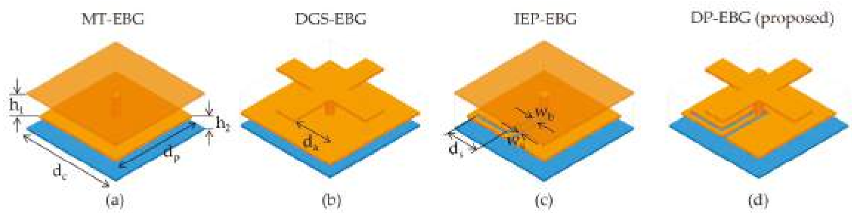

Figure 6. Unit cells of (**a**) mushroom-type (MT)–, (**b**) defected ground structure (DGS)–, (**c**) inductance-enhanced patch (IEP)–, and (**d**) DP–EBG structures for stopband comparisons.

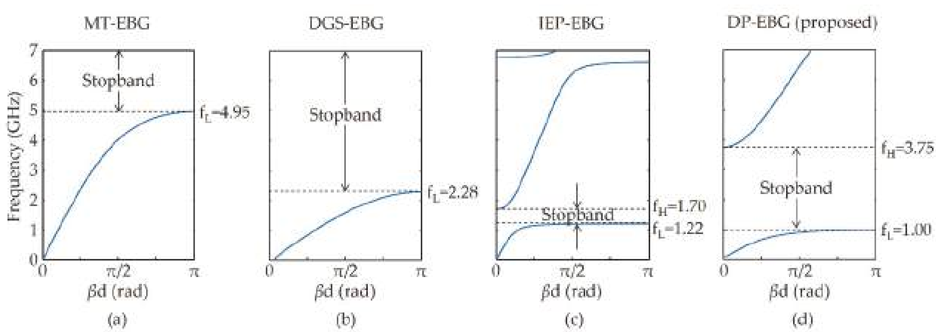

Figure 7. Dispersion diagrams of (**a**) MT–, (**b**) DGS–, (**c**) IEP–, and (**d**) DP–EBG structures.

To examine the advantage of miniaturization, an FEM-based dispersion analysis is performed to compare the previous MT–EBG and the proposed DP–EBG structures. The unit cell areas are found when the MT–EBG and DP–EBG structures contain the same f_L. The comparison result is depicted in Figure 8. An amount of unit cell area reduction substantially increases as the f_L is lowered. For an f_L value equal to 1.0 GHz, the area reduction of the DP–EBG structure is 94.2% compared to the MT–EBG structure. It is shown that the DP–EBG structure is advantageous because it downsizes the unit cell. Remarkably, this enhancement is achieved in dual-plane perforation cases only, without requiring costly materials and additional PCB processes.

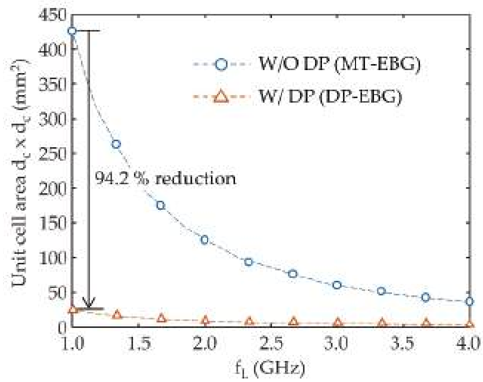

Figure 8. Comparison of unit-cell miniaturization between previous MT– and proposed DP–EBG structures.

3. Results

In this section, the parallel-plate noise suppression of the DP–EBG structure in thin PCBs is demonstrated based on the scattering parameters (S-parameters) which are obtained from the full-wave simulation of the DP–EBG structure with a 7×7 array. Moreover, it is experimentally verified that the DP–EBG structure suppresses parallel-plate noise in thin PCBs using a test vehicle fabricated with conventional PCB process.

3.1. Simulated Results

A full-wave simulation model of the DP–EBG structure with a 7×7 array is depicted in Figure 9. The array size is determined to implement the quasiperiodic condition of the DP–EBG structure. Two-port simulation is performed with waveguide ports renormalized to 50 Ω. The boundaries are set to perfect magnetic conductors and a perfect matched layer, as shown in Figure 9. To compare the noise suppression performance, the simulated S-parameters of the previous EBG structures with the 7×7 array and the parallel plate waveguide (PPW) without any EBG structure are also obtained. The dimensions of the geometrical parameters were described in the previous section. The port locations and the boundary conditions are identical for all EBG structures and the PPW.

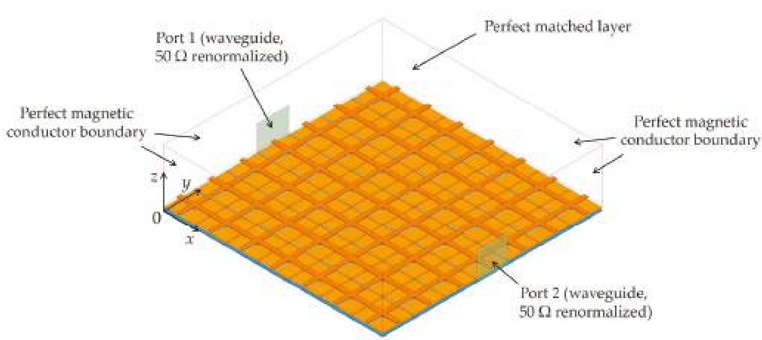

Figure 9. Finite difference method (FEM)-based simulation model of the DP–EBG structure with a 7×7 array.

To prove the existence of a wideband stopband with a low f_L, the simulated S_{21} parameters of the PPW, IEP–EBG, and DP–EBG structures, are shown in Figure 10a. As it can be observed, the PPW without any EBG structure is vulnerable to parallel plate noise. The stopband with a −40 dB suppression level of the IEP–EBG structure forms in the frequency range from 1.01 GHz to 1.36 GHz, while that of the DP–EBG structure ranges from 0.98 GHz to 3.32 GHz. For the same size of the EBG structures, the stopband bandwidth of the DP–EBG structure is approximately 6.7 times wider than that of the IEP–EBG structure. Moreover, the stopband of the proposed DP–EBG structure is significantly lowered compared to those of the MT–EBG and DGS–EBG structures, as shown in Figure 10b. The f_L values of the MT–EBG, DGS–EBG, and DP–EBG structures are 4.6, 3.33, and 0.98 GHz, respectively. The DP–EBG structure substantially reduces the f_L value up to 78.7% without adding costly materials and processes. The stopband estimation based on the S-parameter exhibits a good correlation with dispersion analysis results. The f_L and f_H predicted from the dispersion analysis are 1.0 and 3.75 GHz, respectively.

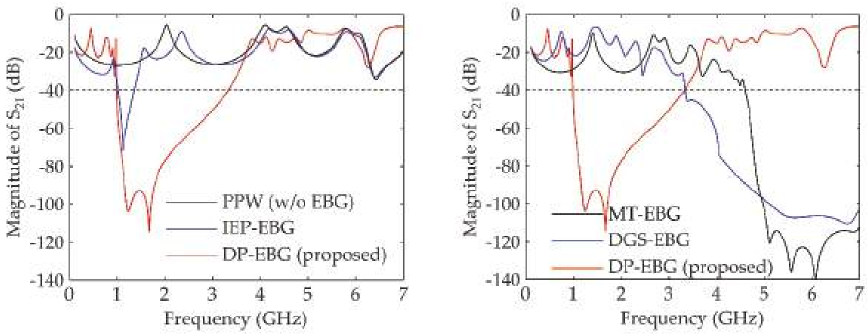

(**a**) (**b**)

Figure 10. Comparison of S-parameters between (**a**) the ppw, IEP-EBG and proposed EBG structures and (**b**) MT-EBG, DGS-EBG, and proposed EBG structures to demonstrate a broad stopband bandwidth and miniaturization.

3.2. Measurements

To experimentally verify the DP–EBG structure, a test vehicle is fabricated using conventional PCB process. The process provides a copper-based conduction layer, FR–4 dielectric, through-hole via, and a minimum dielectric thickness of 100 µm. The via diameter is 0.4 mm and the copper thickness is 17 µm. The dielectric constant and loss tangent of the FR–4 are 4.4 and 0.02, respectively. The dimensions for the test vehicle of the DP–EBG structure are listed in Table 1. The test vehicle includes a 7×7 array and the entire board size is 35 mm x 35 mm. The measurement setup and fabricated PCBs of the DP–EBG structure are depicted in Figure 11. To obtain the S-parameters of the DP–EBG structure, a vector network analyzer (Anritsu MS46122A, 1 MHZ to 1 GHz) and microprobes (GSG type, 500 µm pitch) are employed. The probing pads on the test vehicle are located at (0 mm, 17.5 mm) and (35 mm, 17.5 mm) with the origin placed at the lower left corner of the PCBs. This setup is the same as the setup of the full-wave simulation described in the previous section. The measured and simulated S_{21} parameters are shown in Figure 12. The stopband of the DP–EBG structure is clearly observed in the measurement. The f_L and f_H values with a −40 dB suppression level are equal to 1.03 and 3.32 GHz, respectively. The measurements show good agreement with the full-wave simulation result. Consequently, it is experimentally verified that the DP–EBG structure substantially suppresses the parallel-plate noise with the advantage of miniaturization (in other words, low f_L) in thin and low-cost PCBs.

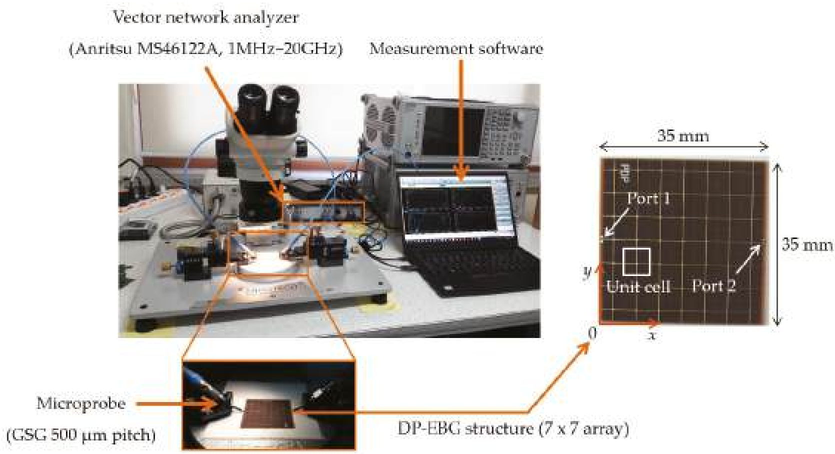

Figure 11. Measurement setup for DP–EBG structure with a 7 × 7 array.

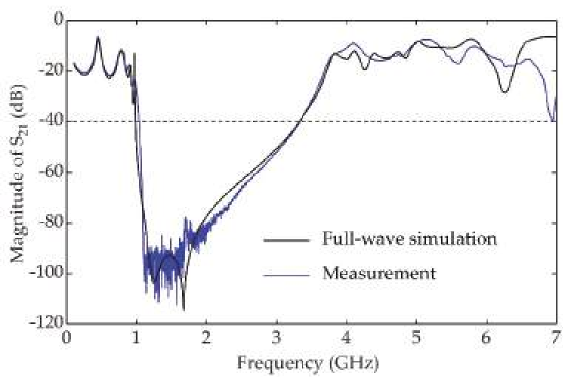

Figure 12. Measured and simulated S_{21} parameters of the DP–EBG structure.

4. Conclusions

The DP–EBG structure was proposed to improve parallel-plate noise suppression and downsize the EBG structure in multilayer PCBs with thin dielectrics. The proposed DP technique efficiently overcame the limitations of the previous EBG structure in thin and low-cost PCBs. The perforation pattern for a resonant patch lowered the start frequency of the stopband and the plane perforation improved the stopband bandwidth. The DP technique successfully achieved these without any costly materials and processes. The improved characteristics of the DP–EBG structures were thoroughly examined and validated using dispersion analysis, full-wave simulations, and experiments. In this study, the particular patterns of the rectangular aperture and L-shape slot for the DP technique are presented. Additional research studies on other patterns for the DP technique need to be conducted. It is thus anticipated that a synthesis algorithm will be developed for the various patterns planned to be tested using the DP technique.

Author Contributions: The author conceived and designed the experiments, analyzed the characteristics, performed the simulations and experiments, and wrote the paper.

Funding: This work was supported by the National Research Foundation of Korea (NRF) grant funded by the Korea government (Ministry of Science and ICT) (NRF-2019R1C1C1005777).

Conflicts of Interest: The author declares no conflict of interest.

Abbreviations

DGS	defected ground structure
DP	dual perforation
EBG	electromagnetic bandgap
FEM	finite difference method
IEP	inductance-enhanced patch
MT	mushroom-type
PCB	printed circuit board
PPW	parallel plate waveguide

References

1. Novak, I. Lossy power distribution networks with thin dielectric layers and/or thin conductive layers. *IEEE Trans. Adv. Packag.* **2000**, *23*, 353–360. [CrossRef]
2. Senthinathan, R.; Prince, J.L. Simultaneous switching ground noise calculation for packaged CMOS devices. *IEEE J. Solid-State Circuits* **1991**, *26*, 1724–1728. [CrossRef]
3. McCredie, B.D.; Becker, W.D. Modeling, measurement, and simulation of simultaneous switching noise. *IEEE Trans. Compon. Packag. Manuf. Technol. Part B* **1996**, *19*, 461–472. [CrossRef]
4. Chun, S.; Swaminathan, M.; Smith, L.D.; Srinivasan, J.; Jin, Z.; Iyer, M.K. Modeling of simultaneous switching noise in high speed systems. *IEEE Trans. Adv. Packag.* **2001**, *24*, 132–142. [CrossRef]
5. Tang, K.T.; Friedman, E.G. Simultaneous switching noise in on-chip CMOS power distribution networks. *IEEE Trans. Very Larg. Scale Integr. Syst.* **2002**, *10*, 487–493. [CrossRef]
6. Swaminathan, M.; Chung, D.; Grivet-Talocia, S.; Bharath, K.; Laddha, V.; Xie, J. Designing and Modeling for Power Integrity. *IEEE Trans. Electromagn. Compat.* **2010**, *52*, 288–310. [CrossRef]
7. Kamgaing, T.; Ramahi, O.M. A novel power plane with integrated simultaneous switching noise mitigation capability using high impedance surface. *IEEE Microw. Wirel. Compon. Lett.* **2003**, *13*, 21–23. [CrossRef]
8. Abhari, R.; Eleftheriades, G.V. Metallo-dielectric electromagnetic bandgap structures for suppression and isolation of the parallel-plate noise in high-speed circuits. *IEEE Trans. Microw. Theory Tech.* **2003**, *51*, 1629–1639. [CrossRef]
9. Lee, J.; Kim, H.; Kim, J. High dielectric constant thin film EBG power/ground network for broad-band suppression of SSN and radiated emissions. *IEEE Microw. Wirel. Compon. Lett.* **2005**, *15*, 505–507.
10. Park, J.; Lu, A.C.W.; Chua, K.M.; Wai, L.L.; Lee, J.; Kim, J. Double-stacked EBG structure for wideband suppression of simultaneous switching noise in LTCC-based SiP applications. *IEEE Microw. Wirel. Compon. Lett.* **2006**, *16*, 481–483. [CrossRef]
11. Wang, C.D.; Yu, Y.M.; de Paulis, F.; Scogna, A.C.; Orlandi, A.; Chiou, Y.P.; Wu, T.L. Bandwidth Enhancement Based on Optimized Via Location for Multiple Vias EBG Power/Ground Planes. *IEEE Trans. Compon. Packag. Manuf. Technol.* **2012**, *2*, 332–341. [CrossRef]
12. Rajo-Iglesias, E.; Inclan-Sanchez, L.; Vazquez-Roy, J.; Garcia-Munoz, E. Size Reduction of Mushroom-Type EBG Surfaces by Using Edge-Located Vias. *IEEE Microw. Wirel. Compon. Lett.* **2007**, *17*, 670–672. [CrossRef]
13. Awasthi, S.; Biswas, A. Compact filter using coupled metamaterial mushroom resonators with corner vias. In Proceedings of the 2011 IEEE Applied Electromagnetics Conference (AEMC), Kolkata, India, 18–20 December 2011; pp. 1–4.
14. Kamgaing, T.; Ramahi, O.M. Multiband Electromagnetic-Bandgap Structures for Applications in Small Form-Factor Multichip Module Packages. *IEEE Trans. Microw. Theory Tech.* **2008**, *56*, 2293–2300. [CrossRef]
15. Kasahara, Y.; Toyao, H. Compact (lambda/45-Sized) Electromagnetic Bandgap Structures With Stacked Open-Circuit Lines. *IEEE Microw. Wirel. Compon. Lett.* **2017**, *27*, 694–696. [CrossRef]
16. Kasahara, Y.; Toyao, H.; Hankui, E. Compact and Multiband Electromagnetic Bandgap Structures with Adjustable Bandgaps Derived From Branched Open-Circuit Lines. *IEEE Trans. Microw. Theory Tech.* **2017**, *65*, 2330–2340. [CrossRef]
17. Shen, C.; Chen, S.; Wu, T. Compact Cascaded-Spiral-Patch EBG Structure for Broadband SSN Mitigation in WLAN Applications. *IEEE Trans. Microw. Theory Tech.* **2016**, *64*, 2740–2748. [CrossRef]
18. Kim, M. A Miniaturized Electromagnetic Bandgap Structure Using an Inductance-Enhanced Patch for Suppression of Parallel Plate Modes in Packages and PCBs. *Electronics* **2018**, *7*, 76. [CrossRef]

19. Zhang, M.; Li, Y.; Jia, C.; Li, L. A Power Plane with Wideband SSN Suppression Using a Multi-Via Electromagnetic Bandgap Structure. *IEEE Microw. Wirel. Compon. Lett.* **2007**, *17*, 307–309. [CrossRef]
20. Park, H.H. Reduction of Electromagnetic Noise Coupling to Antennas in Metal-Framed Smartphones Using Ferrite Sheets and Multi-Via EBG Structures. *IEEE Trans. Electromagn. Compat.* **2018**, *60*, 394–401. [CrossRef]
21. Han, Y.; Huynh, H.A.; Kim, S. Pinwheel Meander-Perforated Plane Structure for Mitigating Power/Ground Noise in System-in-Package. *IEEE Trans. Compon. Packag. Manuf. Technol.* **2018**, *8*, 562–569. [CrossRef]
22. Kim, M.; Koo, K.; Hwang, C.; Shim, Y.; Kim, J.; Kim, J. A Compact and Wideband Electromagnetic Bandgap Structure Using a Defected Ground Structure for Power/Ground Noise Suppression in Multilayer Packages and PCBs. *IEEE Trans. Electromagn. Compat.* **2012**, *54*, 689–695.
23. Kim, M.; Kam, D.G. A Wideband and Compact EBG Structure with a Circular Defected Ground Structure. *IEEE Trans. Compon. Packag. Manuf. Technol.* **2014**, *4*, 496–503. [CrossRef]
24. Kim, Y.; Cho, J.; Cho, K.; Park, J.; Kim, S.; Kim, D.H.; Park, G.; Sitaraman, S.; Raj, P.M.; Tummala, R.R.; et al. Glass-Interposer Electromagnetic Bandgap Structure with Defected Ground Plane for Broadband Suppression of Power/Ground Noise Coupling. *IEEE Trans. Compon. Packag. Manuf. Technol.* **2017**, *7*, 1493–1505. [CrossRef]
25. Collin, R.E. *Field Theory of Guided Waves*; IEEE Press: New York, NY, USA, 1990.

electronics

MDPI

Article

Shielding Properties of Cement Composites Filled with Commercial Biochar

Muhammad Yasir [1], Davide di Summa [2], Giuseppe Ruscica [2], Isabella Natali Sora [2] and Patrizia Savi [1,*]

1 Department of Electronics and Telecommunications, Polytechnic of Turin, C.so Duca degli Abruzzi 24, 10129 Torino, Italy; muhammad.yasir@polito.it
2 Department of Engineering and Applied Sciences, University of Bergamo, 24044 Dalmine, Italy; davide.disumma@unibg.it (D.d.S.); giuseppe.ruscica@unibg.it (G.R.); isabella.natali-sora@unibg.it (I.N.S.)
* Correspondence: patrizia.savi@polito.it

Received: 11 May 2020; Accepted: 14 May 2020; Published: 16 May 2020

Abstract: The partial substitution of non-renewable materials in cementitious composites with eco-friendly materials is promising not only in terms of cost reduction, but also in improving the composites' shielding properties. The water and carbon content of a commercial lignin-based biochar is analyzed with thermal gravimetric analysis. Cementitious composite samples of lignin-based biochar with 14 wt.% and 18 wt.% are realized. Good dispersion of the filler in the composites is observed by SEM analysis. The samples are fabricated in order to fit in a rectangular waveguide for measurements of the shielding effectiveness in the X-band. A shielding effectiveness of 15 dB was obtained at a frequency of 10 GHz in the case of composites with 18 wt.% biochar. Full-wave simulations are performed by fitting the measured shielding effectiveness to the simulated shielding effectiveness by varying material properties in the simulator. Analysis of the dimensional tolerances and thickness of the samples is performed with the help of full/wave simulations. Lignin-based biochar is a good candidate for partial substitution of cement in cementitious composites, as the shielding effectiveness of the composites increases substantially.

Keywords: shielding effectiveness; biochar; eco-friendly material; cementitious composites; waveguides

1. Introduction

The human population saw rapid growth in the past few decades. With increasing population, the demand for the construction industry increased manifold [1]. This resulted in increasing greenhouse gas emissions from cement production [2]. The substitution of non-renewable raw materials used in the construction industry with eco-friendly materials derived from waste is promising in terms of cost and environmental protection [3]. Agriculture and forestry waste is primarily burnt on field in order to reduce the cost of disposal. When converted into biochar, this waste can be used as a partial substitute to cement, resulting in a significant reduction in greenhouse gas emissions and improving the mechanical properties of concrete [4,5].

An increasing number of devices working at microwave- and millimeter-wave frequencies resulted in an overall increase in electromagnetic radiation [6,7]. Electromagnetic shields are deployed to protect sensitive devices against electromagnetic interference [8,9]. In places that are vulnerable to electromagnetic interference, shielding materials can be applied as a coating on wall surfaces [10]. A number of devices working at microwave- and millimeter-wave frequencies are used in the health sector for applications like imaging, tomography, etc. [11,12]. The X-band in particular is important for radar communications including air-traffic control, weather monitoring, maritime vessel traffic control, defense tracking, and vehicle speed detection. The use of shielding materials in buildings can be helpful in isolating equipment that is sensitive to electromagnetic interferences [13,14]. Different measurement techniques can be deployed for the determination of the shielding effectiveness of materials. The most common measurement techniques are: reverberation chamber [15], free-space measurements in an anechoic chamber [16], and coaxial and waveguide methods [17–19]. Each measurement technique requires specific sample dimensions and frequency band. The X-band is very important for applications like satellite communications and radar.

The use of carbon-based materials in epoxy composites and the analysis of their morphological and electrical properties were vastly studied [20–23]. Conventional carbon-based materials like graphene and carbon nanotubes are expensive and require complex synthesis. In recent years, the use of biochar-substituted carbon nanotubes and graphene in composites as filler was investigated [24,25]. Biochar is cost-effective as compared to other carbon-based materials. Biochar is a porous carbonaceous material produced by thermal treatment of biomass in the absence of oxygen [26]. It can be made from a number of different waste products such as agricultural waste, food waste, or sewage sludge [27]. Until recently, biochar was used for soil amendment in agriculture and landfilling applications [28]. The use of biochar in alternative applications is being studied at a vast scale, specifically for carbon sequestration, for energy storage applications [29], and in construction and building [30,31].

In this paper, lignin-based commercial biochar was used as a partial substitute to cement in composites. The water, carbon, and other residues of the biochar were studied by thermogravimetric analysis (TGA). Composites of 4 mm thickness with plain cement, 14 wt.% biochar, and 18 wt.% biochar were fabricated with specific dimensions for measurements of the shielding effectiveness inside a waveguide working in the X-band microwave frequency. The samples with 18 wt.% biochar were cured in water for seven days or 28 days. For examining the microstructural properties of the composites and dispersion of the filler in the composite matrix, SEM was adopted. Measurements of the shielding effectiveness were compared with simulated results obtained with a full-wave simulator. As expected, the shielding effectiveness increased with the increase of the percentage of filler (11 dB for 14 wt.%, and 15 dB for 18 wt.% at 10 GHz). Analyses of fabrication tolerances and sample thickness were performed with the help of a full-wave simulator.

Finally, the effect of the curing period in water on the shielding effectiveness values was analyzed for the samples with 18 wt.% biochar. The shielding effectiveness increased by approximately 5 dB in the whole frequency range for the sample cured in water for 28 days with respect to the sample cured in water for seven days.

2. Materials and Methods

2.1. Composites Preparation

The composite samples produced were with 14 wt.% and 18 wt.% biochar in Portland cement (PC). For the sake of comparison, a composite without biochar was also produced, which is referred to as plain cement composite. The biochar used to realize the samples was a commercial product provided by Carlo Erba Reagents. It was pyrolyzed in the form of powder at a temperature of 750 °C for four hours in an alumina crucible. For preparation of cementitious composites, ordinary Portland Cement (PC) (grade 52.5 R) compliant with ASTM C150 was used along with water and superplasticizer to form an adequate consistency of the paste. The percentages of water and superplasticizer used were equal to 60 wt.% and 1.8 wt.%, respectively. A mechanical mixer was used to work the mixture for a duration of 5 min. Silicon molds of adequate shape and size were then used to give the composites the required shape and dimensions.

Portland cement was blended with biochar by using a mechanical mixer for 5 min with two different percentages by weight of cement, 14% and 18%, water (60%), and superplasticizer (1.8%). Furthermore, a reference specimen was realized using only Portland cement matrix blended together with water and superplasticizer equal to 35% and 1.5%. The obtained composites were then poured into rectangular silicone molds for shielding effectiveness analysis. The silicon molds were fabricated in a three-dimensional (3D) printed master mold of specific dimensions (see Figure 1). The reusable and flexible silicone molds helped with easy extraction of composite samples once they were cured.

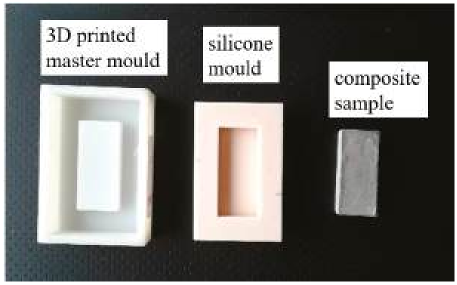

Figure 1. Three-dimensional (3D) printed master mold with silicone mold and an example of a composite sample.

Initially, the composite samples were kept at a relative humidity of 90% ± 5% for 24 h. The composites were then demolded and immersed in water at a temperature of 20 ± 2 °C. The samples were then cured in water for a period of seven days. Two different curing methodologies were used for curing of the 18 wt.% samples in water for seven days and 28 days, in order to evaluate the impact of water curing duration on the shielding effectiveness (see Table 1). In Table 1, the different steps of fabrication and measurements of the cement composites are reported.

Table 1. Fabrication and measurements of the cement composites.

Day	Plain Cement	14 wt.% (7 days)	18 wt.% (7 days)	18 wt.% (28 days)
0	Fabrication	Fabrication	Fabrication	Fabrication
1	Demolded	Demolded	Demolded	Demolded
1	Cured in water	Cured in water	Cured in water	Cured in water
7	Extracted from water	Extracted from water	Extracted from water	-
21	SE meas.* 2 weeks	SE meas.* 2 weeks	SE meas.* 2 weeks	-
28	-	-	-	Extracted from water
42	-	-	-	SE meas.* 2 weeks
70	SE meas.* 10 weeks	SE meas.* 10 weeks	SE meas.* 10 weeks	-
98	-	-	-	SE meas.* 10 weeks

* Shielding effectiveness measurement (SE meas.)

2.2. Morphological Analysis

Thermogravimetric analyses (TG-DTA) were carried out in air using about 20 mg of biochar heated from room temperature to 950 °C at 3 °C/min. For a morphological characterization of the cement composites, a scanning electron microscope (Hitachi S-2500C, Hitachi, Japan) was used for the analysis of the cross-section of cement composites with 18 wt.% biochar. Sections of the composite were cut and polished with measurements performed on gold-plated samples to avoid any charging effects.

2.3. Radiofrequency Measurements

The total shielding effectiveness can be defined as the ratio of the incident and transmitted field. It can be obtained from the measured transmission loss (S_{21}) in a waveguide as follows:

$$SE = -20 \cdot log(|S_{21}|). \tag{1}$$

The total shielding effectiveness of a material comprises dissipation loss, L_D, and mismatch loss, L_M [32].

$$SE = L_D + L_M, \tag{2}$$

where L_M can be calculated from the reflection scattering parameter as follows:

$$L_M = -10 \cdot log_{10}\left(1 - |S_{11}|^2\right), \tag{3}$$

$$L_D = -10 \cdot log_{10}\left(\frac{|S_{21}|^2}{1 - |S_{11}|^2}\right). \tag{4}$$

The scattering parameters of the composites were measured in a WR90 (Sivers IMA, Holding AB (HQ), Sweden) rectangular waveguide from 8 GHz to 12 GHz using a set-up similar to that in Reference [33]. The samples were fabricated in order to fit the rectangular waveguide cross-section (a = 22.86 mm, b = 10.16 mm). The thickness of the samples was 4 mm. The set-up is shown in Figure 2. It consisted of a two-port vector network analyzer (VNA) (Agilent E8361A: Keysight, Santa Rosa, CA 81841, USA), two coaxial cables connected to the two ports of the network analyzer, two coaxial-to-waveguide adapters, and two rectangular waveguides. Between the waveguide flanges, a spacer holding the sample was inserted. Before the measurements, a two-port calibration (short, matched load, thru) was performed. The reference planes were at the ends of the spacer.

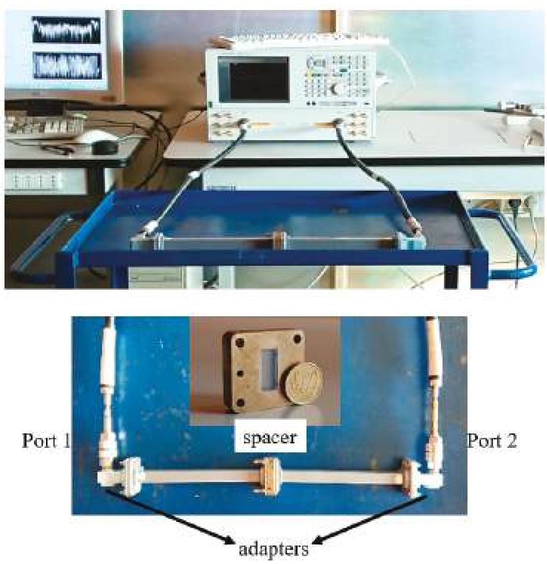

Figure 2. WR90 waveguide measurement set-up.

2.4. Finite Element Simulations

A commercial finite element modeling tool, Ansys HFSS, was used to simulate the waveguide with the composite sample as shown in Figure 3. The material properties of the composite inserted in the waveguide were chosen by fitting the simulated shielding effectiveness values to the measured shielding effectiveness values. The composite dimensions and thickness were varied to analyze the impact of fabrication tolerances and thickness on the values of shielding effectiveness.

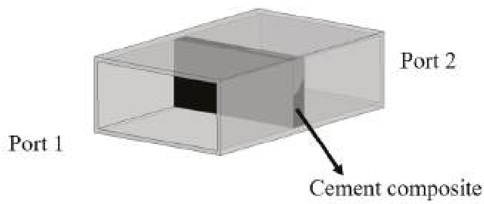

(**a**)

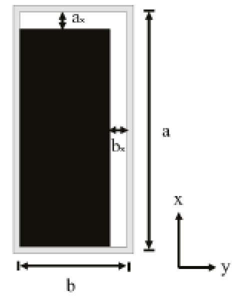

(**b**)

Figure 3. Geometrical configuration of the waveguide: (**a**) geometry of the simulated waveguide with composite. (**b**) Cross-section of the waveguide for the dimensional analysis.

2.5. Dimensional Tolerance Analysis

In order to take into account the dimensional tolerance of the cement composite, simulations were performed based on varying the two dimensions along the *x*-axis and *y*-axis (see Figure 3). In the case of plain cement composites, it was found that there was negligible variation of the transmission properties by varying the a_x dimension of the sample, while the impact of the variation of b_x was significant. A variation of 0.5 mm in b_x resulted in a variation of almost 1 dB in the transmission coefficient, as shown in Figure 4. It was ensured that the tolerance in the dimensions of the cement composites was below this value.

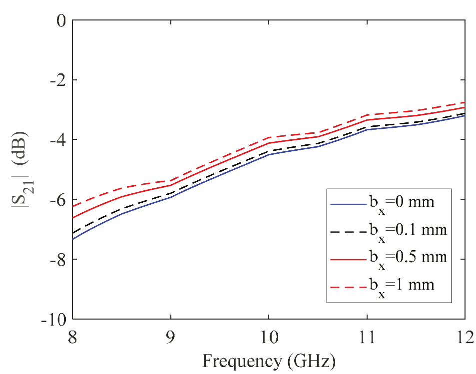

Figure 4. Analysis of fabrication tolerances of the plain cement composites.

3. Results

3.1. Biochar and Composite Characterization

The water and carbon content of the biochar was investigated by TG-DTA experiments. The TGA curve of biochar is reported in Figure 5. Below 100 °C, the weight loss was about 16%, due to the evaporation of the physically adsorbed water. From 350 °C to 500 °C, the weight loss was due to the combustion of the graphitic carbon fraction (about 74% of the total weight of the sample). At 950 °C, a residue of around 5% in weight was observed with respect to the initial amount.

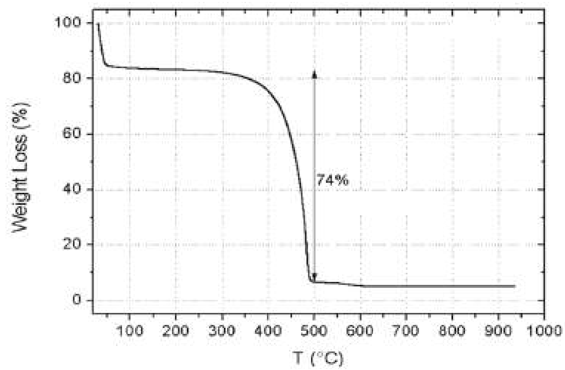

Figure 5. Thermogravimetric analysis (TGA) curve of biochar filler.

Figure 6 illustrates the SEM image of composites with the highest content of biochar (18 wt.%) recorded with secondary electrons. The black structures shown in the SEM image are the carbonaceous particles. The expected elongated structure of the particles was due to the fiber origin of the biochar. The particles showed a good dispersion in the matrix.

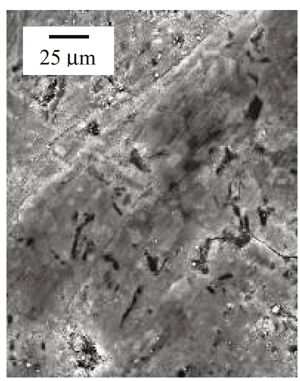

Figure 6. SEM micrograph of cement containing biochar 18% at 1000× magnification.

3.2. *Shielding Effectiveness Analysis*

Shielding effectiveness can be found from the measured transmission coefficient, S_{21}, in a waveguide (see Figure 2), as defined in Equation (1). The measured shielding effectiveness values of the plain cement used as a reference sample, as well as the sample with 14 wt.% and 18 wt.% filler cured in water for seven days, measured after 10 weeks, are shown in Figure 7. At the center frequency of 10 GHz, the shielding effectiveness of plain cement was almost 5 dB, which increased to 11 dB for the samples with 14 wt.% biochar. The maximum shielding effectiveness measured for the sample with 18 wt.% was around 15 dB. These results were obtained with 4-mm-thick samples. The shielding effectiveness values could be further increased by increasing the sample thickness and/or the percentage of biochar. The shielding effectiveness of the plain cement composites decreased with frequency. This behavior is similar to other cement composites [34]. The different behavior in terms of the frequency of the biochar composites with respect to plain cement composites can be attributed to the presence of entrapped water in the biochar [35].

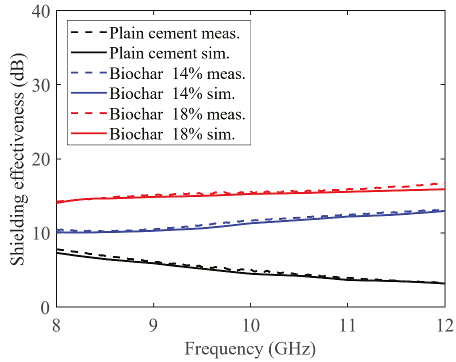

Figure 7. Measured and simulated shielding effectiveness values for plain cement, as well as the sample with 14 wt.% biochar and the sample with 18 wt.%. Samples were cured for seven days in water. Measurements were performed after 10 weeks of aging.

In Figure 7, the simulated shielding effectiveness obtained with full-wave simulations are reported (dashed lines). The values of complex permittivity were varied to fit the simulated shielding effectiveness values to the measured shielding effectiveness values, and a good correlation between the measured and simulated data was obtained.

There is a strong correlation between the curing period in water and the mechanical strength of cement composites [30]. In order to evaluate the effect of the curing period in water on the shielding effectiveness values, samples with 18 wt.% biochar cured in water for a period of seven days and 28 days were analyzed. The shielding effectiveness of the cement composite with 18 wt.% biochar cured in water for seven days and 28 days, measured after two weeks and 10 weeks, are shown in Figure 8. It can be seen that the sample cured in water for 28 days had higher shielding effectiveness when measured both after two weeks and after 10 weeks. The variation of the shielding effectiveness over time of the cement composite cured for 28 days was also higher than that cured in water for seven days. This shows that the shielding effectiveness increased due to the presence of water, whereby the loss of water from the sample over time resulted in a reduced value of the shielding effectiveness.

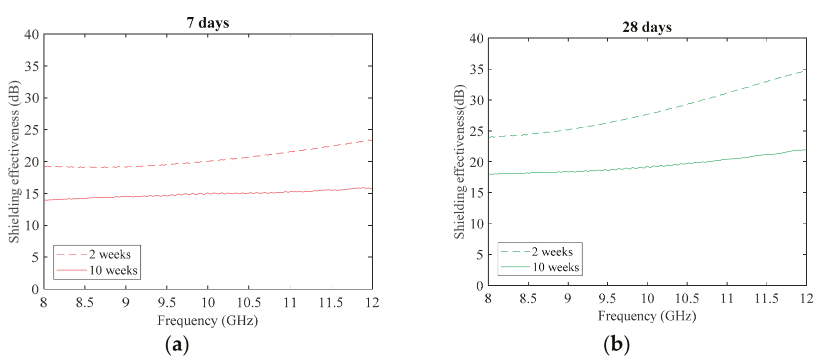

Figure 8. Measured shielding effectiveness of cement sample with 18 wt.% biochar: (**a**) cured in water for seven days; (**b**) cured in water for 28 days. Measurements were performed after two weeks and 10 weeks.

4. Discussions

In order to evaluate the impact of the presence of biochar in the cement composites on the shielding effectiveness, a comparison was performed with other studies in the literature (see Table 2).

The case considered in this comparison was the composite filled with 18 wt.% biochar cured in water for seven days and measured after 10 weeks. The thickness of the samples considered was 4 mm, which provided a shielding effectiveness value of almost 14 dB. In comparison with the literature, other reported cement samples gave higher shielding effectiveness values due to a higher value of thickness. In order to evaluate the impact of the thickness on the shielding effectiveness, simulations were performed with higher thickness values. The results are shown in Figure 9. As expected, the shielding effectiveness increased considerably upon increasing the thickness of the sample.

Table 2. Comparison with the literature.

Reference	Frequency	Measured After (days)	Thickness (mm)	Shielding Effectiveness (dB)	Materials
[34]	3 GHz	36	100	17.5	Cement
[36]	10 GHz	95	150	20	Cement
This work	10 GHz	70	4	15	Cement + 18 wt.% biochar

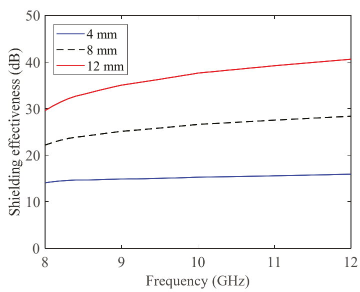

Figure 9. Simulated results for cement composites with 18 wt.% biochar with different thicknesses.

5. Conclusions

Biochar is obtained by thermal treatment of waste products. It is vastly used for soil amendment. More recently, it was used for applications such as energy storage, carbon sequestration, and construction. The effect of a commercial biochar on the shielding properties of cement composites was investigated in the X-band. The conclusions drawn based on the results presented can be extended to other microwave frequencies. Cementitious composites with ordinary Portland Cement (PC) were prepared without biochar and with biochar as filler (14 wt.% and 18 wt.%). Samples were prepared in order to fit a WR90 waveguide (8–12 GHz). With the help of a full-wave simulator, the fabrication tolerances of the samples were analyzed. A variation of ±0.5 mm resulted in a change of the shielding effectiveness of ±1 dB. Shielding effectiveness can be obtained from the measurements of scattering parameters. Samples with 14 wt.% and 18 wt.% biochar as filler were cured in water for seven days. As expected, the shielding effectiveness increased with the increase in the percentage of filler (11 dB for 14 wt.%, and 15 dB for 18 wt.% at 10 GHz). In order to evaluate the effect of the curing period in water on the shielding effectiveness, different curing periods were analyzed. Samples with 18 wt.% biochar were cured in water for a period of seven days and 28 days. The shielding effectiveness increased by approximately 5 dB in the whole frequency range for the samples cured in water for 28 days as compared to samples cured in water for seven days.

Author Contributions: Composite fabrication, D.d.S. and G.R.; waveguide measurements and discussion of the shielding effectiveness, D.d.S., M.Y., and P.S.; microstructure characterization and TGA, I.N.S.; full-wave simulations, M.Y.; original draft preparation, M.Y. and P.S.; writing—review and editing, M.Y., P.S., and I.N.S.; supervision, P.S.; conceptualization, M.Y., P.S., and I.N.S., funding acquisition, G.R. All authors read and agreed to the published version of the manuscript.

Funding: This research received no external funding.

Acknowledgments: The authors would like to thank Renato Pelosato for TGA measurements.

Conflicts of Interest: The authors declare no conflict of interest.

References

1. Klee, H. Briefing: The Cement Sustainability Initiative. *Proc. Inst. Civ. Eng.—Eng. Sustain.* **2004**, *157*, 9–11. [CrossRef]
2. Oh, D.-Y.; Noguchi, T.; Kitagaki, R.; Park, W.-J. CO_2 emission reduction by reuse of building material waste in the Japanese cement industry. *Renew. Sust. Energ. Rev.* **2014**, *38*, 796–810. [CrossRef]
3. Balasubramanian, J.; Gopal, E.; Periakaruppan, P. Strength and microstructure of mortar with sand substitutes. *Graevinar* **2016**, *68*, 29–37.
4. Van der Lugt, P.; Van den Dobbelsteen, A.A.J.F.; Janssen, J.J.A. An environmental, economic and practical assessment of bamboo as a building material for supporting structures. *Constr. Build. Mater.* **2006**, *20*, 648–656. [CrossRef]
5. Klapiszewski, Ł.; Klapiszewska, I.; Ślosarczyk, A.; Jesionowski, T. Lignin-Based Hybrid Admixtures and their Role. *Cem. Compos. Fabr. Mol.* **2019**, *24*, 3544.
6. Research and Markets. Available online: https://www.researchandmarkets.com/research/6mzxvg/microwave_devices (accessed on 25 February 2020).
7. Delhi, N.; Behari, G. Electromagnetic pollution-the causes and concerns. In Proceedings of the International Conference of Electromagnetic Interference and Compatibility, Bangalore, India, 23 February 2002.
8. McKerchar, W.D. Electromagnetic Compatibility of High Density Wiring Installations by Design or Retrofit. *IEEE Trans Elm. Comp.* **1965**, *7*, 1–9. [CrossRef]
9. Wang, Y.; Gordon, S.; Baum, T.; Su, Z. Multifunctional Stretchable Conductive Woven Fabric Containing Metal Wire with Durable Structural Stability and Electromagnetic Shielding in the X-Band. *Polymers* **2020**, *12*, 399. [CrossRef]
10. Lee, H.S.; Park, J.H.; Singh, J.K.; Choi, H.J.; Mandal, S.; Jang, J.M.; Yang, H.M. Electromagnetic Shielding Performance of Carbon Black Mixed Concrete with Zn–Al Metal Thermal Spray Coating. *Materials* **2020**, *13*, 895. [CrossRef]
11. Mojtaba, A.; Maryam, I.; Saripan, A.; Iqbal, M.; Hasan, W.Z.W. Three dimensions localization of tumors in confocal microwave imaging for breast cancer detection. *Microw. Opt. Technol. Lett.* **2015**, *57*, 2917–2929.
12. Peng, K.C.; Lin, C.C.; Li, C.F.; Hung, C.Y.; Hsieh, Y.S.; Chen, C.C. Compact X-Band Vector Network Analyzer for Microwave Image Sensing. *IEEE Sens. J.* **2019**, *9*, 3304–3313. [CrossRef]
13. Hanada, E.; Watanabe, Y.; Antoku, Y.; Kenjo, Y.; Nutahara, H.; Nose, Y. Hospital construction materials: Poor shielding capacity with respect to signals transmitted by mobile telephones. *Biomed. Instrum. Technol.* **1998**, *32*, 489–496. [PubMed]
14. Khushnood, R.A.; Ahmad, S.; Savi, P.; Tulliani, J.M.; Giorcelli, M.; Ferro, G.A. Improvement in electromagnetic interference shielding effectiveness of cement composites using carbonaceous nano/micro inerts. *Constr. Build. Mater.* **2015**, *85*, 208–216. [CrossRef]
15. Holloway, C.L.; Hill, D.A.; Ladbury, J.; Koepke, G.; Garzia, R. Shielding effectiveness measurements of materials using nested reverberation chambers. *IEEE Trans. Electromagn. Compat.* **2003**, *45*, 350–356. [CrossRef]
16. Jung, M.; Lee, Y.-S.; Hong, S.-G. Effect of Incident Area Size on Estimation of EMI Shielding Effectiveness for Ultra-High Performance Concrete With Carbon Nanotubes. *IEEE Access* **2019**, *17*, 183106–183117. [CrossRef]
17. Tamburrano, A.; Desideri, D.; Maschio, A.; Sarto, S. Coaxial Waveguide Methods for Shielding Effectiveness Measurement of Planar Materials Up to 18 GHz. *IEEE Trans. Electromagn. Compat.* **2014**, *56*, 1386–1395. [CrossRef]
18. Valente, R.; Ruijter, C.D.; Vlasveld, D.; Zwaag, S.V.D.; Groen, P. Setup for EMI Shielding Effectiveness Tests of Electrically Conductive Polymer Composites at Frequencies up to 3.0 GHz. *IEEE Access* **2017**, *5*, 16665–16675. [CrossRef]
19. Rudd, M.; Baum, T.C.; Ghorbani, K. Determining High-Frequency Conductivity Based on Shielding Effectiveness Measurement Using Rectangular Waveguides. *IEEE Trans. Instrum. Meas.* **2020**, *69*, 155–162. [CrossRef]
20. Gupta, S.; Tai, N.H. Carbon materials and their composites for electromagnetic interference shielding effectiveness in X-band. *Carbon* **2019**, *152*, 159–187. [CrossRef]

21. Giorcelli, M.; Savi, P.; Yasir, M.; Miscuglio, M.; Yahya, M.H.; Tagliaferro, A. Investigation of epoxy resin/multiwalled carbon nanotube nanocomposites behavior at low frequency. *J. Mater. Res.* **2014**, *30*, 101–107. [CrossRef]
22. Savi, P.; Yasir, M.; Giorcelli, M.; Tagliaferro, A. The effect of carbon nanotubes concentration on complex permittivity of nanocomposites. *Prog. Electromagn. Res. M* **2017**, *55*, 203–209. [CrossRef]
23. Khan, A.; Savi, P.; Quaranta, S.; Rovere, M.; Giorcelli, M.; Tagliaferro, A.; Rosso, C.; Jia, C.Q. Low-Cost Carbon Fillers to Improve Mechanical Properties and Conductivity of Epoxy Composites. *Polymers* **2017**, *9*, 642. [CrossRef] [PubMed]
24. Peterson, S.C. Evaluating corn starch and corn stover biochar as renewable filler in carboxylated styrene butadiene rubber composites. *J. Elastomers Plast.* **2011**, *44*, 43–54. [CrossRef]
25. Giorcelli, M.; Savi, P.; Khan, A.; Tagliaferro, A. Analysis of biochar with different pyrolysis temperatures used as filler in epoxy resin composites. *Biomass Bioenergy* **2019**, *122*, 466–471. [CrossRef]
26. Bridgwater, A.V. Review of fast pyrolysis of biomass and product upgrading. *Biomass Bioenergy* **2012**, *38*, 68–94. [CrossRef]
27. Savi, P.; Yasir, M.; Bartoli, M.; Giorcelli, M.; Longo, M. Electrical and Microwave Characterization of Thermal Annealed Sewage Sludge Derived Biochar Composites. *Appl. Sci.* **2020**, *10*, 1334. [CrossRef]
28. Ding, Y.; Liu, Y.; Liu, S.; Li, Z.; Tan, X.; Huang, X.; Zeng, G.; Zhou, L.; Zheng, B. Biochar to improve soil fertility. A review. *Agron. Sustain. Dev.* **2016**, *36*, 36. [CrossRef]
29. Ngan, A.; Jia, C.Q.; Tong, S.-T. Production, Characterization and Alternative Applications of Biochar. In *Production of Materials from Sustainable Biomass Resources*; Springer: Singapore, 2019; pp. 117–151.
30. Gupta, S.; Kua, H.W.; Low, C.Y. Use of biochar as carbon sequestering additive in cement mortar. *Cem. Concr. Compos.* **2018**, *87*, 110–129. [CrossRef]
31. Gupta, S.; Kua, H.W.; Pang, S.D. Effect of biochar on mechanical and permeability properties of concrete exposed to elevated temperature. *Constr. Build. Mater.* **2020**, *234*, 117338. [CrossRef]
32. Savi, P.; Yasir, M. Waveguide measurements of biochar derived from sewage sludge. *Electron. Lett.* **2020**, *56*, 335–337. [CrossRef]
33. Savi, P.; Cirielli, D.; di Summa, D.; Ruscica, G.; Sora, I.N. Analysis of shielding effectiveness of cement composites filled with pyrolyzed biochar. In Proceedings of the 2019 IEEE 5th International forum on Research and Technology for Society and Industry (RTSI), Florence, Italy, 9–12 September 2019; pp. 376–379.
34. Donnell, K.M.; Zoughi, R.; Kurtis, K.E. Demonstration of Microwave Method for Detection of Alkali–Silica Reaction (ASR) Gel in Cement-Based Materials. *Cem. Concr. Res.* **2013**, *44*, 1–7. [CrossRef]
35. Mrad, R.; Chehab, G. Mechanical and Microstructure Properties of Biochar-Based Mortar: An Internal Curing Agent for PCC. *Sustainability* **2019**, *11*, 2491. [CrossRef]
36. Kharkovsky, S.N.; Akay, M.F.; Hasar, U.C.; Atis, C.D. Measurement and monitoring of microwave reflection and transmission properties of cement-based specimens. *IEEE Trans. Instrum. Meas.* **2002**, *51*, 1210–1218. [CrossRef]

electronics

MDPI

Article

Synthesis and Characterization of Polyaniline-Based Composites for Electromagnetic Compatibility of Electronic Devices

Kamil G. Gareev *, Vladislava S. Bagrets, Vladimir A. Golubkov, Maria G. Ivanitsa, Ivan K. Khmelnitskiy, Victor V. Luchinin, Olga N. Mikhailova and Dmitriy O. Testov

Department of Micro and Nanoelectronics, Saint Petersburg Electrotechnical University "LETI", 197376 Saint Petersburg, Russia; bagretsvlada@mail.ru (V.S.B.); vavantess@mail.ru (V.A.G.); marie.ivanitsa@gmail.com (M.G.I.); khmelnitskiy@gmail.com (I.K.K.); cmid_leti@mail.ru (V.V.L.); novaja.tasamaya@yandex.ru (O.N.M.); dtestov@bk.ru (D.O.T.)

* Correspondence: kggareev@etu.ru

Received: 13 April 2020; Accepted: 26 April 2020; Published: 29 April 2020

Abstract: Polyaniline-based composites designed to ensure the electromagnetic compatibility of electronic devices were obtained. The surface morphologies of the obtained films were studied using optical and electron microscopy. The electrical resistivity of polyaniline (PANI) films were measured at various thicknesses. For films of various compositions and various thicknesses, the frequency dependencies of the complex dielectric permittivity, in the range of 100–2000 kHz, as well as the electromagnetic radiation (EMR) absorption coefficient in the frequency range 0.05–2 GHz were obtained. It was found that flexible gelatin-PANI composite films with a thickness of 200–400 μm, a bending radius of about 5 cm, and a real part of complex permittivity of not more than 10 provide an EMR absorption coefficient of up to 5 dB without introducing additional EMR absorbing or reflecting fillers. The resulting gelatin-PANI composite films do not possess a through electrical conductivity and can be applied directly to the surface of protected printed circuit boards.

Keywords: electromagnetic compatibility; polyaniline; gelatin; composite; microwave absorption; dielectric permittivity; electrical conductivity

1. Introduction

Electromagnetic compatibility (EMC) of electronic devices is ensured by applying materials shielding from electromagnetic radiation (EMR) due to EMR absorption and reflection [1]. Ferrite-based composites with organic binders [2] are widely used materials for EMR absorption. Their serious disadvantage is a high mass density, which limits the application of such materials in electronics. The use of composite materials containing conductive polymers and components with high dielectric and magnetic losses can be considered as the most promising way to ensure EMC. Conductive polymer polyaniline (PANI) is used as an additional component with dielectric losses in a wide variety of EMC composites. A high EMR shielding efficiency, in a wide frequency range, has been experimentally proven for composites of PANI using silver nanowires [3], particles of antimony oxide [4], graphene [5–7], carbon nanotubes [8,9], Ti_3SiC_2 [10], MoS_2 [11], CuO [12], bamboo fibers [13], bagasse [14], MXene, and other fillers [15]. The EMR shielding properties of composites of PANI with magnetic nanoparticles of cobalt and iron–nickel alloy [16] and ferrites [17] have also been shown.

PANI was applied as a component of composites for EMC. PANI/polyacrylate composite coatings demonstrated the efficiency of electromagnetic-interference shielding at 38–60 dB in a frequency range of 100 kHz–10 GHz [18]. PANI nanofibers coatings showed an efficiency of electromagnetic-interference shielding of up to 63 dB in that same frequency range [19]. Films of conductive polymeric blends of polystyrene and PANI provided a shielding efficiency of up to 45 dB in a frequency range of 9–18 GHz [20]. PANI provided a low-percolation threshold (0.58 wt.%), high-electrical conductivity, and high-shielding efficiency of composites using carbon nanotubes [21]. Composites based on PANI and MXene possess excellent thermal and EMR shielding efficiency characteristics; thus, they can be applied in for use in mobile phones, military utensils, heat-emitting electronic devices, automobiles, and radars [22]. Even though the conductivity of PANI is not as high as that of metals, it is considerably high when compared to the conductivity of other polymers. Additionally, PANI has many advantages, including ease of fabrication, low cost, and the ability to be switched between electrically conducting and insulating statuses [15].

The efficiency of PANI-containing composites without additional EMR absorbing or reflecting fillers is not widely described in the literature, but these composites may be useful in order to simplify synthesis techniques and to reduce the costs of EMC materials. At the same time, composites of gelatin–PANI, which are potentially useful for various fields, including electronics [23], are only characterized as materials for tissue engineering [24,25], targeted drug delivery [26], and other biomedical applications [27].

The aim of the current work was to obtain PANI films and gelatin–PANI composite films and to study their potential applications for the EMC of electronic devices.

2. Materials and Methods

2.1. Synthesis of PANI Films

In order to obtain a PANI dispersion, a solution containing 0.228 g of $(NH_4)_2S_2O_8$ (Merck, USA) and 1 mL of distilled water was added to a solution containing 0.255 mL of aniline (Merck, USA), 1 mL of 10 M HCl (Merck, USA), and 7 mL of distilled water. The reaction mixture was kept in a water bath at 20 °C for 24 h. The resulting suspension was dark green, typical for the protonated emeraldine form of PANI, which has the highest stability and the lowest resistivity according to the results of other research groups [28]. Then, the suspension was filtered, washed several times with distilled water, refiltered, and dried to obtain a solid PANI, from which a suspension of a given concentration was prepared. PANI films were fabricated with the help of irrigation on polyethylene substrates with a size of 44 × 44 mm, followed by being dried in an oven at 40 °C. The thickness of films ranged from 50 to 200 μm.

2.2. Synthesis of Gelatin–PANI Composites

Obtaining samples of gelatin–PANI composites (for example, 12%-PANI-GEL with 12 mas.% PANI) was carried out as follows: 6.5 g of gelatin P-11 (GOST 11293-89, Vekton, Saint Petersburg, Russia) was added to 50 mL of distilled water in a glass flask. The produced suspension was being stirred using a magnetic stirrer at a temperature of 60 °C for 2 h. An aqueous suspension of polyaniline was prepared in a conical tube by adding a volume of of dry PANI (obtained in accordance with Section 2.1) of 0.28 g to 5.3 mL of distilled water. Further on, the PANI suspension was treated with an ultrasonic homogenizer (Sonopuls HD 4100 (Bandelin, Berlin, Germany)) for 5 min, directly before being mixed with a gelatin solution. The final suspension was poured into a Petri dish for solidification at room temperature.

The samples, 3%-PANI-GEL, 22%-PANI-GEL, 36%-PANI-GEL, 46%-PANI-GEL, 53%-PANI-GEL, and 59%-PANI-GEL with 3, 22, 36, 46, 53, and 59 mas.% PANI, respectively, were obtained in a similar manner. Each synthesis experiment was repeated five times. The maximum content of PANI was due to the need to obtain a stable suspension for sample preparation.

To provide electrophysical measurements, a sample with a size of 44 × 44 mm and a thickness of 200–400 μm was cut out of the obtained flexible film. As a reference sample, a gelatin-based film with no addition of conductive polymer was obtained.

2.3. Characterization Techniques

The surface morphology of the obtained films was characterized by optical and scanning electron microscopy (SEM) using a digital optical microscope (KH-7700 (Hirox, Tokyo, Japan)) and a two-beam scanning electron microscope (Helios Nanolab 400 (FEI, Hillsboro, OR, USA)).

The frequency dependencies of complex dielectric permittivity were measured in accordance with ASTM D150, using an Agilent E4980A high-precision LCR meter (Agilent Technologies, Inc., Santa Clara, CA, USA) and a measuring cell developed at Saint Petersburg Electrotechnical University "LETI" [29].

To measure the EMR absorption coefficient, we used a method based on a coplanar waveguide (CPW) with an impedance of 50 Ω, assigned to the frequency range of 50–2000 MHz, and a vector network analyzer ZVB-20 (Rohde&Schwarz, Munich, Germany). The design of the CPW was developed at Saint Petersburg Electrotechnical University "LETI" [29]. When measuring, the test sample was placed on the surface of the CPW.

The EMR absorption coefficient L (dB) was calculated using the following formula [30]:

$$L = -10\log_{10}\left(|S_{21}|^2 + |S_{11}|^2\right),$$

where $|S_{21}|$ and $|S_{11}|$ are the modules of complex transmission and reflection coefficients, respectively. The absorption coefficient's value, 10 dB, was equivalent to 90% power loss of transmitted EMR.

A 4200-SCS semiconductor characterization system (Keithley, Solon, OH, USA) and an M150 probe station (Cascade Microtech, Beaverton, OR, USA) were used to measure the surface electrical resistivity of samples using the four-probe method. In order to calculate the electrical resistivity of the samples, their thicknesses were measured using a micrometer with an accuracy of 5 µm [29]. Each sample was measured five times.

3. Results and Discussion

3.1. Surface Morphology of the Samples

The views of the obtained PANI film sample on a polyethylene substrate, the sample of gelatin film, and the sample of the gelatin–PANI composite film are given in Figure 1. The minimal binding radius of the gelatin-PANI composite film with a thickness of 200–400 µm was about 5 cm.

(**a**) (**b**) (**c**)

Figure 1. The view of the obtained samples: (**a**) the polyaniline (PANI) film on a polyethylene substrate; (**b**) the gelatin film; and (**c**) the gelatin-PANI composite film.

SEM images of the PANI film on a polyethylene substrate are given in Figure 2. As can be seen from the images, the film consists of PANI grains of 100–1000 nm, which presumably may be due to the fact that the film was directly obtained from an aniline solution with subsequent polymerization.

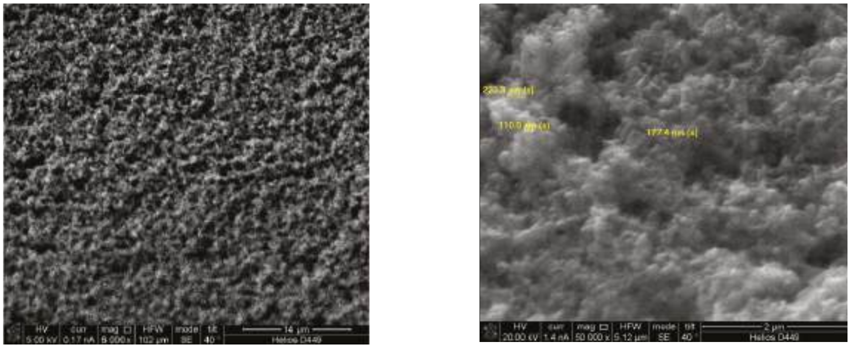

(**a**) (**b**)

Figure 2. SEM images of the PANI film on a polyethylene substrate: (**a**) low magnification and (**b**) high magnification.

The optical microscopy images of PANI film on a polyethylene substrate and gelatin–PANI samples are given in Figure 3.

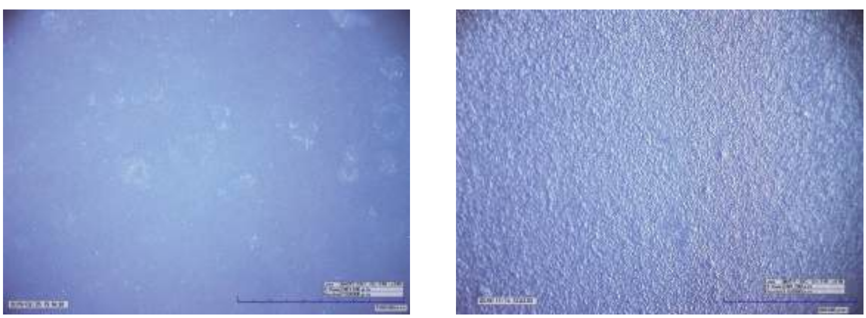

(**a**) (**b**)

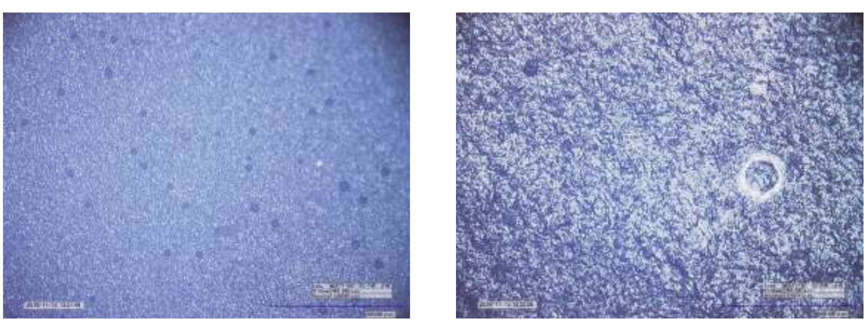

(**c**) (**d**)

Figure 3. *Cont.*

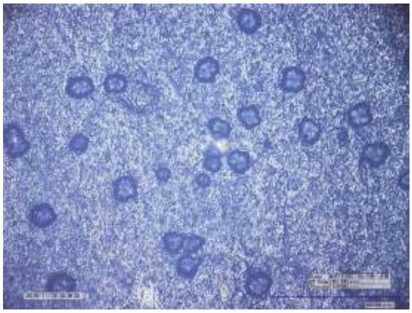

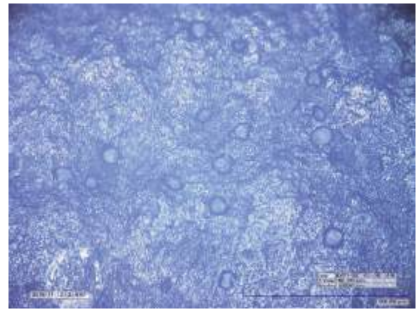

(**e**) (**f**)

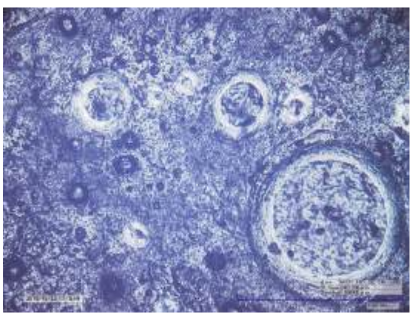

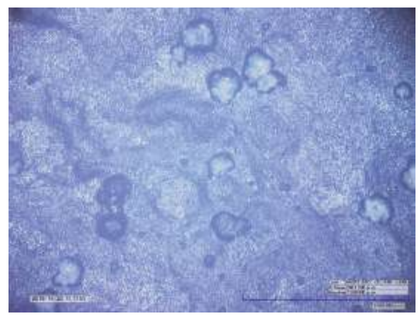

(**g**) (**h**)

Figure 3. Optical microscopy images of the samples: (**a**) the PANI film on a polyethylene substrate; (**b**) 3%-PANI-GEL; (**c**) 12%-PANI-GEL; (**d**) 22%-PANI-GEL; (**e**) 36%-PANI-GEL; (**f**) 46%-PANI-GEL; (**g**) 53%-PANI-GEL; and (**h**) 59%-PANI-GEL.

As shown in the obtained images, an increase in PANI content in the composition provokes the formation of larger particles of conductive polymer. A further increase in the content of PANI is possible with changes in synthesis technology.

3.2. Electrophysical Characteristics

The results of the electrical resistivity of the PANI films on a polyethylene substrate are shown in Figure 4.

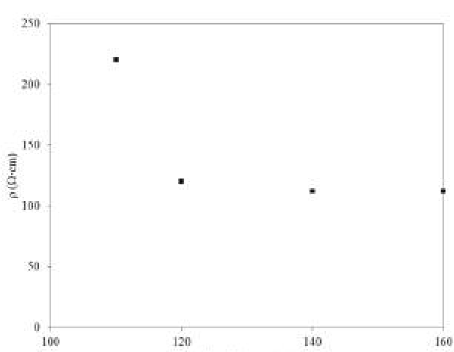

Figure 4. Thickness dependence of the electrical resistivity of the PANI films on a polyethylene substrate.

The electrical resistivity of PANI films decreases, whereas the film thickness increases and stops its decrease at a thickness of about 100–120 μm. The effect is similar to that described in [31] and may be due to the compaction of the structure of the PANI film on a nonconductive polyethylene substrate [32]. The value of the surface electrical resistivity of the PANI film may be increased by introducing additional dielectric components, or by selecting the PANI content in the gelatin–PANI composite in order to achieve an impedance matching with free space (Z = 377 Ω).

The frequency dependencies of the real and imaginary parts of the complex dielectric permittivity of gelatin–PANI composite samples are shown in Figure 5.

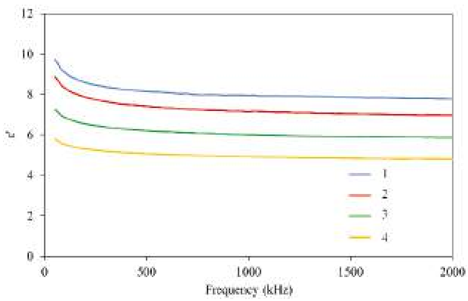

(**a**)

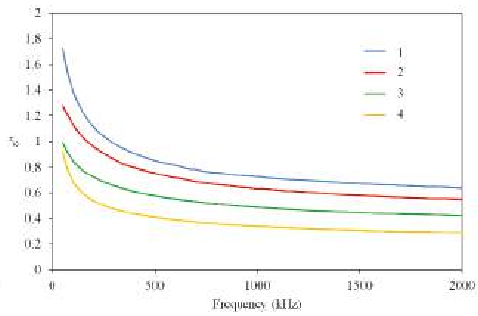

(**b**)

Figure 5. Frequency dependence of the complex dielectric permittivity of the gelatin–PANI composite films: (**a**) real part of dielectric permittivity; (**b**) imaginary part of dielectric permittivity; 1—gelatin; 2—22%-PANI-GEL; 3—36%-PANI-GEL; and 4—59%-PANI-GEL.

As can be seen from Figure 5, the maximum value of the real part of complex dielectric permittivity does not exceed 10; therefore, considering the absence of through electrical conductivity, the composite is close to a dielectric material and its EMR reflection coefficient can be low. An increase in PANI content leads to a decrease in real and imaginary parts of complex dielectric permittivity.

The effect may be due to several different possible reasons. The first is the fact that the dielectric permittivity of replaced gelatin is much higher in comparison with the dielectric permittivity of the gelatin–PANI composites [33]. The second reason is the structural features of the composite, which cause the appearance of electrical moments due to electrically isolated PANI particles, which can be represented as elementary electric dipoles. An increase in the size of PANI grains observed experimentally via optical microscopy leads to a decrease in the number of electric dipoles, a decrease in the electric moment of a unit volume, and, accordingly, a decrease in dielectric permittivity. Composites based on various conductive polymers can have ferroelectric properties and be characterized by a high-dielectric constant, which can be controlled by an external electric field or temperature [34,35]. The third possible reason is not due to physical processes within the composite and is due to the high inhomogeneity of gelatin-PANI composite film with a high content of PANI, which affects the measured values of complex dielectric permittivity due to an increased air gap between the measuring electrodes and the film surfaces.

3.3. EMR Absorption Measurement

The frequency dependencies of the EMR absorption coefficient for samples of PANI films of various thicknesses are shown in Figure 6.

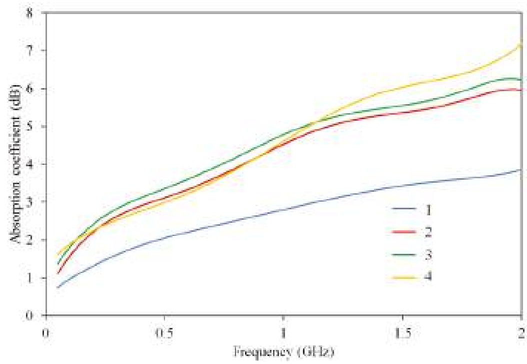

Figure 6. Frequency dependence of the electromagnetic radiation (EMR) absorption coefficient of the PANI films on a polyethylene substrate: 1—110 µm, 2—120 µm, 3—140 µm, and 4—160 µm.

The value of the EMR absorption coefficient reached 6–7 dB for PANI films with a thickness of over 120 µm, and changed insignificantly, while the thickness increased further. These results correlate with the data on the films' electrical resistivity measurements; hence, the assumption of the prevalent role of dielectric loss in PANI can be confirmed. At the same time, an application of continuous PANI films without a dielectric binder is restricted by a mismatch of their impedance with free space impedance and, consequently, by a high EMR reflection coefficient. For this reason, in our opinion, an estimation of the EMR absorption properties of gelatin–PANI composite films may be much more useful. The frequency dependence of the EMR absorption coefficient of gelatin–PANI composite films is shown in Figure 7.

As can be seen, the EMR absorption coefficient grows monotonously and reaches 4–5 dB, while the PANI content increases to 50 mas.%. In accordance with the optical microscopy and complex dielectric permittivity measurement data, the observed effect may be explained by two possible reasons. The first one is the change in film surface morphology, which, due to its high inhomogeneity, leads to an increase in the air gap between the CPW and film surfaces. Therefore, a further increase in the measured value of the EMR absorption coefficient becomes impossible. The second possible reason is a decrease in dielectric losses with an increase in PANI content. If the EMR saturation value maximum's origin is a technological limitation, it can be overcome by making changes to the synthesis technique.

The physical mechanisms of EMR absorption should be similar to those proposed in [20] since it considered composite films of the same thicknesses (250 µm) and with a similar PANI content (40 mas.%) in a dielectric binder, polystyrene. However, a direct comparison of the values of the absorption coefficients is not entirely correct due to the different frequency ranges of measurements (0.05–2 GHz and 9–18 GHz) and different measurement techniques (air-coaxial line and CPW). Nevertheless, the authors believe that the gelatin–PANI composite films will demonstrate similar or higher values of EMR absorption coefficient at frequencies over 8 GHz because, unlike polystyrene, gelatin binders possess intrinsic dielectric losses [29].

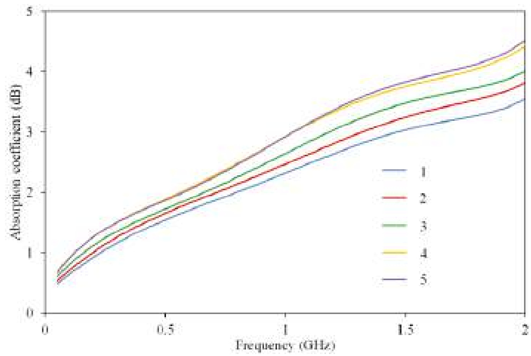

Figure 7. Frequency dependence of the EMR absorption coefficient of the gelatin-PANI composite films: 1—2%-PANI-GEL; 2—36%-PANI-GEL; 3—46%-PANI-GEL; 4—53%-PANI-GEL; and 5—22%-PANI-GEL.

4. Conclusions

As a result of the study, it was found that PANI-based composite films with a film thickness of about 200–400 µm and a minimum bending radius of about 5 cm are capable of providing an EMR absorption coefficient of up to 5 dB in a frequency range 0.05–2 GHz. The possibility of using the obtained composite films without introducing additional absorbing fillers (carbon nanotubes, graphene, magnetic nanoparticles, etc.) into the composition allows to offer a cheap and technologically advanced material to ensure the EMC of electronic devices designed for standard application conditions. Moreover, due to the low value of the real part of complex dielectric permittivity (not more than 10) and the absence of through electrical conductivity, as well as the low temperature of production (not higher than 60 °C), gelatin–PANI composite films can be applied directly to printed circuit boards to form a continuous conformal protective layer on their surfaces.

Author Contributions: Conceptualization, I.K.K. and V.V.L.; methodology, I.K.K. and K.G.G.; formal analysis, I.K.K. and K.G.G.; investigation, K.G.G., V.S.B., V.A.G., M.G.I., O.N.M. and D.O.T.; data curation, K.G.G.; writing—original draft preparation, K.G.G.; writing—review and editing, I.K.K. and V.V.L.; visualization, K.G.G.; supervision, V.V.L.; project administration, I.K.K.; funding acquisition, I.K.K. and V.V.L. All authors have read and agreed to the published version of the manuscript.

Funding: This research was funded by Russian Science Foundation, grant number 16-19-00107.

Conflicts of Interest: The authors declare no conflicts of interest.

References

1. Ott, H.W. *Electromagnetic Compatibility Engineering*; John Wiley & Sons: Hoboken, NJ, USA, 2009; pp. 243–245. ISBN 978-0-470-18930-6.
2. Mouritz, A.P. *Introduction to Aerospace Materials*; Woodhead Publishing: Oxford, UK, 2012; pp. 296–298, ISBN 978-0-85709-515-2.
3. Fang, F.; Li, Y.-Q.; Xiao, H.-M.; Hu, H.; Fu, S.-Y. Layer-structured silver nanowire/polyaniline composite film as high performance X-band EMI shielding material. *J. Mater. Chem. C* **2016**, *19*, 4193–4203. [CrossRef]
4. Faisal, M.; Khasim, S. Polyaniline–antimony oxide composites for effective broadband EMI shielding. *Iran Polym. J.* **2013**, *22*, 473–480. [CrossRef]
5. Khasim, S. Polyaniline-Graphene nanoplatelet composite films with improved conductivity for high performance X-band microwave shielding applications. *Res. Phys.* **2019**, *12*, 1073–1081. [CrossRef]
6. Shakir, M.F.; Khan, A.N.; Khan, R.; Javed, S.; Tariq, A.; Azeem, M.; Riaz, A.; Shafqat, A.; Cheema, H.M.; Akram, M.A.; et al. EMI shielding properties of polymer blends with inclusion of graphene nano platelets. *Res. Phys.* **2019**, *14*, 102365. [CrossRef]
7. Cheng, K.; Li, H.; Zhu, M.; Qiu, H.; Yang, J. In situ polymerization of graphene-polyaniline@polyimide composite films with high EMI shielding and electrical properties. *RSC Adv.* **2020**, *10*, 2368–2377. [CrossRef]

8. Kumar, A.; Kumar, V.; Kumar, M.; Awasthi, K. Synthesis and Characterization of Hybrid PANI/MWCNT Nanocomposites for EMI Applications. *Polym. Compos.* **2018**, *39*, 3858–3868. [CrossRef]
9. Li, H.; Lu, X.; Yuan, D.; Sun, J.; Erden, F.; Wang, F.; He, C. Lightweight flexible carbon nanotube/polyaniline films with outstanding EMI shielding properties. *J. Mater. Chem. C* **2017**, *5*, 8694–8698. [CrossRef]
10. Shi, S.; Zhang, L.; Li, J. Complex permittivity and electromagnetic interference shielding properties of Ti_3SiC_2/polyaniline composites. *J. Mater. Sci.* **2009**, *44*, 945–948. [CrossRef]
11. Saboor, A.; Khalid, S.M.; Jan, R.; Khan, A.N.; Zia, T.; Farooq, M.U.; Afridi, S.; Sadiq, M.; Arif, M. PS/PANI/MoS_2 Hybrid Polymer Composites with High Dielectric Behavior and Electrical Conductivity for EMI Shielding Effectiveness. *Materials* **2019**, *12*, 2690. [CrossRef]
12. Rahul, D.S.; Pais, T.P.M.; Sharath, N.; Ali, S.A.; Faisal, M. Polyaniline-copper oxide composite: A high performance shield against electromagnetic pollution. *AIP Conf. Proc.* **2015**, *1665*, 140021. [CrossRef]
13. Yang, Z.; Zhag, Y.; Wen, B. Enhanced electromagnetic interference shielding capability in bamboo fiber@polyaniline composites through microwave reflection cavity design. *Compos. Sci. Technol.* **2019**, *178*, 41–49. [CrossRef]
14. Zhang, Y.; Qiu, M.; Yu, Y.; Wen, B.; Cheng, L. A novel polyaniline-coated bagasse fiber composite with core-shell heterostructure provides effective electromagnetic shielding performance. *ACS Appl. Mater. Interfaces* **2017**, *9*, 809–818. [CrossRef]
15. Wanasinghe, D.; Aslani, F.; Ma, G.; Habibi, D. Review of polymer composites with diverse nanofillers for electromagnetic interference shielding. *Nanomaterials* **2020**, *10*, 541. [CrossRef] [PubMed]
16. Kamchi, N.E.; Belaabed, B.; Wojkiewicz, J.L.; Lamouri, S.; Lasri, T. Hybrid polyaniline/nanomagnetic particles composites: High performance materials for EMI shielding. *J. Appl. Polym. Sci.* **2013**, *127*, 4426–4432. [CrossRef]
17. Zahari, M.H.B.; Guan, B.H.; Meng, C.E. Development and evaluation of $BaFe_{12}O_{19}$-PANI-MWCNT composite for electromagnetic interference (EMI) shielding. *Prog. Electromagn. Res. C* **2018**, *80*, 55–64. [CrossRef]
18. Niu, Y. Preparation of polyaniline/polyacrylate composites and their application for electromagnetic interference shielding. *Polym. Compos.* **2006**, *27*, 627–632. [CrossRef]
19. Niu, Y. Electromagnetic interference shielding with polyaniline nanofibers composite coatings. *Polym. Eng. Sci.* **2008**, *48*, 355–359. [CrossRef]
20. Shakir, M.F.; Rashid, I.A.; Tariq, A.; Nawab, Y.; Afzal, A.; Nabeel, M.; Naseem, A.; Hamid, U. EMI shielding characteristics of electrically conductive polymer blends of PS/PANI in microwave and IR region. *J. Electronic Mat.* **2020**, *49*, 1660–1665. [CrossRef]
21. Sobhaa, A.P.; Sreekalac, P.S.; Narayanankuttya, S.K. Electrical, thermal, mechanical and electromagnetic interference shielding properties of PANI/FMWCNT/TPU composites. *Prog. Org. Coat.* **2017**, *113*, 168–174. [CrossRef]
22. Raagulan, K.; Braveenth, R.; Kim, B.M.; Lim, K.J.; Lee, S.B.; Kim, M.; Chai, K.Y. An effective utilization of MXene and its effect on electromagnetic interference shielding: Flexible, free-standing and thermally conductive composite from MXene–PAT–poly(p-aminophenol)–polyaniline co-polymer. *RSC Adv.* **2020**, *10*, 1613–1633. [CrossRef]
23. Bhowmick, B.; Mollick, M.R.; Mondal, D.; Maity, D.; Bain, M.K.; Bera, N.K.; Rana, D.; Chattopadhyay, S.; Chakraborty, M.; Chattopadhyay, D. Poloxamer and gelatin gel guided polyaniline nanofibers: Synthesis and characterization. *Polym. Int.* **2014**, *63*, 1505–1512. [CrossRef]
24. Li, M.; Guo, Y.; Wei, Y.; MacDiarmid, A.G.; Lelkes, P.I. Electrospinning polyaniline-contained gelatin nanofibers for tissue engineering applications. *Biomaterials* **2006**, *27*, 2705–2715. [CrossRef] [PubMed]
25. Ostrovidov, S.; Ebrahimi, M.; Bae, H.; Nguyen, H.K.; Salehi, S.; Kim, S.B.; Kumatani, A.; Matsue, T.; Shi, X.; Nakajima, K.; et al. Gelatin-polyaniline composite nanofibers enhanced excitation-contraction coupling system maturation in myotubes. *ACS Appl. Mater. Interfaces* **2017**, *49*, 42444–42458. [CrossRef] [PubMed]
26. Xue, J.; Liu, Y.; Darabi, M.A.; Tu, G.; Huang, L.; Ying, L.; Xiao, B.; Wu, Y.; Xing, M.; Zhang, L.; et al. An injectable conductive Gelatin-PANI hydrogel system serves as a promising carrier to deliver BMSCs for Parkinson's disease treatment. *Mater. Sci. Eng. C* **2019**, *100*, 584–597. [CrossRef]
27. Blinova, N.V.; Trchová, M.; Stejskal, J. The polymerization of aniline at a solution–gelatin gel interface. *Eur. Polym. J.* **2009**, *45*, 668–673. [CrossRef]
28. Long, Y.; Huang, K.; Yuan, J.; Han, D.; Niu, L.; Chen, Z.; Gu, C.; Jin, A.; Duvail, J.L. Electrical conductivity of a single Au/polyaniline microfiber. *Appl. Phys. Lett.* **2006**, *88*, 162113. [CrossRef]

29. Gareev, K.G.; Bagrets, V.S.; Khmelnitskiy, I.K.; Ivanitsa, M.G.; Testov, D.O. Research and Development of "Gelatin–Conductive Polymer" Composites for Electromagnetic Compatibility. In Proceedings of the 2020 IEEE Conference of Russian Young Researchers in Electrical and Electronic Engineering (EIConRus), St. Petersburg/Moscow, Russia, 27–30 January 2020; pp. 1069–1072. [CrossRef]
30. Gareev, K.G.; Luchinin, V.V.; Sevost'yanov, E.N.; Testov, I.O.; Testov, O.A. Frequency dependence of an electromagnetic absorption coefficient in magnetic fluid. *Tech. Phys.* **2019**, *89*, 954–957. [CrossRef]
31. Haberko, J.; Raczkowska, J.; Bernasik, A.; Rysz, J.; Nocuń, M.; Nizioł, J.; Łużny, W.; Budkowski, A. Conductivity of thin polymer films containing polyaniline. *Mol. Cryst. Liq. Cryst.* **2008**, *485*, 48–55. [CrossRef]
32. Vanga Bouanga, C.; Fatyeyeva, K.; Baillif, P.-Y.; Bardeau, J.-F.; Khaokong, C.; Pilard, J.-F.; Tabellout, M. Study of dielectric relaxation phenomena and electrical properties of conductive polyaniline based composite films. *J. NonCrystal. Sol.* **2010**, *356*, 611–615. [CrossRef]
33. Altarawneh, M.M.; Alharazneh, G.A.; Al-Madanat, O.Y. Dielectric properties of single wall carbon nanotubes-based gelatin phantoms. *J. Adv. Dielectr.* **2018**, *8*, 1850010. [CrossRef]
34. Zhang, W.; Ye, H.-Y.; Graf, R.; Spiess, H.W.; Yao, Y.-F.; Zhu, R.-Q.; Xiong, R.-G. Tunable and Switchable Dielectric Constant in an Amphidynamic Crystal. *J. Am. Chem. Soc.* **2013**, *135*, 5230–5233. [CrossRef] [PubMed]
35. Ye, H.-Y.; Zhang, Y.; Fu, D.-W.; Xiong, R.-G. An above-room-temperature ferroelectric organo–metal halide perovskite: (3-Pyrrolinium)($CdCl_3$). *Angew. Chem. Int. Ed.* **2014**, *53*, 1–7. [CrossRef] [PubMed]

electronics

MDPI

Article

Performance Study of Split Ferrite Cores Designed for EMI Suppression on Cables

Adrian Suarez [1,*], Jorge Victoria [1,2], Jose Torres [1], Pedro A. Martinez [1], Antonio Alcarria [2], Joaquin Perez [1], Raimundo Garcia-Olcina [1], Jesus Soret [1], Steffen Muetsch [2] and Alexander Gerfer [2]

1 Department of Electronic Engineering, University of Valencia, 46100 Burjassot, Spain; jorge.victoria@we-online.de (J.V.); jose.torres@uv.es (J.T.); pedro.a.martinez@uv.es (P.A.M.); joaquin.perez-soler@uv.es (J.P.); raimundo.garcia@uv.es (R.G.-O.); jesus.soret@uv.es (J.S.)

2 Würth Elektronik eiSos GmbH & Co. KG, 74638 Waldenburg, Germany; antonio.alcarria@we-online.de (A.A.); steffen.muetsch@we-online.de (S.M.); alexander.gerfr@we-online.de (A.G.)

* Correspondence: adrian.suarez@uv.es

Received: 14 October 2020; Accepted: 22 November 2020; Published: 24 November 2020

Abstract: The ideal procedure to start designing an electronic device is to consider the electromagnetic compatibility (EMC) from the beginning. Even so, EMC problems can appear afterward, especially when the designed system is interconnected with external devices. Thereby, electromagnetic interferences (EMIs) could be transmitted to our device from power cables that interconnect it with an external power source or are connected to another system to establish wired communication. The application of an EMI suppressor such as a sleeve core that encircles the cables is a widely used technique to attenuate EM disturbances. This contribution is focused on the characterization of a variation of this cable filtering solution based on openable core clamp or snap ferrites. This component is manufactured by two split parts pressed together by a snap-on mechanism which turns this into a quick, easy to install solution for reducing post-cable assembly EMI problems. The performance of three different materials, including two polycrystalline (MnZn and NiZn) materials and nanocrystalline (NC) solution, are analyzed in terms of effectiveness when the solid sleeve cores are split. The possibility of splitting an NC core implies an innovative technique due to the brittleness of this material. Thus, the results obtained from this research make it possible to evaluate this sample's effectiveness compared to the polycrystalline ones. This characterization is carried out by the introduction of different gaps between the different split-cores and analyzing their behavior in terms of relative permeability and impedance. The results obtained experimentally are corroborated with the results obtained by a finite element method (FEM) simulation model with the aim of determining the performance of each material when it is used as an openable core clamp.

Keywords: electromagnetic interference (EMI) suppressors; sleeve ferrite cores; cable filtering; nanocrystalline (NC); split-core; snap ferrite; gap; DC currents; relative permeability; impedance

1. Introduction

The control of EMI in electronic devices is an increasing issue faced by designers in order to ensure that devices comply with EMC requirements to operate simultaneously without inferring with each other. This fact is due to the trends towards higher component integration, printed circuit board (PCB) size and thickness reduction, and the miniaturization of the device housings. Besides, other factors, such as higher switching frequencies in power converters and communication data rates in digital circuits, could lead to EMI problems [1,2]. Consequently, EMC engineering should be handled with the system approach, considering EMC throughout the design process to prevent possible EMI problems that could degrade device performance. Therefore, adopting specific solutions as early as possible in the design stage to meet the EMC requirements is of primary importance to reduce penalties from the standpoint of costs, time-to-market, and performance [3,4]. The EMC testing process can reveal that the shielding of a certain cable is needed or may even detect an unexpected EMI source when the designed device is connected to external modules, such as a power supply or to another device to communicate with it. When the cables represent the EMI source, that implies failing the conducted or radiated emissions test, and a widely used technique is applying an EMI suppressor such as a cable ferrite [4].

A cable ferrite's effectiveness to reduce EMI in cables is defined by its capability to increase the flux density of a specific field strength created around a conductor. The presence of noise current in a conductor generates an undesired magnetic field around it that can result in EMI problems. When a cable ferrite is applied in the conductor, the magnetic field is concentrated into magnetic flux inside the cable ferrite because it provides a higher magnetic permeability than air. As a result, the flowing noise current in the conductor is reduced and, thus, the EMI is attenuated. Currents that flow in cables (with two or more conductors) can be divided into differential mode (DM) and common mode (CM) depending on the directions of propagation. Although DM currents are usually significantly higher than CM currents, one of the most common radiated EMI problems is originated by CM currents flowing through the cables of the system [5]. CM currents, despite not having a high value, have a much greater interfering potential. This fact is because only a few microamps are required to flow through a cable to fail radiated emission requirements [4]. The use of a cable ferrite is an efficient solution to filter the CM currents in cables because, if a pair of adjacent conductors is considered, when the cable ferrite is placed over both signal and ground wires, the CM noise is reduced. As shown in Figure 1, the CM currents in both wires flow in the same direction, so the two magnetic fluxes in the cable ferrite are added together, and the filtering action occurs. The intended (DM) current is not affected by the presence of the cable ferrite because the DM current travels in opposite directions and it is transmitted through the signal and returns. Thus, the currents of the two conductors are opposing, meaning they cancel out and the cable ferrite has no effect [6]. This ability to attenuate only the undesirable CM disturbances is a very interesting feature of this kind of component [7–9].

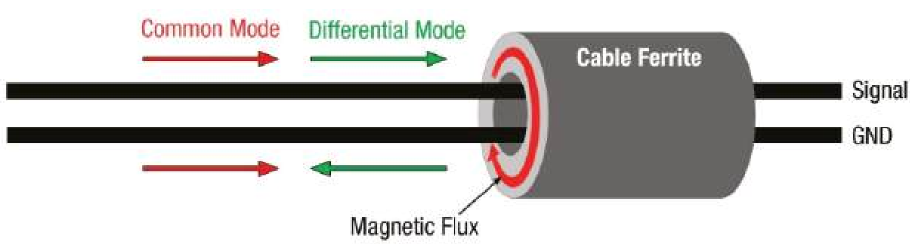

Figure 1. Diagram of common mode (CM) and differential mode (DM) currents passing through a cable ferrite with two adjacent conductors (signal and return paths).

This component represents a solution when the cables turn into an EMI source. It can be applied to peripheral and communication cables such as multiconductor USB or video cables to prevent interferences that could be propagated along the wire, affecting the devices that are interconnected [10,11]. This component is also widely used to reduce high-frequency oscillations caused by the increasingly fast switching in power inverters and converters with cables attached without scarifying the switching speed and increasing the power loss. Therefore, selecting the proper cable ferrite makes it possible to reduce the switching noise by increasing the propagation path impedance in the desired frequency range [5].

The application of cable ferrites is a widely used technique to reduce EMI in cables, despite the drawbacks that the integration of an extra component can involve in terms of cost and production of the system [12]. Nevertheless, these drawbacks are usually compensated by the effectiveness of cable ferrites to filter interferences without having to redesign the electronic circuit [6,7]. Manufacturers provide a wide range of ferrite cores with different shapes, dimensions and compositions, but the most widely used solutions applied to cables are the sleeve (or tube) ferrite cores or their split variation, the openable core clamp (or snap ferrites) [13]. This component is manufactured from two split parts pressed together by a snap-on mechanism, turning this into a quick, easy to install solution for reducing post-cable assembly EMI problems. The main advantage of snap ferrites compared to solid sleeve ferrite cores is the possibility to add them to the final design, without manufacturing a specific cable that includes the sleeve ferrite core before assembling its connectors.

Nevertheless, the halved ferrite's performance will be lower than that of a solid core with the same composition and dimensions in terms of the relative permeability (μr) and hence the impedance introduced in the cable [14]. This performance degradation is caused by the gap introduced between the split parts. Additionally, the presence of a defined air gap between the split parts can turn into an advantage from the standpoint of the core saturation because it allows for higher DC currents before saturation is reached as compared to solid cores. For applications such as power supplies or motor drivers, high DC currents flow through the cable, and the performance of the cable ferrite can be degraded [8]. Therefore, in these situations, it is interesting to halve the cable ferrite with the aim of introducing a controlled gap that reduces the influence of DC currents into it [15,16].

The materials selected to carry out the characterization in terms of cable ferrite performance considering gap and stability to DC currents are two ceramic cores based on MnZn and NiZn and a third core of nanocrystalline (NC) structure. One of the main advantages of MnZn and NiZn materials is the possibility of creating cores with many different shapes and the possibility of halving them without modifying their internal structure [17,18]. Preliminary studies have shown that NC sleeve ferrite cores provide a significant effectiveness when used as an EMI suppressor [17,19,20]. Nevertheless, the internal structure and manufacturing process have traditionally made it complicated to obtain a split-core sample that can be used as a snap ferrite, keeping its effectiveness. Therefore, a prototype of a split-core of an NC sample has been manufactured based on a new cutting and assembling technique that makes it possible to analyze this material's performance when it is halved.

Consequently, one of the main objectives of this contribution is to analyze the dependencies between the gap parameter and the performance in terms of impedance provided by the snap ferrite. This analysis is performed through an experimental measurement setup that is compared with the results obtained through a finite element method (FEM) simulation model. The simulation model helps to determine the study's accuracy, specifically in the high-frequency range where parasitic elements may affect the experimental results [20]. Likewise, the stability of three solid (not split) and split cable ferrites based on different compositions are characterized in order to determine the influence of DC currents on the impedance response provided. The results obtained from this study make it possible to compare the different materials to find out which one is the most efficient, depending on the frequency range.

Thereby, the three different materials and their structures are described in Section 2 through the main magnetic parameters, such as the relative permeability and the reluctance caused by introducing a gap. Section 3 defines the measurement setups employed to perform the experimental results and the designed FEM simulation model description. Subsequently, in Section 4, the three different samples' performance under test is shown in terms of impedance versus frequency. The dependencies on the air gap introduced in the split-cores and the influence on the injection of DC currents are discussed. Finally, the main conclusions are summarized in Section 5 to determine the performance of each material when used as an openable core clamp.

2. Magnetic Properties

The magnetically soft ferrites are widely used for manufacturing EMI suppressors as cable ferrites. Conventionally, the most used ferrite cores for filtering applications are based on ceramic materials (also known as polycrystalline materials) and, although they do not belong to the metals group, they are made from metal oxides such as ferrite, nickel and zinc. MnZn and NiZn represent two extensively used solutions due to their heat resistance, hardness, and high resistance to pressure. An advantage of ceramic materials is the possibility of manufacturing components with many different shapes and dimensions. The remarkable fact about the ceramic ferrites is that they combine extremely high electrical resistivity with reasonably good magnetic properties [21]. The starting material is iron oxide Fe_2O_3 that is mixed with one or more divalent transition metals, such as manganese, zinc, nickel, cobalt or magnesium [14]. The manufacturing procedure can be divided into these steps. First, the base materials are weighed into the desired proportions and wet mixed in ball mills to obtain a uniform distribution and particle size. Next, the water is removed in a filter press, and the ferrite is loosely pressed into blocks and dried. It is then pre-fired (calcined) at about 1000 °C to form the ferrite. The pre-sintered material is then milled to obtain a specific particle size. Subsequently, the dry powder is mixed with an organic binder and lubricants before being shaped by a pressing technique to obtain the final form. Finally, the resultant green core is subjected to a heating and cooling cycle, reaching temperatures higher than 1150 °C, promoting any unreacted oxides to be formed into ferrite. The manufacturing procedure and the material mix are essential to define a ceramic core's magnetic properties. With MnZn materials, it is possible to obtain samples that provide initial permeabilities of the order of 1000–20,000 and provide a low resistivity (0.1–100 Ω·m). Their range of frequency for EMI suppression applications covers from hundreds of kHz to some MHz.

Regarding NiZn materials, these provide initial permeabilities of the order of 100–2000, so they are intended for a higher frequency operation than MnZn, covering from tens of MHz up to several hundreds of MHz. In terms of resistivity, NiZn materials reach high values (about 10^4–10^6 Ω·m) [15,21,22]. Therefore, considering the structure of ceramic cores, they can be considered as isotropic.

The structure and manufacturing technique used for ceramics make it possible to produce split-cores or cut a solid core after its production with water-cooled diamond tools to build snap ferrites [14]. The NC cores' manufacturing procedure is quite different from the one used for ceramic production since they are formed by a continuous laminar structure that is wound to form the final core. The tape-wound structure is based on an amorphous ribbon of only 7–25 micrometers in thickness. It is generated by melting the base material by heating it at 1300 °C and depositing it on a high-speed cooling wheel (100 km/h) that reduces the temperature of the material to 20 °C at a rate of 10^6 K/s. After that, the rolled material is exposed to an annealing process, usually under a transversal and longitudinal magnetic field. This treatment affects the magnetic properties, resulting in ultrafine crystals with a size of the order of 7–20 nm. Finally, an epoxy coating or an additional protective case is needed to protect the sample, due to the brittle nature of the tape. Depending on the parameters selected during the manufacturing procedure, NC samples can provide initial permeability values in the range of 15,000 to 150,000. Electrical resistivity is relatively high even if it is considered a metallic material, generally over 10^{-6} Ω·m [14,15,17,23]. The NC material structure presents the advantage of designing smaller components with more significant magnetic properties for EMI suppression [19,20,24–27]. Figure 2 shows the NC core before adding the protective coating and its manufacturing procedure diagram.

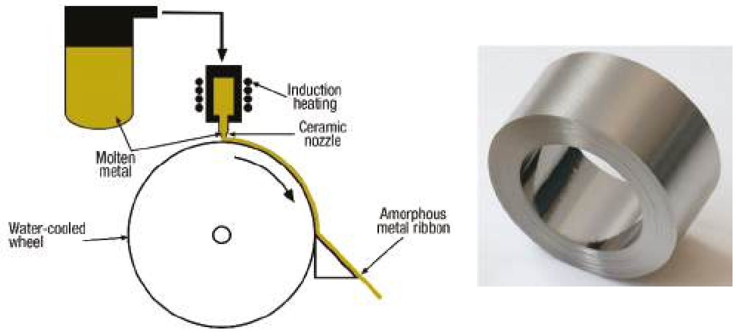

Figure 2. Nanocrystalline manufacturing procedure diagram and nanocrystalline (NC) final core sample without the protective coating.

Ceramic and NC samples can be manufactured as sleeve cores but have a different internal structure. From the point of view of the flux, it travels only in the rolling direction of the amorphous ribbon in the NC core. In ceramics, the flux is distributed uniformly because the material is a single homogeneous unit [21]. This different structure will result in a different behavior when the core is split into two parts for use as a snap ferrite. In ceramic cores, a performance reduction in terms of relative permeability when they are split is expected. However, we could anticipate that in the case of the NC structure, this decrease would be significant. This fact could be considered because when the NC sample is halved, the wound core is cut, limiting the flux path. Thereby, the halved faces have been plated in order to connect both halved parts with the aim of reducing the gap of the resultant snap core. Table 1 and Figure 3 show the dimensions of the samples used to develop characterization. Note that the split samples have the same dimensions as the solid cores.

Table 1. List of cable ferrite samples used in this research.

Magnetic Material	Outer Diameter (OD) (mm)	Inner Diameter (ID) (mm)	Height (H) (mm)	Thickness (mm)
NC	19.2	11.7	25.4	7.5
MnZn	18.6	10.2	25.2	8.4
NiZn	18.6	10.2	25.1	8.4

Figure 3. Non-split NC and split-core sample (**left**) and non-split ceramic and split-core sample (**right**).

The solid and split-cores' behavior based on the three different materials is analyzed in this section through the relative permeability. The permeability of magnetic materials generally depends on the magnetic flux density, DC bias currents, temperature, frequency, and intrinsic material properties [15,17]. When an air gap is included in a closed magnetic circuit, the circuit's total permeability is called the effective relative permeability μ_e and this is lower than the permeability of the original solid core without the presence of the air gap. In terms of EMI suppression, reducing the relative permeability in a cable ferrite is generally related to the decrease in its ability to attenuate interferences. However, the presence of an air gap is sometimes desired to increase the DC bias capability of the core or to reduce the permeability to achieve a more predictable and stable response with the aim of shifting the resonance frequency (f_r) to higher values to reduce the effects of dimensional effects [28,29].

When the two parts of the split-core are joined, a certain air gap remains between them that results in a magnetic reluctance (R) increase, since the gap represents an opposition to the magnetic flux (Φ) normal flow [15,30]. As shown in Figure 4, this effect is analogous to adding a series resistor in an electronic circuit to reduce the magnitude of the current. In Figure 4, R_c represents the reluctance of the core, R_g the reluctance of the gap, Φ the magnetic flux that flows through the magnetic path length of the core (l_c), l_g the length of the air gap, i the current that flows through the conductor and N the number of turns.

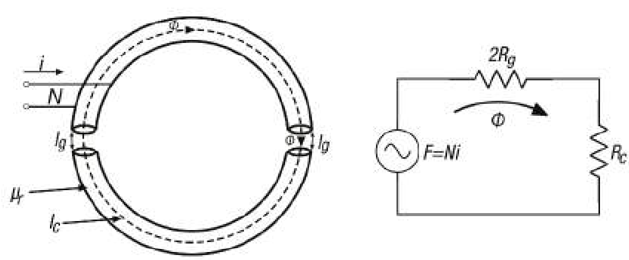

(**a**) (**b**)

Figure 4. Split-core with air gaps: (**a**) Magnetic flux distribution diagram and (**b**) the magnetic circuit of a split-core with two air gaps.

The general expression to obtain the magnetic reluctance is given by [15]:

$$R = \frac{l}{\mu_r \mu_0 A} \left[H^{-1}\right] \tag{1}$$

where l corresponds to the magnetic path length and A to the cross-sectional area. The l and A parameters are obtained from the dimensional features of the sample, considering a toroid with a rectangular cross-section:

$$l = \pi\left(\frac{OD}{2} + \frac{ID}{2}\right)[m] \tag{2}$$

$$A = H\left(\frac{OD}{2} - \frac{ID}{2}\right)[m] \tag{3}$$

where H is the core's height and OD and ID are the outer and inner diameter, respectively. The overall reluctance of the split-core considering the air gap can be calculated from (1) as the sum of the reluctance core (R_c) and reluctance air gap (R_g) [13,15]:

$$R = R_c + 2R_g = \frac{l_c - l_g}{\mu_r \mu_0 A} + \frac{2l_g}{\mu_0 A} \left[H^{-1}\right] \tag{4}$$

thereby, the air gap factor (F_g) is

$$F_g = \frac{R}{R_c} = \frac{R_c + 2R_g}{R_c} = 1 + \frac{2R_g}{R_c} = 1 + \frac{\mu_r 2l_g}{l_c} \tag{5}$$

and the effective relative permeability of a core with an air gap is [14,15,31]:

$$\mu_e = \frac{\mu_r}{1 + \frac{\mu_r 2l_g}{l_c}} = \frac{\mu_r}{F_g}. \tag{6}$$

Equation (6) represents the most common and simplified model to approximate the effective permeability caused by an air gap since it underestimates the value of μ_e because it does not consider the effect of the fringing flux across the air gap [32]. In the case of toroid cores, to estimate the influence of the air gap introduced when the core is split into two parts, l_g is usually considered to be twice the spacer thickness [15,32]. In order to characterize the reduction of the relative permeability caused by an air gap, the three solid (not split) cores of Table 1 are compared with three split-cores of the same material and dimensions but introducing four different gaps. Thereby, five study cases are carried out for each core material:

1. Non-split-core: core without a gap.
2. Split-core $g0$: both parts of the core are joined without fixing a gap value. In order to differentiate this case with the non-split-core, a gap value of 0.01 mm is considered.
3. Split-core $g1$: both parts of the core are joined by fixing a gap value of 0.07 mm.
4. Split-core $g2$: both parts of the core are joined by fixing a gap value of 0.14 mm.
5. Split-core $g3$: both parts of the core are joined by fixing a gap value of 0.21 mm.

Figure 5 shows the experimental relative permeability measured for each of the three cores included in Table 1, considering the five different cases in terms of the gap introduced. The experimental traces (solid traces) are compared with the effective relative permeability calculated (dotted traces) by using Equation (6), considering the four gaps defined above. This parameter has been calculated from the experimental relative permeability of the non-split-core sample. These data are expressed through a vector formed by 801 frequency points with their corresponding permeability values. The effective relative permeability of a core with a specific gap is determined by computing these values point by point. Thereby, the air gap factor value F_g changes throughout the frequency range analyzed. It is possible to observe that both NiZn and MnZn graphs show a similar response between calculated and experimental results. There is a significant match in the low-frequency region, particularly in the NiZn samples, since they provide a lower and more stable permeability than MnZn cores. In the high-frequency region, the calculated effective relative permeability is lower than the experimentally measured one, verifying that Equation (6) provides an underestimation of this. Another difference between NiZn and MnZn traces is observed by comparing the $g0$ traces because the initial permeability decreases mostly in MnZn because the original non-split-core yields a higher initial permeability than the NiZn sample. The estimation of $g0$ traces was obtained by fixing a gap of 0.01 mm between both split parts in order to simulate the real snap ferrite's behavior, and the estimated values match with the experimental data [13]. The NC graph shows a different behavior than the ceramic core since the experimental and calculated permeability only matches in the low-frequency region. Therefore, unlike ceramic cores, it is not possible to estimate with Equation (6) the effective relative permeability of NC in the middle and high-frequency region when used as a snap ferrite due to its different internal structure.

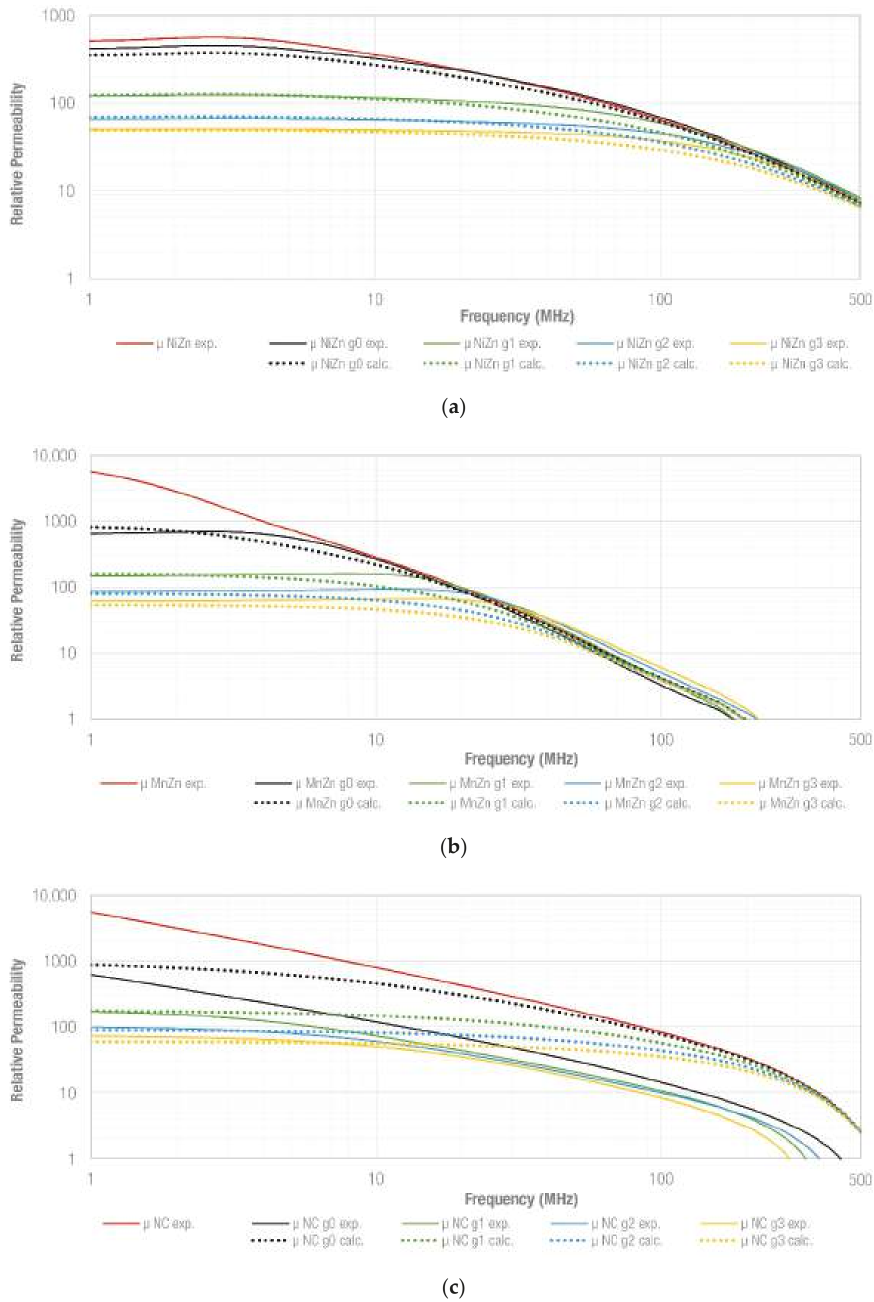

Figure 5. Comparison between experimental (solid traces) and estimated (dotted traces) effective permeability considering different gaps for NiZn, MnZn and NC samples: (**a**) NiZn non-split (red trace) and split cases; (**b**) MnZn non-split (red trace) and split cases and (**c**) NC non-split (red trace) and split cases.

3. Characterization Setups

EMI suppressors, such as cable ferrites, are usually classified by the impedance that they can introduce in a specific frequency range when they embrace a conductor. This parameter represents the magnitude of the impedance that can be represented from a series equivalent circuit mainly based on a resistive and inductive component [13,20]. The resistive component is connected to the imaginary part of the relative permeability representing the core's losses, whereas the real part of the permeability is related to the inductive component [22]. Therefore, there is a direct relationship between the core material's magnetic behavior and its performance in terms of impedance. Other factors that contribute to defining the impedance provided by a cable ferrite are the dimensions and the shape [19].

3.1. Impedance Measurement Setup

The experimental magnitude of the impedance of each sample is obtained by using the E4991A RF Impedance/Material Analyzer (Keysight, Santa Rosa, CA, USA) connected to the Terminal Adapter 16201A (Keysight, Santa Rosa, CA, USA). This adapter makes it possible to introduce into the measurement setup the 16200B External DC Bias (Keysight, Santa Rosa, CA, USA) that allows for supplying a bias current through the cable ferrite of up to 5 A using a 7 mm port and an external DC current source. Finally, the cable ferrite is connected by means of the Spring Clip Fixture 16092A (Keysight, Santa Rosa, CA, USA) that is connected to the 16200B test fixture [33]. After it is properly calibrated, this measurement setup is able to characterize cable ferrites from 1 MHz to 500 MHz since the E4991A equipment can operate from 1 MHz and the 16200B test fixture up to 500 MHz. Figure 6 shows the described experimental measurement setup.

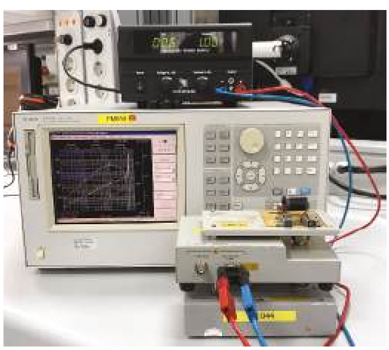

(**a**)

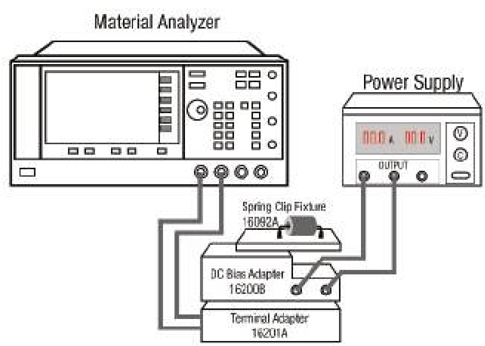

(**b**)

Figure 6. Impedance measurement setup with the DC bias test fixture connected: (**a**) Photograph of the measurement setup and (**b**) diagram blocks of the measurement setup.

This setup provides the experimental impedance of the split and non-split-cores, analyzing them when there is no presence of DC currents and increasing this parameter up to 5 A. The results obtained can be compared to analyze the behavior of each of the three materials characterized in this contribution in terms of the gap introduced in the core and the value of bias current injected.

3.2. Simulation Model

The different split and non-split cable ferrites' performance and the relationship between the impedance provided and the air gap introduced are specifically examined through an electromagnetic analysis simulator (Ansys Electronics Desktop). The proposed simulation model is shown in Figure 7. It is formed by a copper conductor that crosses a cylindrical core defined by the material properties of each of the materials described in Section 2. The conductor is connected to two ports (input and output) referenced to a perfect electrical plane located at a certain distance under it. This simulation setup represents a transmission line based on a parallel line (or single wire) considering a single wire over a ground plane that allows for designing a system with a characteristic impedance of $Z_0 = 150\ \Omega$. This parameter is fixed by selecting the distance from the plane to the center of the conductor $H = 15$ mm, the diameter of the conductor $d = 4.9$ mm and considering that it is surrounded by air [34–36]. By setting the ports' impedance to 150 Ω, it is possible to extract the cable ferrite's impedance under test without the characterization system influencing the results obtained. This value is a reference value adopted in different EMC standards to characterize and calibrate devices such as common mode absorption devices (CMADs) intended for measuring EMI disturbances in cables [11]. These fixtures are characterized using the through-reflect-line (TRL) calibration method based on measuring the S-parameters of CMADs, as described in CISPR 16-1-4 [11]. Therefore, this simulation model provides a reference system that can extract the impedance introduced in the conductor by the cable ferrite. The procedure performed to emulate the different studied gap cases ($g0$, $g1$, $g2$ and $g3$) is based on a parametric gap sweep. This technique makes it possible to determine the sleeve core's impedance when it is split into two parts and a specific gap is introduced. It is expected that this simulation model is able to provide the performance of the split samples from the original relative permeability (the values obtained for the non-split-core sample) by fixing the gaps described in Section 2. In the $g0$ case, the 0.01 mm distance value was introduced to differentiate it from the original non-split core.

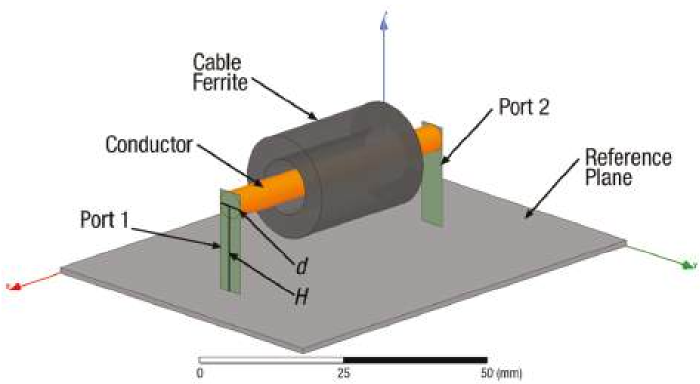

Figure 7. Cable ferrite simulation model.

4. Results and Discussion

This section focuses on analyzing the EMI suppression performance of the three described materials when they are split to be employed as snap ferrites. The results obtained from the experimental measurement setup and those provided by the simulation model are compared through each materials' impedance. This comparison is carried out to verify that the experimental results are not influenced by elements such as stability of the calibration setup in the high-frequency region and undesired high-frequency resonances caused by parasitic elements that could reduce the accuracy of the measurement. As is shown in Figure 8, the results are organized in three graphs, one per material: NiZn (a), MnZn (b) and NC (c)). These graphs represent the experimental (solid traces) and computed (dotted traces) impedance provided by the cable ferrite, considering the non-split situation and the split cases where the core is separated into two parts.

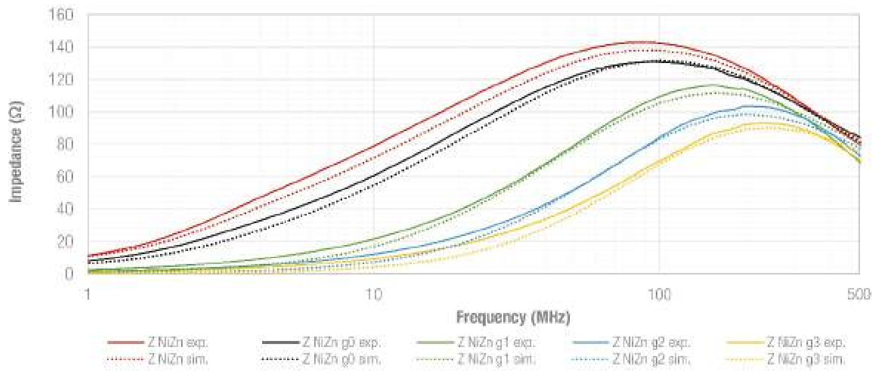

(**a**)

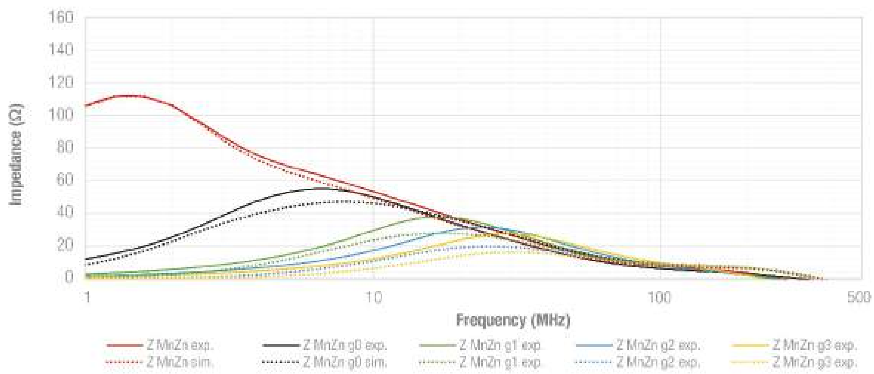

(**b**)

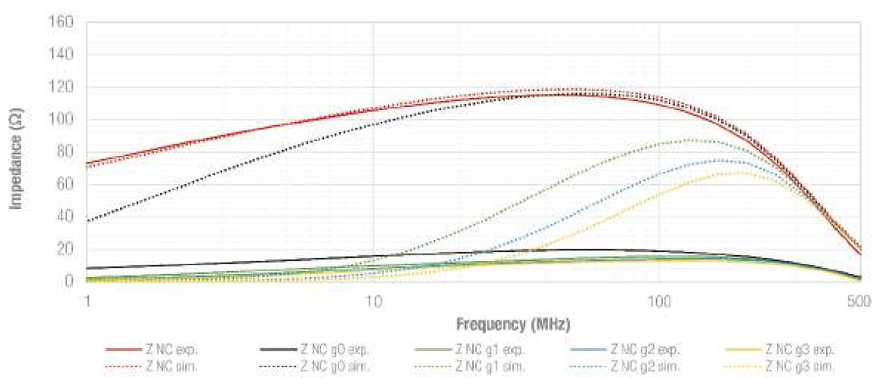

(**c**)

Figure 8. Comparison between experimental (solid traces) and simulated (dotted traces) impedance considering different gaps (non-split and split with gaps $g0$, $g1$, $g2$ and $g3$) for NiZn, MnZn and NC cable ferrites: (**a**) NiZn non-split (red trace) and split cases; (**b**) MnZn non-split (red trace) and split cases and (**c**) NC non-split (red trace) and split cases.

From the results obtained, the red traces of the graphs show the impedance provided by each non-split sample and it is possible to verify that the simulated and experimental results are a good match and, consequently, the data derived from the experimental setup can be considered in the whole frequency range analyzed. Consequently, a parametric gap sweep was performed in the simulation model by setting the four defined gap situations ($g0$, $g1$, $g2$ and $g3$) and keeping the same magnetic properties introduced to the non-split model. As can be observed, there is an excellent agreement between simulated and experimentally obtained results in NiZn and MnZn traces, whereas there is a significant difference in the NC case. This fact correlates with the conclusions obtained from the effective permeability data of the NC sample, shown in Section 2. Therefore, it is not possible to determine the NC sample's behavior when it is split and gapped by considering the non-split sample's magnetic properties. This is because the cut section's metallization is not able to maintain the high performance of the original NC sample. Then, the NC experimental results are considered to compare its performance with that provided by NiZn and MnZn samples.

Based on the results of three materials, halving the cable ferrite and using it as a snap ferrite ($g0$ situation) results in a shift of the resonance frequency at which the sample is able to provide the maximum attenuation ratio at the same time that the impedance is reduced. From the standpoint of the equivalent inductance and resistance series circuit of the sleeve core, the f_r is produced when the inductive component (X_L) turns into negative values and the resistive part (R) reaches the maximum value. Above this frequency value, the sleeve core's performance is degraded by the parasitic capacitive effect. Therefore, the f_r to higher frequencies shift results in extending the frequency range in which the sleeve core is effective to reduce EMI. This effect is lower for the NiZn cable ferrite since the f_r is increased from 86.7 MHz to 92.3 MHz, providing 142.9 Ω and 130.7 Ω, respectively. It represents a reduction of 8.5% in terms of impedance and an increase in the resonance frequency of f_r = 5.6%. Regarding the results obtained when a gap is introduced, an impedance of Z = 116.3 Ω (34.9% reduction) at f_r = 152.2 MHz for the $g1$ case, Z = 103.3 Ω (27.7% reduction) at f_r = 199.0 MHz for the $g2$ case and Z = 93.0 Ω (27.7% reduction) at f_r = 240.6 MHz for the $g3$ case. In the case of MnZn, it is possible to observe that the impedance traces are significantly modified when the sample is split since the original sample provides a maximum value of Z = 111.7 Ω at f_r = 1.4 MHz. The split-core with one part attached to the other ($g0$ case) provides Z = 55.0 Ω at f_r = 6.6 MHz, so the performance of the cable ferrite is reduced by about 50.8%. It is a relevant performance reduction compared to the attenuation ratio reduction of the NiZn sample. For the rest of the MnZn study cases where a higher gap is introduced ($g1$, $g2$ and $g3$), the impedance is mostly reduced (66.1%, 58.0% and 75.6%, respectively), compared to the NiZn results. Regarding the NC results, as described above, the simulated results obtained for the non-split sample match significantly with the experimental ones. Nevertheless, when the core is split, the simulated results overestimate the experimental data since the maximum impedance provided by the not split sample corresponds to 115.0 Ω, whose f_r = 45.5 MHz, whereas when it is split with both parts attached as closely as possible, the impedance is reduced by about 82.9%. When a specific gap is introduced ($g1$, $g2$ and $g3$ cases), the attenuation ratio produced is 86–89%.

The NC simulation model magnetic parameters were modified with the objective of obtaining a more realistic approximation response. Thereby, the model was simulated considering three different situations: non-split-core for the original sample, split-core without introducing a gap ($g0$) and split-core with the intended gap ($g1$, $g2$ and $g3$). Consequently, the magnetic parameters of the $g0$ situation correspond to the effective permeability measured with the split-core with both parts attached. The rest of gapped cases ($g1$, $g2$ and $g3$) were simulated by considering the measured effective permeability of the sample when the gap $g1$ is introduced. Figure 9 shows that the new simulated results match significantly with the experimental traces.

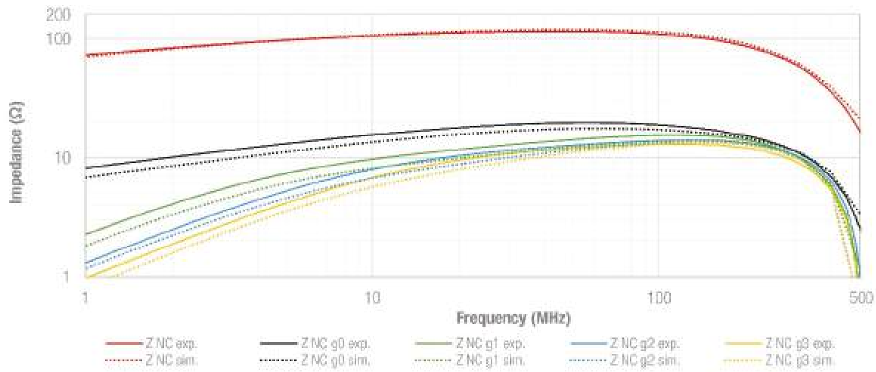

Figure 9. Comparison between experimental (solid traces) and new simulated (dotted traces) impedance, considering different gaps (non-split and split with gaps *g*0, *g*1, *g*2 and *g*3) for NC cable ferrites.

The comparison of the three different cable ferrites by separating them depending on the gap introduced is shown in Figure 10. As can be observed in Figure 10a, when cores are not split, they can be divided into three frequency ranges based on their performance. As expected, MnZn provides the larger impedance value in the low-frequency region, yielding the best performance up to 2.9 MHz. The NiZn cable ferrite offers higher impedance than MnZn and NC samples above 23.4 MHz, representing the most effective solution to reduce EMI disturbances in the high-frequency region. The NC core offers excellent performance in the medium-frequency region, providing a great impedance throughout the frequency band from 2.9 MHz to 23.4 MHz.

Additionally, the non-split NC core is able to yield a more stable response up to its maximum impedance value and it shows a better performance than ceramic cores to reduce EMI disturbances when they are distributed in a wideband frequency range (from the low-frequency region up to about 100 MHz). Figure 10b shows the impedance comparison when the cores are split into two parts and attached as closely as possible, emulating a snap ferrite's function. In this case, NC has significantly reduced its performance and MnZn provides the best performance up to 8.4 MHz. From this frequency value, NiZn yields the highest impedance value. In the rest of the analyzed gaps (*g*1, *g*2 and *g*3), the NiZn sample mainly represents the most interesting solution because MnZn and NC cable ferrites offer a lower impedance response. Thus, when a significant gap is introduced, the material with lower permeability is able to yield the best EMI attenuation.

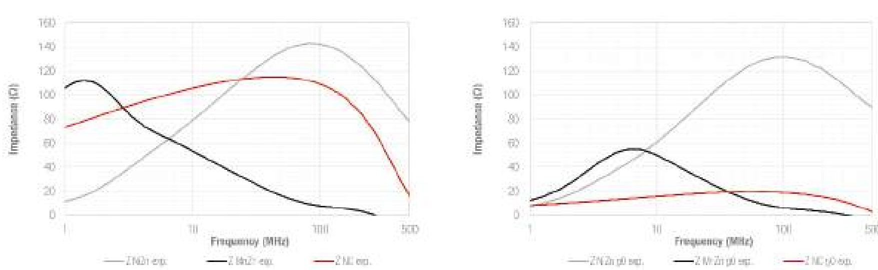

(**a**) (**b**)

Figure 10. *Cont.*

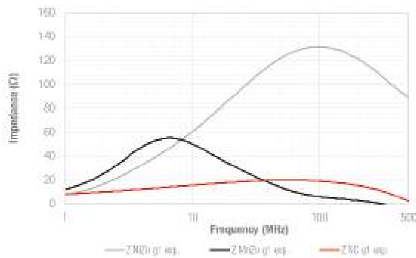

(**c**)

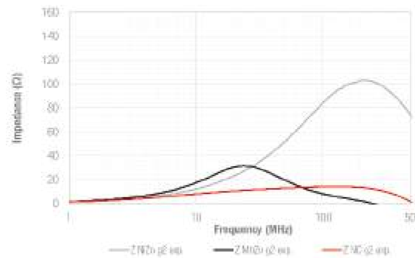

(**d**)

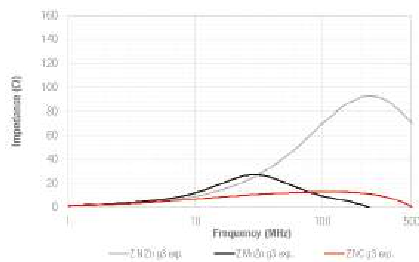

(**e**)

Figure 10. Comparison between the measured impedance of NiZn, MnZn and NC cable ferrites, considering five different gap cases: (**a**) NiZn, MnZn and NC non-split-cores; (**b**) NiZn, MnZn and NC $g0$ split-cores; (**c**) NiZn, MnZn and NC $g1$ split-cores; (**d**) NiZn, MnZn and NC $g2$ split-cores and (**e**) NiZn, MnZn and NC $g3$ split-cores.

Additionally, the non-split NC core is able to yield a more stable response up to its maximum impedance value and it shows a better performance than ceramic cores to reduce EMI disturbances when they are distributed in a wideband frequency range (from the low-frequency region up to about 100 MHz). Figure 10b shows the impedance comparison when the cores are split into two parts and attached as closely as possible, emulating a snap ferrite's function. In this case, NC has significantly reduced its performance and MnZn provides the best performance up to 8.4 MHz. From this frequency value, NiZn yields the highest impedance value. In the rest of the analyzed gaps ($g1$, $g2$ and $g3$), the NiZn sample mainly represents the most interesting solution because MnZn and NC cable ferrites offer a lower impedance response. Thus, when a significant gap is introduced, the material with lower permeability is able to yield the best EMI attenuation.

How splitting a cable ferrite into two parts, to be employed as a snap ferrite, modifies the impedance behavior was analyzed. Depending on the core's magnetic properties and structure, this involves a certain degradation of the EMI suppression ability. Nevertheless, splitting a cable ferrite could result in an advantage if the component is intended to encircle cables where DC currents are flowing. To further investigate this effect of the DC currents on the impedance, Figure 11 shows the impedance response of each of the three different materials studied when they are under DC bias conditions. Each material is represented in a separate graph and the response of the non-split sample is shown when different values of DC currents are injected (0 A, 0.5 A, 1 A, 2 A and 5 A), as described in Section 3. Figure 11a shows that the five traces have a similar trend, but the higher the DC current value, the lower the sample's impedance. This effect is observed from the lowest DC current value (0.5 A) and does not modify the impedance response significantly when compared to MnZn and NC results (Figure 11b,c, respectively). It is interesting how the resonance frequency is moved to higher frequencies when an increasing DC current is injected into the MnZn sample, specifically in the cases of 2 A and 5 A.

As regards NC behavior, it shows a significant impedance decrease in the low-frequency region and its performance is reduced more than that of ceramic cores when a DC bias flows through the cable.

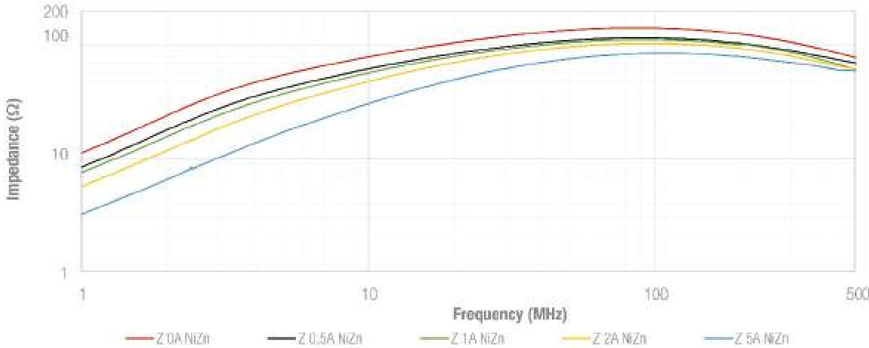

(**a**)

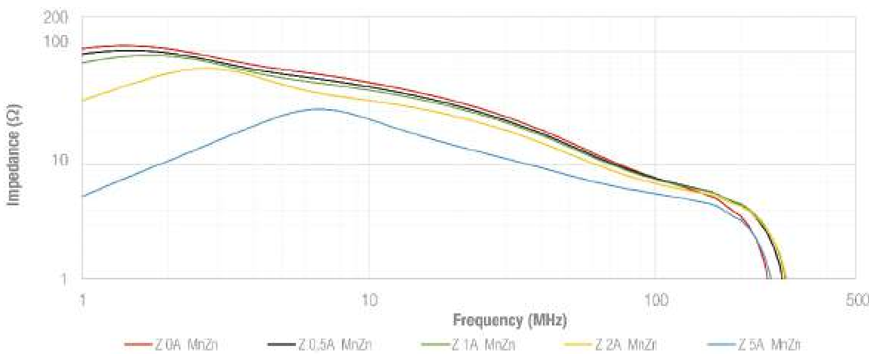

(**b**)

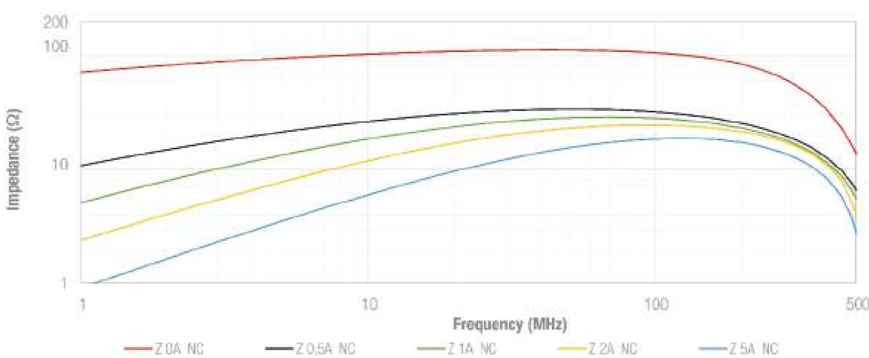

(**c**)

Figure 11. Impedance analysis considering different values of DC currents for the three different non-split samples: (**a**) NiZn; (**b**) MnZn and (**c**) NC.

The same analysis is repeated in Figure 12 for different gap values introduced in each of the samples. Thereby, the first row corresponds to the split NiZn samples, the second to the split MnZn samples and the third to the split NC samples. The left column shows the behavior of each material when the $g0$ gap is considered, and the right column shows the results obtained when $g1$ (dotted traces), $g2$ (short dashed traces) and $g3$ (long dashed traces) gaps are introduced. When the effect on the impedance response of splitting the samples to be attached without an intended gap is observed, the $g0$ traces show quite similar behavior in the three materials. NC traces have the same behavior over most of the frequency range, whereas NiZn traces show the same match between traces except for the 5 A case. In the case of MnZn, there is a difference between traces in the low-frequency region, producing a shift of the resonance frequency when DC currents higher than 0.5 A are applied. When the rest of the gaps are analyzed, the three materials have the same response when DC currents up to 5 A are injected. Moreover, from a certain frequency value, the materials' traces match independently of the DC current value and gap introduced.

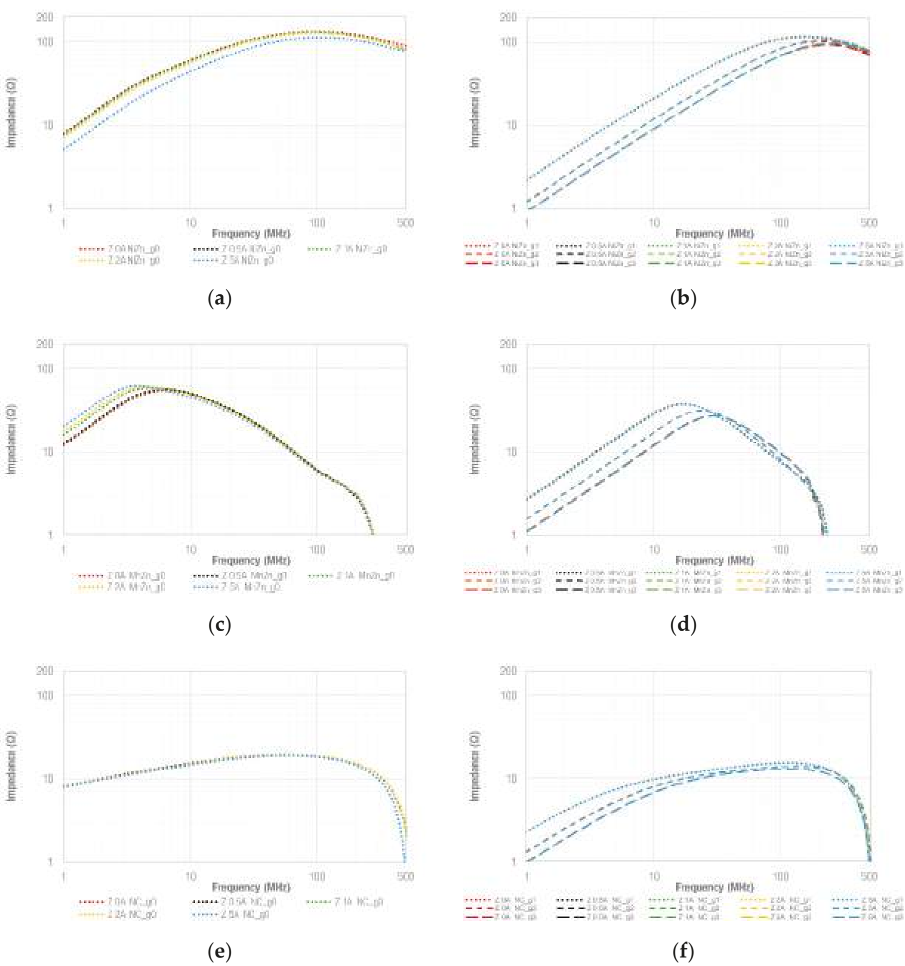

Figure 12. Impedance analysis considering different values of DC currents and gap conditions for the split samples: (**a**) NiZn $g0$ case; (**b**) NiZn $g1$, $g2$ and $g3$ cases; (**c**) MnZn $g0$ case; (**d**) MnZn $g1$, $g2$ and $g3$ cases; (**e**) NC $g0$ case and (**f**) NC $g1$, $g2$ and $g3$ cases.

5. Conclusions

The performance of the three different materials to build up ferrite cores was evaluated when they are split in order to determine their EMI suppression ability to be used as an openable core clamp. When the samples are not split, the analysis carried out in terms of impedance provided by each sample reveals that a ferrite core based on MnZn yields the best performance in the low-frequency region, whereas an NC core is most effective in the medium-frequency range and the NiZn sample provides larger impedance values in the high-frequency region.

When the samples are split and attached without introducing any gap ($g0$ situation), the impedance yielded by the NiZn sample is less degraded than the MnZn and NC impedances. In this study case, MnZn provides the best behavior in the low- and medium-frequency range, whereas the NC sample offers lower performance than expected due to its different internal structure. When larger gaps are considered, NiZn shows the most effective solution in terms of impedance. In this framework, other manufacturing procedures for NC snap-on cores should be investigated to obtain similar performance to what this solution can offer when it is not split.

The results obtained from the transmission line simulation model verify that the experimental results are in agreement and, thus, the data derived from the experimental measurement setup can be considered as an accurate approach in the frequency range studied (1–500 MHz). Consequently, the experimental and simulated results coincide with the conclusions obtained from effective relative permeability data. The material with more stable properties can provide higher performance and more predictable behavior than those with greater magnetic properties when the core is split. This conclusion is also applied when DC currents are flowing through the cable to be shielded since the NiZn solution shows better stability than the other materials.

Author Contributions: Conceptualization, A.S., J.V. and J.T.; Formal analysis, A.S., P.A.M., R.G.-O. and J.S.; Investigation, A.S., J.V., J.T., P.A.M. and A.A.; Methodology, A.S., P.A.M. and A.A.; Project administration, J.V., J.T., J.S., S.M. and A.G.; Supervision, J.V., J.T., J.S. and S.M.; Writing—original draft, A.S., J.T., P.A.M., J.P. and R.G.-O.; Writing—review and editing, J.V., J.T., P.A.M., A.A., J.P., R.G.-O., J.S., S.M. and A.G. All authors have read and agreed to the published version of the manuscript.

Funding: The APC was funded by the Universitat de València.

Acknowledgments: This work was supported by the Catedra Würth-EMC, a research collaboration agreement between the University of Valencia and Würth Elektronik eiSos GmbH & Co. KG.

Conflicts of Interest: The authors declare no conflict of interest. The founding sponsors had no role in the design of the study; in the collection, analyses, or interpretation of data; in the writing of the manuscript, and in the decision to publish the results.

References

1. González-Vizuete, P.; Domínguez-Palacios, C.; Bernal-Méndez, J.; Martín-Prats, M.A. Simple Setup for Measuring the Response to Differential Mode Noise of Common Mode Chokes. *Electronics* **2020**, *9*, 381. [CrossRef]
2. Kim, J.; Rotaru, M.D.; Baek, S.; Park, J.; Iyer, M.K.; Kim, J. Analysis of noise coupling from a power distribution network to signal traces in high-speed multilayer printed circuit boards. *IEEE Trans. Electromagn. Compat.* **2006**, *48*, 319–330. [CrossRef]
3. Crovetti, P.S.; Musolino, F. Interference of Spread-Spectrum EMI and Digital Data Links under Narrowband Resonant Coupling. *Electronics* **2020**, *9*, 60. [CrossRef]
4. Ott, H.W. *Electromagnetic Compatibility Engineering*; John Wiley & Sons: Hoboken, NJ, USA, 2009.
5. Yao, J.; Li, Y.; Zhao, H.; Wang, S. Design of CM Inductor Based on Core Loss for Radiated EMI Reduction in Power Converters. In Proceedings of the 2019 IEEE Applied Power Electronics Conference and Exposition (APEC), Anaheim, CA, USA, 17–21 March 2019; pp. 2673–2680. [CrossRef]
6. Kraftmakher, Y. Experiments on ferrimagnetism. *Eur. J. Phys.* **2012**, *34*, 213. [CrossRef]
7. Williams, T. *EMC for Product Designers*; Elsevier Science & Technology: Burlington, MA, USA, 2006; pp. 361–364. [CrossRef]
8. Goldman, A. *Modern Ferrite Technology*, 2nd ed.; Springer: Pittsburgh, PA, USA, 2006.

9. Bondarenko, N.; Shao, P.; Orlando, A.; Koledintseva, M.Y.; Beetner, D.G.; Berger, P. Prediction of common-mode current reduction using ferrites in systems with cable harnesses. In Proceedings of the 2012 IEEE International Symposium on Electromagnetic Compatibility, Pittsburgh, PA, USA, 6–10 August 2012; pp. 80–84. [CrossRef]
10. Paul, C.R. *Introduction to Electromagnetic Compatibility*, 2nd ed.; Wiley Interscience: Hoboken, NJ, USA, 2006.
11. Urabe, J.; Fujii, K.; Dowaki, Y.; Jito, Y.; Matsumoto, Y.; Sugiura, A. A Method for Measuring the Characteristics of an EMI Suppression Ferrite Core. *IEEE Trans. Electromagn. Compat.* **2006**, *48*, 774–780. [CrossRef]
12. Tong, X.C. *Advanced Materials for Electromagnetic Interference Shielding*, 1st ed.; CRC Press: Boca Raton, FL, USA, 2009.
13. Orlando, A.; Koledintseva, M.Y.; Beetner, D.G.; Shao, P.; Berger, P. A lumped-element circuit model of ferrite chokes. In Proceedings of the 2010 IEEE International Symposium on Electromagnetic Compatibility, Fort Lauderdale, FL, USA, 25–30 July 2010; pp. 754–759. [CrossRef]
14. Van den Bossche, A.; Valchev, V.C. *Inductors and Transformers for Power Electronics*; CRC Press: Boca Raton, FL, USA, 2005.
15. Kazimierczuk, M.K. *High-Frequency Magnetic Components*; John Wiley & Sons: Hoboken, NJ, USA, 2009.
16. Weinschrott, A. New measurement method for high frequency cable mounted ferrites. In Proceedings of the 2005 International Symposium on Electromagnetic Compatibility, Chicago, IL, USA, 8–12 August 2005; pp. 312–314. [CrossRef]
17. Suarez, A.; Victoria, J.; Alcarria, A.; Torres, J.; Martinez, P.A.; Martos, J.; Soret, J.; Garcia-Olcina, R.; Muetsch, S. Characterization of Different Cable Ferrite Materials to Reduce the Electromagnetic Noise in the 2–150 kHz Frequency Range. *Materials* **2018**, *11*, 174. [CrossRef] [PubMed]
18. Damnjanovi, M.; Stojanovi, G.; Živanov, L.; Desnica, V. Comparison of different structures of ferrite EMI suppressors. *Microelectron. Int.* **2006**, *23*, 42–48. [CrossRef]
19. Suarez, A.; Victoria, J.; Martinez, P.A.; Alcarria, A.; Torres, J.; Molina, I. Analysis of different Sleeve Ferrite Cores Performance according to their Dimensions. In Proceedings of the 2019 International Symposium on Electromagnetic Compatibility-EMC EUROPE, Barcelona, Spain, 2–6 September 2019; pp. 88–93. [CrossRef]
20. Suarez, A.; Victoria, J.; Torres, J.; Martinez, P.A.; Alcarria, A.; Martos, J.; Garcia-Olcina, R.; Soret, J.; Muetsch, S.; Gerfer, A. Effectiveness Assessment of a Nanocrystalline Sleeve Ferrite Core Compared with Ceramic Cores for Reducing Conducted EMI. *Electronics* **2019**, *8*, 800. [CrossRef]
21. Cullity, B.D.; Graham, C.D. *Introduction to Magnetic Materials*; Wiley: Hoboken, NJ, USA, 2009.
22. Kącki, M.; Rylko, M.S.; Hayes, J.G.; Sullivan, C.R. Magnetic material selection for EMI filters. In Proceedings of the 2017 IEEE Energy Conversion Congress and Exposition (ECCE), Cincinnati, OH, USA, 1–5 October 2017; pp. 2350–2356. [CrossRef]
23. Cuellar, C. HF Characterization and Modeling of Magnetic Materials for the Passive Components Used in EMI Filters. Ph.D. Thesis, University of Lille, Lille, France, 2013.
24. Sixdenier, F.; Morand, J.; Salvado, A.; Bergogne, D. Statistical study of nanocrystalline alloy cut cores from two different manufacturers. *IEEE Trans. Magn.* **2014**, *50*, 1–4. [CrossRef]
25. Brander, T.; Gerfer, A.; Rall, B.; Zenkner, H. *Trilogy of Magnetics: Design Guide for EMI Filter Design, SMP & RF Circuits*, 4th ed.; Swiridoff Verlag: Künzelsau, Germany, 2010.
26. Roc'h, A.; Leferink, F. Nanocrystalline core material for high-performance common mode inductors. *IEEE Trans. Electromagn. Compat.* **2012**, *54*, 785–791. [CrossRef]
27. Thierry, W.; Thierry, S.; Benoît, V.; Dominique, G. Strong volume reduction of common mode choke for RFI filters with the help of nanocrystalline cores design and experiments. *J. Magn. Magn. Mater.* **2006**, *304*, 847–849. [CrossRef]
28. Brockman, F.G.; Dowling, P.H.; Steneck, W.G. Dimensional effects resulting from a high dielectric constant found in a ferromagnetic ferrite. *Phys. Rev.* **1950**, *77*, 85–93. [CrossRef]
29. Ponomarenko, N. Study of Frequency and Microstructure Dependencies of Magnetic Losses of Ferrite Materials and Components. Ph.D. Thesis, Riga Technical University, Riga, Latvia, 2014.
30. Fiorillo, F. *Measurement and Characterization of Magnetic Materials*; Elsevier: Amsterdam, The Netherlands, 2004.
31. Bhuiyan, R.H.; Dougal, R.A.; Ali, M. A miniature energy harvesting device for wireless sensors in electric power system. *IEEE Sens. J.* **2010**, *10*, 1249–1258. [CrossRef]
32. McLyman, C.W.T. *Transformer and Inductor Design Handbook*; Dekker: New York, NY, USA, 1988.

33. Keysight 16200B External DC Bias Adapter Operation and Service Manual. Available online: http://literature.cdn.keysight.com/litweb/pdf/16200B.pdf (accessed on 28 September 2020).
34. Chang, K. *Handbook of Microwave and Optical Components, Fiber and Electro-Optical Components*; Wiley: Hoboken, NJ, USA, 1991.
35. International Telephone, & Telegraph Corporation. *Reference Data for Radio Engineers*; Howard W. Sams and Company: Indianapolis, IN, USA, 1968.
36. Haase, H.; Nitsch, J.; Steinmetz, T. Transmission-line super theory: A new approach to an effective calculation of electromagnetic interactions. *URSI Radio Sci. Bull.* **2003**, *307*, 33–60. [CrossRef]

electronics

Article

Simple Setup for Measuring the Response to Differential Mode Noise of Common Mode Chokes

Pablo González-Vizuete [1], Carlos Domínguez-Palacios [1], Joaquín Bernal-Méndez [2,*] and María A. Martín-Prats [1]

1 Dpto.Ingeniería Electrónica, Escuela Técnica Superior de Ingeniería, Universidad de Sevilla, 41092 Seville, Spain; pgonzalez17@us.es (P.G.-V.); cardompal@alum.us.es (C.D.-P.); mmprats@us.es (M.A.M.-P.)

2 Dpto.Física Aplicada III, Escuela Técnica Superior de Ingeniería, Universidad de Sevilla, 41092 Seville, Spain

* Correspondence: jbmendez@us.es; Tel.: +34-954-486191

Received: 15 January 2020; Accepted: 21 February 2020; Published: 25 February 2020

Abstract: This work presents a technique to measure the attenuation of differential mode noise provided by common mode chokes. The proposed setup is a simpler alternative to the balanced setup commonly employed to that end, and its main advantage is that it avoids the use of auxiliary circuits (baluns). We make use of a modal analysis of a high-frequency circuit model of the common mode choke to identify the natural modes actually excited both in the standard balanced setup and in the simpler alternative setup proposed here. This analysis demonstrates that both setups are equivalent at low frequencies and makes it possible to identify the key differences between them at high frequencies. To analyze the scope and interest of the proposed measurement technique we have measured several commercial common mode chokes and we have thoroughly studied the sensitivity of the measurements taken with the proposed setup to electric and magnetic couplings. We have found that the proposed setup can be useful for quick assessment of the attenuation provided by a common mode choke for differential mode noise in a frequency range that encompasses the frequencies where most electromagnetic compatibility regulations impose limits to the conducted emissions of electronic equipment.

Keywords: electromagnetic compatibility; power electronics EMC; EMI mitigation techniques; EMI filter design and optimization

1. Introduction

The control of conducted emissions of electronic devices is an increasingly critical topic due to the trends toward the use of higher switching frequencies in power converters [1]. To mitigate conducted emissions, power line electromagnetic interference (EMI) filters are commonly used. However, at frequencies ranging from several hundred kilohertz to a few tens of megahertz the performance of EMI filters is typically undermined by parasitic effects such as parasitic parallel capacitances between windings in inductors and parasitic series inductances of capacitors [2–5]. Therefore, characterizing the response of these components at those high frequencies is becoming increasingly important to reduce design time, cost and size of the filter.

Common mode chokes (CMCs), made up of a pair of tightly coupled inductors, are key components of EMI filters primarily intended to limit common mode (CM) noise [2,5]. However, CMCs typically exhibit an inductive response to differential mode (DM) noise (leakage inductance) which has a significant impact on the attenuation that the EMI filter provides to differential mode (DM) noise [2]. The reason is that the leakage inductance provides a 40 dB/dec roll-off above its frequency of resonance with capacitors that typically are placed between power lines in the EMI filter to attenuate DM noise (Cx capacitors). This resonance typically occurs at tens or a few hundreds of kilohertz. At even higher frequencies (up to tens or a few hundreds of megahertz) leakage inductance no longer determines the DM attenuation of the CMC, which is instead governed by parasitic capacitive effects [6]. In this context, a method to directly measure and evaluate the actual frequency-dependent insertion loss provided by a CMC for DM noise would be very useful to estimate its suitability for a particular EMI filter.

A first option available to analyze the DM response of a CMC is to perform a full characterization of the device in a broad frequency range, obtaining an equivalent circuit which would make it possible to estimate the response of the CMC to a DM excitation by simulation as an additional task to perform after the characterization process is complete. Within this category of full characterization methods, several methods have been reported to obtain equivalent circuits for transformers and coupled coils [7–11]. Some of these methods have been particularized or directly conceived to be applied to CMCs [6,12,13]. The main drawback of these methods is that they often involve impedance measurements for different connections of the CMC and that they require a post-processing of the obtained data. Moreover, compensation is often required to perform these impedance measurements. Therefore, these methods are not the most appropriate option when a quick assessment of the DM response of a CMC is required.

A more straightforward alternative for evaluating the attenuation of DM signals provided by a CMC is to directly measure it. Techniques to measure the response of a four-port components such as CMCs to CM and DM excitations are adequately described in different standards, mostly based upon CISPR recommendations [14]. However, while measuring the CM attenuation of a CMC is fairly simple, the measurement of the insertion loss for a DM excitation requires the use of either a four-port vector network analyzer (VNA) or a balanced circuit that includes 180° splitters (baluns) [15]. Four-port VNAs are expensive and consequently may well not to be available. Baluns are much more affordable and common devices. However, its effect should be carefully assessed and taken into account because they may introduce some losses and, more importantly, they have a limited bandwidth [15]. Consequently, the use of these ancillary circuits complicates the setup and the measurement process. In this context, the availability of a simpler measurement technique that allows evaluation of the DM attenuation provided by a CMC would greatly facilitate the processes of design and test of EMI filters.

In response to that need, in this work we present a simple unbalanced measurement setup that can be used to quickly evaluate the attenuation that a CMC provides against DM noise. We perform a thorough analysis of this unbalanced setup which shows that possible sensibility of the unbalanced setup to external couplings might be a source of measurement errors. To determine whether this represent a problem in practice we systematically compare measurements performed with the unbalanced setup with those provided by the alternative balanced setup with the aim of clearly determining the validity, scope and limitations of the proposed setup.

This paper is organized as follows: in Section 2 we present a general analysis of the problem. In Section 2.1 we make use of a modal analysis of a high-frequency circuit model of a CMC considered to be a four-port network to obtain closed-form expressions for the transmission coefficients (and their corresponding frequencies of resonance) corresponding to both the standard balanced setup and the proposed unbalanced setup that can be used to assess the DM response of a CMC. The aim is to analyze the differences between both setups, and to identify the approximations under which both measurement methods provide similar results. Sections 2.2 and 2.3 present analysis of the effect of electric and magnetic couplings on the measurements performed with the balanced and unbalanced setups, with a focus on situations where these effects may arise in practice. In Section 3 we present results for several commercial CMCs to validate the analysis presented in Section 2. Also, in that section the actual sensitivity of both balanced and unbalanced setups to the effects of electric and magnetic couplings are experimentally studied. Finally, conclusions and a discussion about the scope of the method are provided in Section 4.

2. Analysis

Figure 1 shows a simplified representation of a CMC along with a lumped-element circuit model of the CMC. As shown in Figure 1a, a CMC is made up of two equal magnetically coupled windings. In [16] it has been demonstrated that a CMC can be conveniently modeled in a sufficiently broad frequency range by using a lumped-elements circuit with two blocks, each one containing two perfectly coupled inductances as shown in Figure 1b. The first block in that figure (CM block) only affects the CM noise, while the second block (DM block) contains inductors with opposite (perfect) coupling and therefore it only affects DM signals. In that circuit model parasitic intra-winding capacitances (C_t) and inter-winding capacitances (C_w) have been added to account for the response of the CMC throughout a sufficiently broad frequency range [16,17]. Also, losses within the magnetic material are accounted for in that model by resistors R_{CM} and R_{DM} placed in parallel with the coupled inductors. Finally, capacitances to ground, C_g, have been included in the circuit model to consider possible electric coupling to nearby metallic surfaces, e.g., the ground plane on a printed circuit board (PCB).

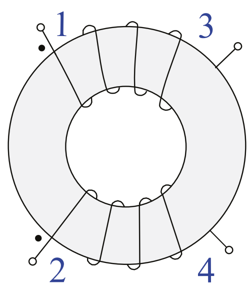

(**a**) Common mode choke.

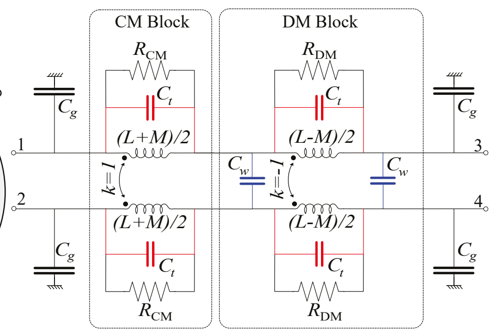

(**b**) Equivalent circuit of the CMC with CM and DM blocks.

Figure 1. Representation and circuit model of a common mode choke made up of two equal coupled windings with self-inductance L and mutual inductance M.

2.1. Modal Analysis of the CMC

The circuit in Figure 1b can be considered to be a four-port network and it can be characterized by a 4×4 admittance matrix $[Y]$. A modal analysis can be carried out by calculating the voltage eigenvectors (modes) that diagonalize $[Y]$, as explained in [16]. In that work, it has been shown that this analysis yields four independent (uncoupled) modes, which are referred to as C, V, H and D modes. In general, for a given excitation of the CMC, its response is always made up of a superposition of the responses of one or more of those natural modes. The equivalent circuits of these four modes are represented in Figure 2. In that figure we also represent the normalized excitation at the four ports of the CMC that corresponds to each mode. Please note that CM and DM excitation of the CMC appear as H and D natural modes of the equivalent circuit of the CMC (Figure 2c,d). As for the other two modes, mode C in Figure 2a corresponds to applying a common voltage to the four ports of the CMC, while mode V in Figure 2b is obtained by applying a difference of voltage between the two windings of the CMC.

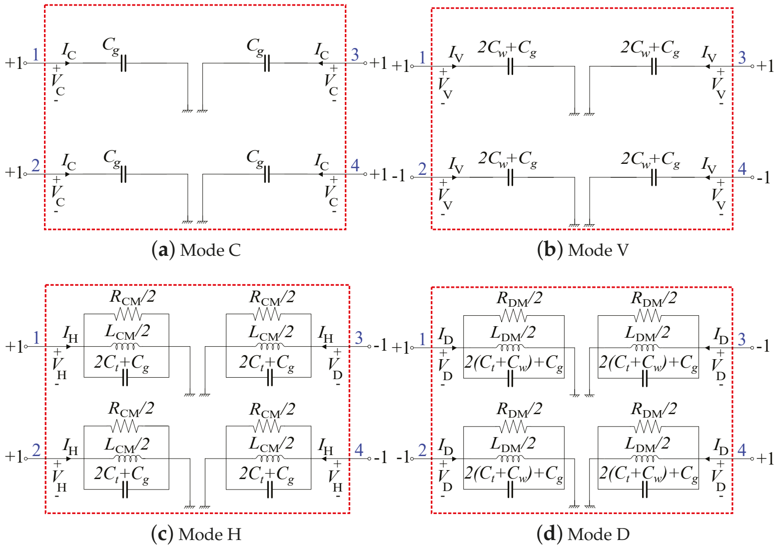

Figure 2. Equivalent circuits of the modes obtained for the high-frequency circuit of the CMC in Figure 1b. Normalized voltages at the four terminals of the CMC are indicated for each mode.

In Figure 2 it can be seen that the admittances of the four modes of the CMC are either a capacitive admittance (modes C and V) or the admittance of a resistor, an inductor and a capacitor connected in parallel (parallel RLC circuit), where the inductive component is proportional to $L_{\mathrm{CM}} = L + M$ for the CM (H mode) and to $L_{\mathrm{DM}} = L - M$ (the leakage inductance) for the DM (D mode). The admittances of the four modes of the CMC can be written as follows:

$$Y_{\mathrm{C}} = j\omega C_g. \tag{1}$$

$$Y_{\mathrm{V}} = j\omega(2C_w + C_g). \tag{2}$$

$$Y_{\mathrm{H}} = j\omega(2C_t + C_g) + \frac{2}{j\omega L_{\mathrm{CM}}} + \frac{2}{R_{\mathrm{CM}}}. \tag{3}$$

$$Y_{\mathrm{D}} = j\omega(2C_t + 2C_w + C_g) + \frac{2}{j\omega L_{\mathrm{DM}}} + \frac{2}{R_{\mathrm{DM}}}. \tag{4}$$

The modal analysis outlined above allows performance of a very efficient analysis of the measurement setups that can be used to characterize the DM response of CMCs. The idea is to express the transmission coefficients corresponding to these measurement setups in terms of the admittances of the natural modes of the CMC to determine to what extent those setups actually excite a pure DM (as intended) and also to assess the impact on measurements of the parasitic effects incorporated to the equivalent circuit of the CMC.

The measurement setup usually required to characterize the DM response of a CMC is schematically shown in Figure 3a [14]. We will refer here to this setup as DM setup. The DM setup requires the use of two baluns (or 180° dividers) to convert the excitation of the output port of the measurement device into a DM signal and to measure the transmitted DM signal at the input port. In other words, the DM setup permits direct measurement of the S_{DD21} term of the Mixed-Mode S-Parameter Matrix of the CMC seen as a four-port network [18]. This S_{DD21} S-Parameter physically represents the DM response of the CMC to a DM excitation, or equivalently the transmission coefficient (or inverse of the insertion loss) of the DM. For this reason, we will refer here to this S-parameter as S_{21}^{DM}. Table 1 provides S_{21}^{DM} as a function of the admittances of the natural modes of the CMC.

Since only Y_D and Y_V appear in the expression of S_{21}^{DM}, we can conclude that only D (DM) and V modes of the CMC are excited in the DM setup. Also, from that expression it is possible to obtain the frequency of resonance of the CMC in that setup in terms of the elements of the circuit model of the CMC in Figure 1b. This frequency of resonance, f_{DM}, is also given in Table 1 (Since in practice $R_{CM}, R_{DM} \gg R = 50\,\Omega$ the frequency of resonance can be calculated by taking $R_{CM} \to \infty$ and $R_{DM} \to \infty$ in S_{21}^{DM} and imposing $S_{21}^{DM} = 0$). At frequencies below f_{DM} the response of the CMC is dominated by the inductive part of Y_D, i.e., L_{DM}. Above f_{DM} the CMC behaves capacitively and the magnitude of S_{21}^{DM} increases with frequency. Please note that since f_{DM} does not depend on C_g, an electric coupling to ground will not alter the frequency of resonance of S_{21}^{DM}.

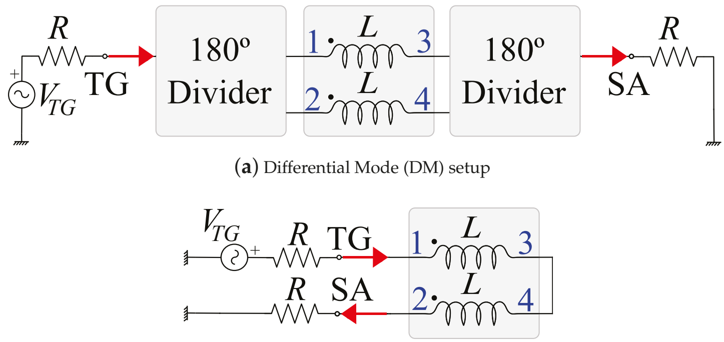

(**a**) Differential Mode (DM) setup

(**b**) Unbalanced Differential Mode (UDM) setup

Figure 3. Balanced and unbalanced setups for measuring transmission coefficients conveying information about the attenuation provided by a CMC for a differential mode excitation. Measurements can be performed with a spectrum analyzer (SA) with tracking generator (TG) or a VNA.

Table 1. Transmission coefficients and frequencies of resonance for a CMC measured in the setups of Figure 3, where $Y_{OC} = Y_H Y_D/(Y_H + Y_D)$. Approximated expressions assume $C_g \ll C_t, C_w$ and $Y_C \ll Y_V, Y_H, Y_D$.

Setup	Transmission Coefficient	Frequencies of Resonance
DM	$S_{21}^{DM} = \frac{RY_D}{2+RY_D} - \frac{RY_V}{2+RY_V}$	$f_{DM} = \frac{1/2\pi}{\sqrt{C_t L_{DM}}}$
UDM	$S_{21}^{UDM} \approx \frac{R(Y_D+Y_V)}{2+R(Y_D+Y_V)}$	$f_{UDM} \approx \frac{1/2\pi}{\sqrt{(C_t+2C_w)L_{DM}}}$
OC	$S_{21}^{OC} \approx \frac{2RY_{OC}}{2RY_{OC}+1}$	$f_{OC} \approx \frac{1/2\pi}{\sqrt{(C_t+C_w)L_{DM}}}$

As an alternative to the DM setup, in Figure 3b we propose a simpler unbalanced setup (UDM setup) which dispenses with baluns and which at the same time is also able to provide information about the DM response of the CMC. The UDM setup in Figure 3b, like the DM setup in Figure 3a, involves the measurement of a transmission coefficient instead of the measurement of impedances of the CMC. This allows for avoiding additional measurements to account for the effect of cables and/or test fixtures (compensation measurements) [19]. To compare the UDM setup with the DM setup, it is useful to obtain also the transmission coefficient of the UDM setup (S_{21}^{UDM}) in terms of the admittances of the natural modes of the CMC. An analysis of the circuit in Figure 3b with the circuit model of the CMC in Figure 1b leads to:

$$S_{21}^{UDM} = \frac{R(Y_p - 4Y_s)}{(2 + Y_p R)(1 + 2Y_s R)}. \tag{5}$$

where $Y_p = Y_D + Y_V + 2Y_C$ and $Y_s = Y_C Y_H/(Y_C + Y_H)$. This analysis shows that unlike the DM setup which only excites D and V modes, the UDM setup excites the four natural modes of the CMC. In principle, this makes an important difference between DM and UDM setups. However, it can be easily shown that if measurements are performed avoiding the presence of nearby conducting surfaces, the response of the UDM setup becomes quite similar to that of the DM setup. In particular, only D and V modes are significantly excited in the UDM setup. To demonstrate this, suppose that capacitances to ground are negligible compared with the rest of the capacitances of the circuit model in Figure 1b ($C_g \ll C_t, C_w$). In that case, the expressions for the modal impedances in Equations (1)–(4) allow us to assume that $Y_\mathrm{C} \ll Y_\mathrm{V}, Y_\mathrm{H}, Y_\mathrm{D}$. Consequently, we can approximate in (5) $Y_s \approx Y_\mathrm{C} \ll Y_p \approx Y_\mathrm{D} + Y_\mathrm{V}$. In that case, a simpler approximation of the expression of S_{21}^{UDM} in (5) can be obtained:

$$S_{21}^{\mathrm{UDM}} \approx \frac{R(Y_\mathrm{D} + Y_\mathrm{V})}{2 + R(Y_\mathrm{D} + Y_\mathrm{V})}. \quad (6)$$

This expression is included in Table 1 along with that of S_{21}^{DM}. The frequency of resonance of S_{21}^{UDM} in Equation (6) is also provided in that table as f_{UDM}. When comparing S_{21}^{UDM} with S_{21}^{DM}, it can be noticed that both expressions depend only on Y_D and Y_V. Moreover, because Y_V in Equation (2) is a capacitive admittance related to the inter-winding capacitance, it is expected that at low frequencies $Y_\mathrm{V} \ll Y_\mathrm{D}$ and therefore $S_{21}^{\mathrm{UDM}} \approx S_{21}^{\mathrm{DM}} \approx RY_\mathrm{D}/(2 + RY_\mathrm{D})$. In other words, at low frequencies (i.e., well below resonance) the response of the CMC is expected to be dominated by L_{DM} and to be the same for the DM setup as for the UDM setup, with currents flowing inside the CMC in a purely differential mode in both cases.

Summing up, the previous analysis demonstrates that provided that coupling with nearby metallic surfaces is negligible, $S_{21}^{\mathrm{UDM}} \approx S_{21}^{\mathrm{DM}}$ at low frequencies. This is an important result because it allows us to conclude that at these low frequencies the UDM setup can be used as a simpler alternative to the DM setup to quickly characterize the DM response of a CMC. However, the analysis presented here also demonstrates that at high frequencies some differences should be expected between S_{21}^{DM} and S_{21}^{UDM}. This will be experimentally checked in Section 3. Before that the next subsections complete the theoretical analysis by analyzing the effect of electric and magnetic couplings of the CMC with nearby conducting surfaces on measurements performed with DM and UDM setups.

2.2. Effect of Electric Coupling to Metallic Surfaces

In the previous section we have seen that the transmission coefficient S_{21}^{DM} of the balanced DM setup is inherently independent of Y_C (see Table 1) and that electric couplings are not expected to significantly affect measurements carried out with the DM setup. By contrast, external electric couplings will affect measurements with the UDM setup unless S_{21}^{UDM} can be approximated by Equation (6). That approximation can be safely applied whenever no metallic surface is allowed near the CMC when measuring. However, there are situations where this cannot be ensured. This may occur for example when measuring a CMC which is mounted on a PCB with a return plane. This PCB can be for example the PCB of the EMI filter or a PCB employed to measure the CMC as a four-port terminal, as required in many cases in the normative [14].

Even for a CMC mounted on a PCB, the return plane is usually sufficiently far from the windings of the CMC as to make it reasonable to disregard a direct electric coupling of the CMC to the return plane with respect to the internal couplings given by the inter-windings and intra-windings capacitances ($C_g \ll C_t, C_w$ in Figure 1b). However, the effects on the DM and UDM measurements of the microstrip traces of the PCB employed to lead the signals to the four pins of the CMC should be assessed. As for the DM measurements, it can be easily demonstrated that if the characteristic impedance of these signal traces of the PCB are equal to the input and output impedances of the measuring device (usually 50 Ω), those traces will only introduce a phase shift in the transmission coefficient of the DM setup, but they will not alter the magnitude of S_{21}^{DM} [19]. However, the situation is different for the UDM setup.

A schematic of the situation presented for the UDM setup can be seen in Figure 4. That figure represents a CMC connected in the UDM setup, and it includes transmission line models for the interconnecting cables (e.g., coaxial cables), which are labelled as $\mathrm{TL_C}$ lines, and for the signal traces of the PCB (typically microstrip lines), which are labelled as $\mathrm{TL_T}$ lines. In principle, $\mathrm{TL_T}$ traces leading to terminals 1 and 3 of the CMC are not an issue. In fact, provided that they have the same 50 Ω characteristic impedance as TL_C lines, those traces will only introduce a phase shift in the transmission coefficient [19]. However, TL_T lines attached at terminals 2 and 4 of the CMC create an asymmetric electric coupling of the CMC to ground whose effect is not negligible, as we will show here. To demonstrate that, consider the situation represented in Figure 4, where terminals 2 and 4 of the CMC are directly short-circuited to achieve an UDM configuration that circumvents the two TL_T lines attached to those terminals. Considering lengths of TL_T lines in the order or centimeters, they will be electrically short at the frequencies of interest and, consequently, these open-circuited lines can be modeled as capacitances [20]. The two parasitic capacitances C_r included in Figure 4 account for this effect. Since these C_r capacitances correspond to the total capacitance of the trace lines, their values are typically in the order of units or tens of picofarads [20]. Consequently, C_r capacitances cannot be disregarded by comparison with typical parasitic capacitances of the CMC, which are of the same order of magnitude.

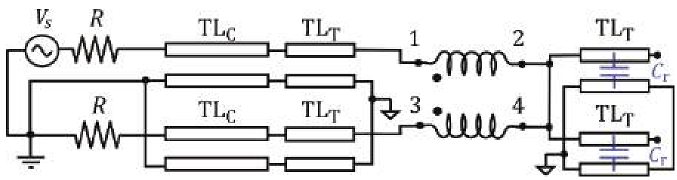

Figure 4. Schematic of a CMC mounted on a grounded PCB connected in UDM setup. Transmission lines labelled as TL_C stand for the interconnecting cables. Transmission lines labelled as TL_T represent the signal traces of the PCB. The signal traces terminated as open-circuits at terminals 2 and 4 are supposed to be electrically short and thereby modeled as two capacitances C_r to ground.

To investigate the impact on the transmission coefficient measured with the UDM setup of the capacitances C_r that must be included in the schematic of the UDM setup in Figure 4, we have calculated the transmission coefficient of that circuit by circuit analysis. We have used the circuit model of the CMC in Figure 1 with $Y_C = 0$, but we have included the effect of C_r capacitors as two external admittances $Y_R = j\omega C_r$ connected to terminals 2 and 4 of the CMC. In this way, we have obtained the following modified S_{21}^{UDM} coefficient in terms of the admittances of the modes of the CMC:

$$S_{21}^{\mathrm{UDM}'} = \frac{R(Y_D + Y_V)}{2 + R(Y_D + Y_V)} - \frac{RY_{HR}}{2 + RY_{HR}}. \tag{7}$$

where $Y_{HR} = Y_H Y_R/(Y_H + Y_R)$. It is very interesting to note that the only difference between $S_{21}^{\mathrm{UDM}'}$ in (7) and S_{21}^{UDM} in Equation (6) is the presence of the second additive term in (7). This term is zero if $Y_R = 0$ (C_r=0), as expected. Therefore, Equation (7) reveals that the effect of considering the electric coupling given by C_r is to excite an additional mode of the CMC (H mode), whose admittance Y_H acts in series with that of C_r. A very good approximation for the frequency of resonance of $S_{21}^{\mathrm{UDM}'}$ in Equation (7) can be obtained if we consider that this frequency must be near that of S_{21}^{UDM}, i.e., it must be found at frequencies where $\omega C_t \approx 1/|\omega L_{DM}|$. Because in practical CMCs we have $L_{CM} \gg L_{DM}$, we have $1/|\omega L_{CM}| \ll \omega C_t$ and therefore Y_H in Equation (3) can be approximated as $Y_H \approx j\omega C_t$. With this approximation the frequency of resonance of $S_{21}^{\mathrm{UDM}'}$ in Equation (7) can be expressed as:

$$f'_{\mathrm{UDM}} = \frac{1/2\pi}{\sqrt{(C_t + 2C_w - \frac{C_r C_t}{C_r + C_t})L_{DM}}}. \tag{8}$$

By comparing this frequency of resonance with f_{UDM} given in Table 1 we conclude that the main effect of C_r in the transmission coefficient of the UDM setup is to slightly increase its frequency of resonance.

From the previous analysis we conclude that by contrast with DM setup, the UDM setup is sensitive to the presence of electrical couplings (capacitive effects) caused by the presence of nearby metallic grounded structures such as a ground plane on a PCB, and that this effect can be noticeable at high frequencies.

An interesting question that arises in this point is whether in the UDM setup this effect can be avoided by isolating the return plane of the PCB with respect to ground in the measurement setup. This situation is shown in Figure 5, which represents an alternative implementation of the UDM setup for a CMC mounted on a PCB where the active conductors of the TL_C lines (cables) are directly connected to the terminals of the CMC, while circumventing the TL_T lines connected to terminals 1 and 3, thus isolating the return plane of the PCB from the ground of the measurement setup. In that case, the four electrically short open-circuited TL_T lines connected at each terminal will introduce four parasitic capacitances C_r at each terminal of the CMC.

These capacitances connected to a star point (the isolated return plane) can be transformed into its triangle equivalent, as shown in figure Figure 6. That figure shows that the effect of the capacitances C_r is to increase the C_w parasitic capacitance of the CMC by an amount $\Delta C_w = C_r/4$, and to increase C_t by an amount $\Delta C_t = C_r/2$. This should cause a decrease in the frequency of resonance of S_{21}^{UDM} with respect to the case with no return plane. Therefore, the UDM Setup will still be sensitive to the presence of the return plane of the PCB. This will be experimentally verified in Section 3.

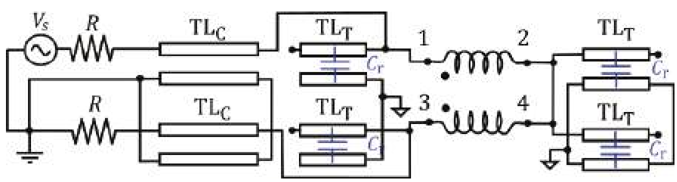

Figure 5. Equivalent circuit of the UDM setup for a CMC mounted on a PCB with an ungrounded return plane. Transmission lines labelled as TL_C stand for the interconnecting cables. Transmission lines labelled as TL_T represent the signal traces of the PCB. Since all the signal traces are terminated as open-circuits and they are supposed to be electrically short, they are actually modeled as capacitances C_r to ground.

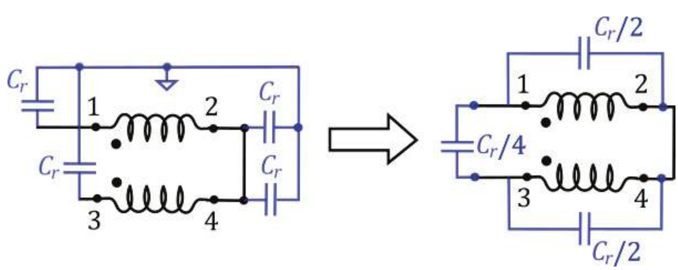

Figure 6. Star to triangle conversion for the parasitic capacitances C_r that appear at the four terminals of the CMC in the circuit of Figure 5.

2.3. *Effect of Magnetic Coupling to Metallic Surfaces*

Another effect that can alter the response of a CMC excited by a DM signal is a magnetic coupling of the CMC with nearby metallic surfaces. The root cause of this effect is that, unlike CM currents, DM currents in a CMC create a magnetic field which closes its field lines outside the core of the CMC [21,22]. Therefore, this magnetic field can interact with nearby metallic surfaces such as for instance, the metallic enclosure usually employed for housing and shielding of EMI filters. Even though metallic enclosures are usually constructed with non-magnetic metals, a magnetic coupling might still appear due to eddy currents induced in those conducting surfaces by the time-varying stray magnetic field of the CMC. The effect of these eddy currents is to partially counteract the magnetic fields created by the CMC outside its core, thus causing a decrease of the leakage inductance L_{DM} of the CMC [22,23]. This change of L_{DM} can equally affect measurements performed with the DM or the UDM setups. The actual impact of this effect in practical cases will be investigated in Section 3.3.

3. Results

The analysis presented in the previous section suggests that in principle it is possible to use the UDM setup in Figure 3b to measure the DM response of a CMC. However, since we have shown that electric or magnetic couplings may affect the response of the CMC, the impact of these effects on measurements performed with the UDM setup must be assessed to clearly determine the scope and limitations of this method of measurement by comparison with standard DM measurement. To this end, we present in this section experimental results for several commercial CMCs in different setups. These measurements have been carried out by using a Rhode&Schwarz ZND VNA. However, note that measurements of the magnitude of a transmission coefficient can be alternatively performed by using a spectrum analyzer with tracking generator.

3.1. Analysis of the Response of a Standalone CMC

To validate the analysis presented in Section 2 we have measured the response of the CMCs listed in Table 2 in the DM and UDM setups shown in Figure 3. Also, we have used an alternative setup, referred to as Open-Circuit (OC) setup, which is shown in Figure 7. This setup was proposed in [16] to characterize CMCs. The main difference between OC setup and UDM is that since the OC setup is actually used for obtaining a complete circuit model of the CMC and it is not conceived as a measurement method to characterize its DM response, in the OC setup both the CM (H) and DM (D) modes of the CMC are simultaneously excited. An expression for the transmission coefficient of the CMC in the OC setup, S_{21}^{OC} in terms of Y_{H} and Y_{D} is given in Table 1 [16]. From this expression, it can be easily demonstrated that S_{21}^{OC} always presents two frequencies of resonance: one related to L_{CM} and another one at a higher frequency associated with L_{DM} which is given in Table 1 as f_{OC}. As a consequence of this double resonance, the OC setup does not allow quick measurement of the response of a CMC to a purely DM signal throughout the entire range of frequencies of interest. However, since the expression and physical meaning of f_{OC} has been previously studied in [16], we will use it here to validate our analysis of the UDM setup as explained below.

Table 2. Parameters extracted for the equivalent circuit of Figure 1b for several commercial common mode chokes.

Manufacturer and Part Number	L (mH)	L_{CM} (mH)	L_{DM} (uH)	C_w (pF)	C_t (pF)	R_{CM}(kΩ)	R_{DM}(kΩ)
WÜRTH ELEKT. 744824622	2.2	4.94	4.7	4.2	6.8	17.2	6.5
WÜRTH ELEKT. 744824310	10	26.7	33.6	4.7	18.3	118	16.6
WÜRTH ELEKT. 744824220	20	54.1	57.6	10.7	20.2	203	22.2
WÜRTH ELEKT. 7448011008	8.0	6.90	6.5	0.86	2.7	22.1	8.1
MURATA PLA10AN2230R4D2B	22	71.3	173	1.8	2.9	73.9	33.0
KEMET SC-02-30G	3.0	7.40	5.8	1.4	2.8	34.3	16.7
KEMET SCF20-05-1100	11	13.4	5.1	8.6	7.2	15.4	7.9

By comparing the frequencies of resonance in Table 1 it is apparent that for a given CMC we must have $f_{\mathrm{UDM}} < f_{\mathrm{OC}} < f_{\mathrm{DM}}$. We will use here this fact to verify the accuracy of our circuit model and to check the expressions for the transmission coefficients of the DM and UDM setups, S_{21}^{DM} and S_{21}^{UDM}, presented in Table 1.

Figure 8 shows $|S_{21}^{\mathrm{DM}}|$, $|S_{21}^{\mathrm{UDM}}|$ and $|S_{21}^{\mathrm{OC}}|$ measured for the CMC listed as WÜRTH ELEKTRONIK 744824622 (2.2 mH) in Table 2. It can be observed that each one of these curves present a resonance dip related to differential excitation of the CMC, as expected. Also, note that these frequencies of resonance are different for the three setups. In fact, resonance occurs first for the UDM setup, then for the OC setup (second resonance) and finally, for the DM, i.e., $f_{UDM} < f_{OC} < f_{DM}$. These results are consistent with our previous analysis. Similar results are obtained for all the CMCs in Table 2. An additional example is represented in Figure 9 for another CMC, identified in the caption of the figure and listed in Table 2.

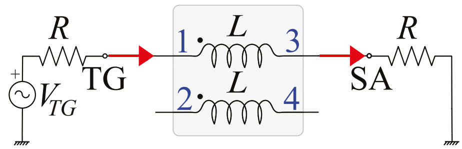

Figure 7. Open-circuit (OC) setup proposed in [16] for characterizing CMCs.

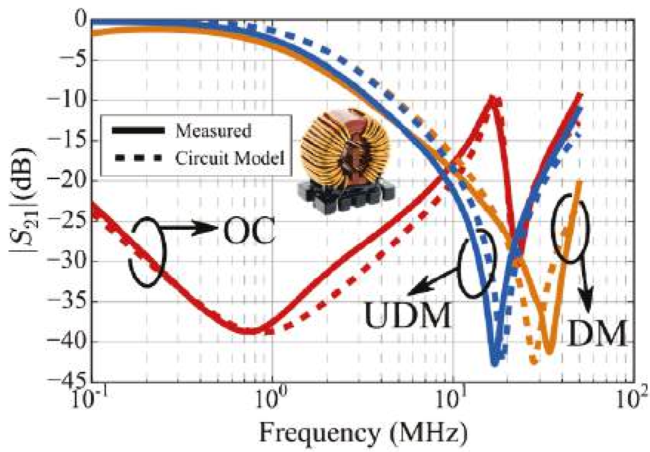

Figure 8. Magnitude $|S_{21}|$ for the CMC listed as Würth Elecktronik 744824622 (2.2 mH) in Table 2, using the setups in Figures 3 and 7.

To further ensure consistency of the measured curves with our theoretical analysis, we have used an advanced search algorithm based upon genetic algorithms (GA) [24] to find a set of values for the components of the circuit in Figure 1b that allow us to simultaneously fit the measured S_{21}^{OC} and S_{21}^{DM} curves. Parameters obtained for all the CMCs analyzed here are given in Table 2. Then, we have used these circuit parameters to calculate $|S_{21}^{UDM}|$ using the expression given in Table 1. These curves are represented in Figures 8 and 9 as dashed lines, and labelled as calculated results. A good agreement between measured and calculated results can be observed in these graphs. Similar results are obtained for all the CMCs in Table 2. This permits us to ensure that the high-frequency circuit model in Figure 1b is reasonably accurate within the range of frequencies where most EMC regulations impose limits to conducted emissions [25–27].

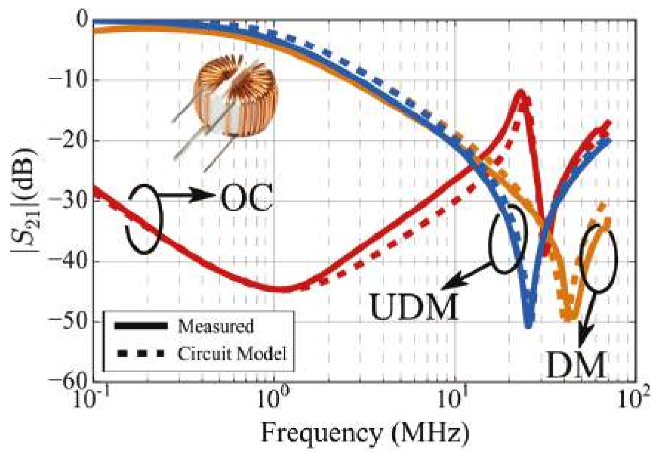

Figure 9. Magnitude $|S_{21}|$ for the CMC listed as KEMET SC-02-30G (3 mH) in Table 2, using the setups in Figures 3 and 7.

It is worth pointing out that in the measurements performed in this section external magnetic or electric couplings have been carefully avoided by keeping the CMC under test far from metallic surfaces (a distance greater than the size of the CMC is typically enough). This is important because the expression for S_{21}^{OC} in Table 1, such as that of S_{21}^{UDM} Equation (6), assumes that parasitic capacitances to ground can be disregarded, i.e., $Y_{\mathrm{C}} \ll Y_{\mathrm{V}}, Y_{\mathrm{H}}, Y_{\mathrm{D}}$. The effect on measurements of electric coupling with nearby metallic surfaces will be analyzed in the next subsection.

3.2. Effect of Capacitive Couplings in a PCB

The analysis presented in Section 2.2 shows that when a CMC is mounted on a PCB (a situation that may easily arise in practice), the parasitic capacitances introduced by the traces connected to the terminals of the CMC might alter the measurements of S_{21}^{UDM}, thus rendering misleading results if the aim is to characterize the CMC as a standalone component. In this section, we will analyze the actual impact of this effect by comparing measured S_{21}^{UDM} for an isolated CMC with results obtained when the CMC is mounted on a PCB representative of those usually employed to fabricate EMI filters.

Figure 10 shows a CMC mounted on a PCB fabricated with a 1.5 mm-thick FR4 substrate. Signal traces (not visible in Figure 10 because the CMC is mounted on the side of the return plane) are 4 mm-width×60 mm-long strips connecting the CMC pins to the BNC connectors. These signal traces, along with the BNC connectors, add an extra parasitic capacitance between the four ports of the CMC and the return plane (RP). We have measured this parasitic capacitance, obtaining a value of $C_r = 17.5\,\mathrm{pF}$.

As a first step, we have checked that the fact that the CMC is mounted on a PCB has a negligible effect on the measurements of $|S_{21}^{\mathrm{DM}}|$, as expected from the analysis in Section 2. This robustness of S_{21}^{DM} measurements against external electric couplings comes from the balanced nature of this setup, and represents an advantage of this measurement technique. On the contrary, and according to the analysis in Section 2.2, the measure of $|S_{21}^{\mathrm{UDM}}|$ could be affected by the parasitic capacitances appearing at the terminals of the CMC when it is mounted on a PCB with a RP. To study the actual impact of this effect in a practical case, Figure 11 shows $|S_{21}^{\mathrm{UDM}}|$ measured for the CMC listed as WÜRTH ELEKTRONIK 744824220 (20 mH) in Table 2 in three different situations: when CMC is isolated (no magnetic or electric coupling with nearby conducting surfaces), when CMC is mounted in the PCB but the RP is not grounded (schematic in Figure 4) and finally, when the CMC is mounted in the PCB and the RP is grounded (schematic in Figure 5). Curves in Figure 11 show that the response of the CMC at low frequencies (well below resonance) is the same for these three situations. However, Figure 11 also reveals that at high frequencies there exists a shift in the frequency of resonance of S_{21}^{UDM}. Compared to the isolated case, the frequency of resonance is slightly lower when the RP is not grounded and slightly higher when the RP is grounded. These results are consistent with the analysis presented in Section 2.2. We have obtained similar results for all the CMCs in Table 2.

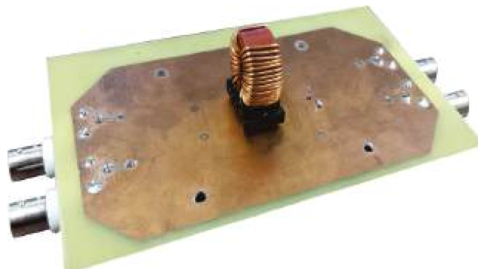

Figure 10. A 2.2 mH CMC, listed in Table 2 as WÜRTH ELEKTRONIK 744824622, mounted on a PCB fabricated to check the impact on $|S_{21}^{\mathrm{UDM}}|$ of the capacitive coupling of the signal traces to the return plane.

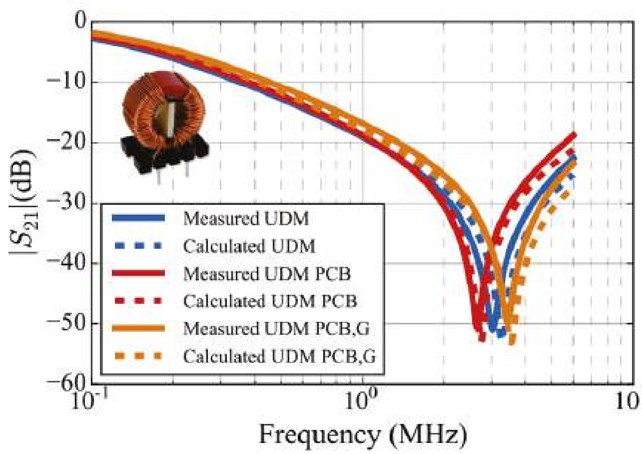

Figure 11. Measured and calculated $|S_{21}^{\mathrm{UDM}}|$ curves for the CMC listed as WÜRTH ELEKTRONIK 744824220 (20 mH) in Table 2. We compare curves for three cases: standalone CMC, CMC mounted on a PCB with a floating return plane and CMC mounted on a PCB whose return plane is grounded (G label).

To analyze this effect in more detail, and also to check the explanation provided inSsection 2.2, we have measured the frequencies of resonance of three different CMCs (among those in Table 2) when measured in the three different situations described above. In Table 3 we compare the frequency of resonance measured with the CMC isolated with that obtained when the CMC is placed on a PCB with an ungrounded RP. Those results show that the effect of the presence of the isolated RP is to decrease the frequency of resonance of S_{21}^{UDM} by an amount that goes from 10% to 20%. Table 3 also includes for each CMC the frequency of resonance calculated by using the expression of f_{UDM} given in Table 1, where C_t and C_w have been modified to $C_t' = C_t + C_r/2$ and $C_w' = C_w + C_r/4$ in accordance with the results of the analysis presented in Section 2.2. The rest of the parameters of the model of each CMC have been taken from Table 2. Results in Table 3 show that the calculated frequency of resonance agrees reasonably well with the measured one, with typical discrepancies around 5%. This allows us to conclude that the decrease of the frequency of resonance of S_{21}^{UDM} observed when the CMC is mounted on a PCB with an isolated RP is mainly caused by the parasitic capacitances between the traces and the isolated return plane of the PCB.

Table 3. Measured frequencies of resonance of S_{21}^{UDM} for three CMCs when isolated and when mounted on a PCB with an ungrounded return plane. Also, calculated f_{UDM} for the latter case.

	f_{UDM} (MHz)		
	CMC Isolated	**CMC on Ungrounded PCB**	
CMC Part Number	**Measured**	**Measured**	**Calculated**
WE 744824622	16.9	13.6	12.8
WE 744824310	4.77	4.30	4.07
WE 744824220	3.02	2.65	2.74

Table 4 compares the frequency of resonance of S_{21}^{UDM} measured when the CMC is isolated with that measured when the CMC is mounted on a grounded PCB for the same three CMCs listed in Table 3. Results show that the grounded RP causes the frequency of resonance to increase in all the cases, as expected. This increase is up to 35% for the WE 2.2 mH CMC. Frequencies of resonance f'_{UDM} calculated by using (8) are also included in Table 4. The good agreement found in general between calculated and measured results confirms that the shift of the frequency of resonance of S_{21}^{UDM} is caused by the presence of the grounded RP and that this shift can be approximately predicted by using Equation (8).

Table 4. Measured frequencies of resonance of S_{21}^{UDM} for three CMCs when isolated and when mounted on a PCB with a grounded return plane. Also, calculated f_{UDM} for the latter case.

	f_{UDM} (MHz)		
	CMC Isolated	**CMC on Grounded PCB**	
CMC Part Number	**Measured**	**Measured**	**Calculated**
WE 744824622	16.9	21.7	22.8
WE 744824310	4.77	5.63	5.64
WE 744824220	3.02	3.40	3.72

Summing up, results in this section show that when measured in the UDM setup, the capacitance between the signal traces and the RP of the PCB can modify the response of the CMC at high frequencies. Therefore, when accurate results are required, measuring a CMC mounted on a PCB with the UDM setup should be avoided unless the effect of the parasitic capacitances of the signal traces to the RP is accounted for.

Another interesting conclusion that can be obtained from these results refers to the impact of magnetic coupling. Figure 11 shows that at low frequencies the response of the standalone CMC coincides with those measured when the CMC is mounted on a PCB. Therefore, we can conclude that at low frequencies (i.e., well below resonance), the RP has no significant effect on L_{DM}. This is because the RP is not sufficiently close to the windings of the CMC. Situations where magnetic coupling with external metallic surfaces may have an impact on the measurements of S_{21}^{UDM} (and S_{21}^{DM}) will be analyzed in the next subsection.

3.3. *Effect of Magnetic Coupling to Nearby Conducting Surfaces*

The aim of this section is to study the sensitivity of the measurements of S_{21}^{DM} and S_{21}^{UDM} to the effect of magnetic coupling to nearby conducting surfaces (CS). We have verified for all the CMCs in Table 2 that the measurements of S_{21}^{DM} and S_{21}^{UDM} are altered by the presence of an isolated (i.e., not necessarily grounded) copper plate placed very close to the top of the CMC. This situation is representative of that that may arise in practice when the CMC of an EMI filter is placed very close to the metallic enclosure of the filter. We have verified that this effect is noticeable only if the CS is very close to the windings (in general, less than 1 mm apart). In fact, we have checked that the effect of magnetic coupling is very weak when the CS is placed beneath (instead of on top) of the CMC, because in this case the leads and the plastic structure that typically supports the CMC keep the CS sufficiently far from the windings of the CMC to prevent a significant magnetic coupling. This is consistent with results for CMCs mounted on a PCB presented in the previous section, where we have seen that the effect of the return plane of the PCB on the leakage inductance of the CMC, L_{DM}, is negligible.

As an example to show the effect of magnetic coupling on the DM response of CMCs, we represent in Figure 12 the measured $|S_{21}^{\mathrm{UDM}}|$ and $|S_{21}^{\mathrm{DM}}|$ with and without the presence of a CS for the 10 mH CMC listed as WÜRTH ELEKTRONIK 744824310 in Table 2. The CS employed to induce magnetic coupling in this experiment is a 10cm-side square copper plate which has been placed on top of the CMC, only separated by a paper film whose thickness is approximately 0.1 mm. Figure 12 shows that the effect of the CS is to slightly increase both $|S_{21}^{\mathrm{DM}}|$ and $|S_{21}^{\mathrm{UDM}}|$ at low frequencies and also to increase their respective frequencies of resonance. These effects can be explained by a decrease of L_{DM}. To demonstrate this, we have included in Figure 12 the $|S_{21}^{\mathrm{DM}}|$ and $|S_{21}^{\mathrm{UDM}}|$ curves calculated by using the equivalent circuit of Figure 1b with the parameters extracted in the previous sections (Table 2) and also the same curves obtained after conveniently decreasing L_{DM}. Those calculated results agree very well with measurements. In general, the effect of the magnetic coupling created by CS placed very close to a CMC is to decrease the leakage inductance of the CMC by an amount between a 20% and a 30%. Detailed quantitative results are provided in Table 5 for the CMC in Figure 12 and two additional CMCs among those listed in Table 2. Table 5 compares for each CMC the inductance L_{DM} calculated without the presence of a CS with the reduced inductance (referred to as $L_{\mathrm{DM}}^{\mathrm{CS}}$) that should be used to match the S_{21}^{DM} and S_{21}^{UDM} curves in the presence of a CS. It is interesting to highlight that the same reduced inductance $L_{\mathrm{DM}}^{\mathrm{CS}}$ can be used to account for the effect of the magnetic coupling for both the DM and UDM measurements, as should be expected.

The main conclusion that can be drawn from the experiment described in this section is that a closely placed CS can alter the DM response of a CMC by decreasing its leakage inductance. Moreover, this effect can equally affect measurements in both the DM and the UDM setups. This implies that independently of the setup, magnetic coupling should be avoided (by keeping the CMC sufficiently far apart from metallic surfaces) to prevent an inaccurate characterization of the DM response of a CMC as a standalone component. Alternatively, in case the actual metallic enclosure where the CMC is going to be placed is available, it would be possible to determine its effect on the leakage inductance of a CMC by measuring it in the UDM setup with the CMC placed in the same relative position with respect to the metallic enclosure that it is intended to occupy in practice.

Table 5. L_{DM} for different CMCs with and without the effect of a nearby conducting surface.

CMC Part Number	L_{DM} (μH)	$L_{\mathrm{DM}}^{\mathrm{CS}}$ (μH)
WE 744824622	4.73	3.38
WE 744824310	33.6	27.0
WE 744824220	58.2	44.2

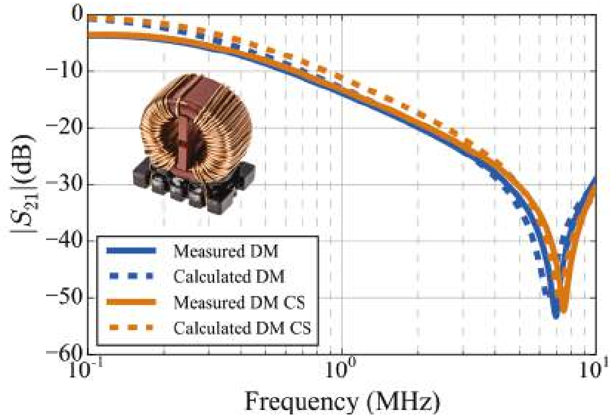

(**a**)

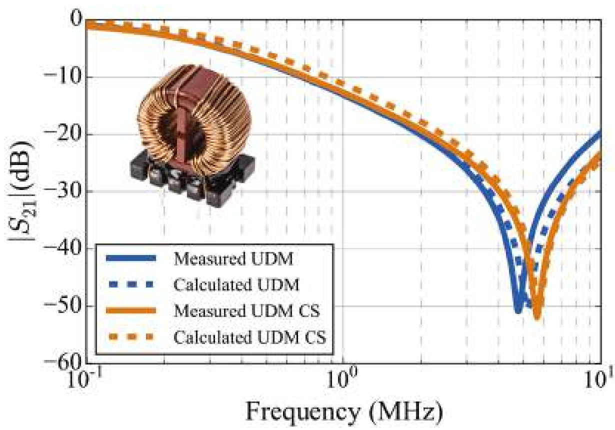

(**b**)

Figure 12. Measured and calculated $|S_{21}^{\rm DM}|$ (**a**) and $|S_{21}^{\rm UDM}|$ (**b**) for the CMC listed as WÜRTH ELEKTRONIK 744824310 (10 mH) in Table 2, whose picture is inserted in the figures. The CS acronym used in the legends indicates results corresponding to the case where a conducting surface is placed near the CMC.

From results in Figure 12, it is also interesting to note that below approximately 3 MHz, $|S_{21}^{\rm DM}|$ curves coincide very well with $|S_{21}^{\rm UDM}|$ ones. This is consistent with the discussion presented in Section 2.1, where we demonstrate that at low frequencies the response of a CMC is mainly determined by $L_{\rm DM}$ and that is expected that $S_{21}^{\rm DM} \approx S_{21}^{\rm UDM}$. This confirms that in the range of frequencies where the CMC behaves inductively, the UDM setup can be effectively used to predict the DM insertion loss of a CMC.

It is also worth pointing out that the curves for $|S_{21}^{\rm DM}|$ in Figure 12a show a slight attenuation at very low frequencies (between 100 kHz and 200 kHz) when compared with $|S_{21}^{\rm UDM}|$ curves in Figure 12b. This effect can also be observed in measured $|S_{21}^{\rm DM}|$ represented in Figures 8 and 9. We have verified that this is caused by a decrease in the performance of the baluns that we have employed in these measurements, due to its limited bandwidth (We have used baluns constructed with commercial wide-band 1:1 transformers Coilcraft WB2010-1 [28].). Although this problem could be solved by using baluns with a wider bandwidth or by performing a careful calibration, we point it out here to highlight an inherent shortcoming of the DM setup, namely its dependence on ancillary circuitry whose effect on the measurements has to be carefully taken into account.

4. Discussion and Conclusions

This work presented a thorough analysis of a measurement setup, referred to as UDM setup, which can be used to readily measure the response of a CMC to DM signals throughout the frequency range where most EMC regulations impose limits to conducted emissions. The UDM setup is conceived as a simpler and faster alternative to balanced setups, which require ancillary circuits (baluns), and to the use of sophisticated equipment such as four-port VNAs.

We have presented a detailed analysis of the UDM setup based on a modal analysis of a high-frequency circuit model of the CMC. This modal analysis has allowed us to obtain analytical expressions for the transmission coefficients of the CMC in terms of the admittances of the natural modes of the CMC, both for the DM and UDM setups. From these expressions it has been possible to determine the modes actually excited in the CMC in each setup which has permitted us to analyze the effect of parasitic effects on each setup and to identify the conditions that ensure similar responses of the CMC for the DM and UDM measurement setups.

The analysis and experimental results presented in this work provide a deep understanding on the differences and similarities between both techniques of measurement. This has allowed us to demonstrate that the DM setups is inherently immune to (symmetric) external electric coupling while the UDM is sensitive to this effect. By contrast, we have verified that both DM and UDM setups are equally sensitive to magnetic coupling of the CMC to nearby conducting surfaces because this effect modifies the leakage inductance of the CMC. We have quantified the impact of these effects in some practical cases and we have found that provided that the presence of nearby conducting surfaces is avoided or carefully accounted for, the proposed UDM setup can be used to assess the response of a CMC to DM noise within a range of frequencies of practical interest.

Summing up, the main contribution of the present work is to provide a deep understanding on the actual scope and limitations of a simple technique that can be used to measure the attenuation provided by a common mode choke to differential mode signals. This is important because the simplicity of the proposed measurement technique makes it very appropriate for quick assessment of the suitability of a common mode choke for a particular application. In fact, the quick assessing of the impedance and DM attenuation of a CMC provided by the proposed measurement approach facilitates the tasks of ensuring stability and compliance of electronic equipment with conducted emissions limits imposed by EMC regulations.

Author Contributions: Conceptualization, J.B.-M. and M.A.M.-P.; methodology, J.B.-M.; software, C.D.-P.; validation, P.G.-V. and C.D.-P.; formal analysis, P.G.-V. and C.D.-P.; investigation, P.G.-V. and C.D.-P.; resources, M.A.M.-P.; data curation, C.D.-P.; writing–original draft preparation, J.B.-M. and P.G.-V.; writing–review and editing, J.B.-M. and M.A.M.-P.; visualization, C.D.-P. and P.G.-V.; supervision, M.A.M.-P. and J.B.-M.; project administration, M.A.M.-P.; funding acquisition, J.B.-M. and M.A.M.-P. All authors have read and agreed to the published version of the manuscript.

Funding: This work has been supported by the Spanish Ministerio de Economía y Competitividad (project TEC2014-54097-R) and by H2020-EU.3.4.5.6. SCOPUS project (Grant agreement ID: 831942).

Conflicts of Interest: The authors declare no conflict of interest.

References

1. Kovacevic, I.F.; Friedli, T.; Muesing, A.M.; Kolar, J.W. 3-D electromagnetic modeling of EMI input filters. *IEEE Trans. Ind. Electron.* **2014**, *61*, 231–242. [CrossRef]
2. Paul, C.R. *Introduction to Electromagnetic Compatibility*; John Wiley and Sons: Hoboken, NJ, USA, 2006.
3. Wang, S.; Lee, F.; Chen, D.; Odendaal, W. Effects of parasitic parameters on EMI filter performance. *IEEE Trans. Power Electron.* **2004**, *19*, 869–877. [CrossRef]
4. Wang, S.; Chen, R.; Van Wyk, J.D.; Lee, F.C.; Odendaal, W.G. Developing parasitic cancellation technologies to improve EMI filter performance for switching mode power supplies. *IEEE Trans. Electromagn. Compat.* **2005**, *47*, 921–929. [CrossRef]

5. Chiu, H.J.; Pan, T.F.; Yao, C.J.; Lo, Y.K. Automatic EMI measurement and filter design system for telecom power supplies. *IEEE Trans. Instrum. Meas.* **2007**, *56*, 2254–2261. [CrossRef]
6. Kotny, J.L.; Margueron, X.; Idir, N. High-frequency model of the coupled inductors used in EMI filters. *IEEE Trans. Power Electron.* **2012**, *27*, 2805–2812. [CrossRef]
7. Baccigalupi, A.; Daponte, P.; Grimaldi, D. On a circuit theory approach to evaluate the stray capacitances of two coupled inductors. *IEEE Trans. Instrum. Meas.* **1994**, *43*, 774–776. [CrossRef]
8. Cogitore, B.; Keradec, J.; Barbaroux, J. The two-winding transformer: An experimental method to obtain a wide frequency range equivalent circuit. *IEEE Trans. Instrum. Meas.* **1994**, *43*, 364–371. [CrossRef]
9. Schellmanns, A.; Berrouche, K.; Keradec, J.P. Multiwinding transformers: A successive refinement method to characterize a general equivalent circuit. *IEEE Trans. Instrum. Meas.* **1998**, *47*, 1316–1321. [CrossRef]
10. Margueron, X.; Keradec, J.P. Identifying the magnetic part of the equivalent circuit of n-winding transformers. *IEEE Trans. Instrum. Meas.* **2007**, *56*, 146–152. [CrossRef]
11. Besri, A.; Chazal, H.; Keradec, J.P. Capacitive behavior of HF power transformers: global approach to draw robust equivalent circuits and experimental characterization. In Proceedings of the 2009 IEEE Instrumentation and Measurement Technology Conference, Singapore, 5–7 May 2009; pp. 1262–1267.
12. Roc'h, A.; Bergsma, H.; Zhao, D.; Ferreira, B.; Leferink, F. A new behavioural model for performance evaluation of common mode chokes. In Proceedings of the 2007 18th International Zurich Symposium on Electromagnetic Compatibility, Munich, Germany, 24–28 September 2007; pp. 501–504.
13. Stevanovic, I.; Skibin, S.; Masti, M.; Laitinen, M. Behavioral modeling of chokes for EMI simulations in power electronics. *IEEE Trans. Power Electron.* **2013**, *28*, 695–705. [CrossRef]
14. CISPR 17:2011. Methods of measurement of the suppression characteristics of passive EMC filtering devices. 2011.
15. Kyyrä, J.; Kostov, K. Insertion loss in terms of four-port network parameters. *IET Sci. Meas. Technol.* **2009**, *3*, 208–216.
16. Dominguez-Palacios, C.; Bernal-Méndez, J.; Martin Prats, M.A. Characterization of common mode chokes at high frequencies with simple measurements. *IEEE Trans. Power Electron.* **2018**, *33*, 3975–3987. [CrossRef]
17. den Bossche, A.V.; Valchev, V.C. *Inductors and Transformers for Power Electronics*; CRC Press: Boca Raton, FL, USA, 2005.
18. Bockelman, D.E.; Eisenstadt, W.R. Combined differential and common-mode scattering parameters: Theory and simulation. *IEEE Trans. Microw. Theory Technol.* **1995**, *43*, 1530–1539. [CrossRef]
19. Bernal-Méndez, J.; Freire, M.J.; Martin Prats, M.A. Overcoming the effect of test fixtures on the measurement of parasitics of capacitors and inductors. *IEEE Trans. Power Electron.* **2020**, *35*, 15–19. [CrossRef]
20. Pozar, D. *Microwave Engineering*; Wiley&Son: Hoboken, NJ, USA, 2011.
21. Nave, M. *Power Line Filter Design for Switched-Mode Power Supplies*; Van Nostrand Reinhold: New York, NY, USA, 1991.
22. Dominguez Palacios, C.; Gonzalez Vizuete, P.; Martin Prats, M.A.; Bernal, J. Smart shielding techniques for common mode chokes in EMI filters. *IEEE Trans. Electromagn. Compat.* **2019**, *61*, 1329–1336. [CrossRef]
23. Bernal-Méndez, J.; Freire, M.J. On-site, quick and cost-effective techniques for improving the performance of EMI filters by using conducting bands. In Proceedings of the 2016 IEEE International Symposium on Electromagnetic Compatibility, Ottawa, ON, Canada, 25–29 July 2016; pp. 390–395.
24. Weile, D.; Michielssen, E. Genetic algorithm optimization applied to electromagnetics: A review. *IEEE Trans. Antennas Propag.* **1997**, *45*, 343–353. [CrossRef]
25. EN55011:2011/CISPR 11. *Industrial, Scientific, and Medical Equipment—Radio-Frequency Disturbance Characteristics—Limits and Methods of Measurement*; Beuth Verlag: Berlin, Germany, 2009.
26. EN55022:2011/CISPR 22. *Information Technology Equipment—Radio disturbance characteristics—Limits and methods of measurement*; Beuth Verlag: Berlin, Germany, 2008.
27. FCC Part 15. *The FCC 47 CFR Part 15 from the Federal Communications Commission: Rules and Regulations for EMC*; Federal Communications Commission: Washington, DC, USA, 2020.
28. Available online: https://www.coilcraft.com/wbt.cfm (accessed on 15 March 2012).

MDPI
St. Alban-Anlage 66
4052 Basel
Switzerland
Tel. +41 61 683 77 34
Fax +41 61 302 89 18
www.mdpi.com

Electronics Editorial Office
E-mail: electronics@mdpi.com
www.mdpi.com/journal/electronics

MDPI
St. Alban-Anlage 66
4052 Basel
Switzerland

Tel: +41 61 683 77 34
Fax: +41 61 302 89 18

www.mdpi.com

ISBN 978-3-0365-0501-5